

**Universität
Rostock**



Traditio et Innovatio

**FABRICATION OF POLYMER-BASED OPTOFLUIDIC MICROSYSTEMS
FOR OPTICAL FLUID ANALYSIS ON PRINTED CIRCUIT BOARDS**

HERSTELLUNG VON POLYMERBASIERTEN OPTOFLUIDISCHEN
MIKROSYSTEMEN ZUR OPTISCHEN FLUIDANALYSE AUF LEITERPLATTEN-BASIS

Dissertation zur Erlangung des akademischen Grades
Doktor-Ingenieur (Dr.-Ing.)
der Fakultät für Informatik und Elektrotechnik
der Universität Rostock

vorgelegt von Ekaterina Sergeeva
geboren am 30.04.1988 in Smolensk
aus Rostock

Rostock, März 2019

https://doi.org/10.18453/rosdok_id00002429

This work was carried out between April 2015 and October 2018 under supervision of Prof. Dr.-Ing. Dennis Hohlfeld at the Institute of Electronic Appliances and Circuits, University of Rostock

Date of submission: 30.10.2018

Date of defense: 19.02.2019

Reviewers: Prof. Dr.-Ing. Dennis Hohlfeld
Chair of Micro- and Nanotechnology of Electronic Systems
Institute of Electronic Appliances and Circuits
University of Rostock

Prof. Dr. Hans Zappe
Gisela and Erwin Sick Chair of Micro-optics
Department of Microsystems Engineering, IMTEK
University of Freiburg

Prof. Dr.-Ing. Nils Damaschke
Chair of Optoelectronics and Photonic Systems
Institute of General Electrical Engineering
University of Rostock

Selbstständigkeitserklärung

Ich versichere hiermit, die vorliegende Dissertation eigenständig und ausschließlich unter Verwendung der angegebenen Hilfsmittel angefertigt zu haben. Alle öffentlichen Quellen sind als solche kenntlich gemacht.

Rostock, den 13. März 2019



Ekaterina Sergeeva

Hiermit erkläre ich, dass die vorgelegte Promotionsschrift bisher weder im Ausland noch im Inland in gleicher oder ähnlicher Form einer anderen Prüfungsbehörde vorgelegt wurde.

Rostock, den 13. März 2019



Ekaterina Sergeeva

Dedicated to my deceased father, who always wanted me to be the
first scientist in our family.

Посвящается моему так рано ушедшему из жизни отцу, всегда
мечтавшему видеть меня в науке.

Abstract

Next generation printed circuit boards, which are equipped with components and structures for processing and transmitting both electrical and optical signals, are known as (hybrid) electro-optical circuit boards (EOCBs). They can be used for board-level high speed data transmission as well as for implementation of compact devices for measuring physical properties of fluids (optofluidic lab-on-a-board systems). EOCBs are in the focus of many academic and industrial research groups. Only a few of the existing technologies, mainly found in industrial environments, can be used for cost-effective prototyping of polymer-based EOCBs.

This thesis focusses on the establishment of a technological process chain for prototyping of EOCB-based sensing platforms for optical fluid analysis with photopolymer-based optical waveguides integrated with microfluidic channels on FR-4^a, glass and PMMA^b substrates. The combination of established mask-based lithography with laser direct writing is proposed as the technological basis for it. This flexible and easily scalable to large substrates technology is established for epoxy resin-based photolithographically patternable polymers (SU-8, EpoCore, and EpoClad). Subsequent sealing of microchannels is performed by dry resist lamination. Encountered challenges and implemented solutions towards an optofluidic prototype are discussed in detail in this thesis.

The influence of technological parameters (e.g. substrate pre-treatment methods, laser intensity profile, size and shape of the focused laser spot, exposure dose, parameters of tempering process) on the quality of fabricated optical structures is investigated. Herein, methods for improving polymer adhesion, homogenization of the refractive index inside the laser-written waveguide core, and geometric and optical waveguide properties are comprehensively studied. Using optimized laser direct writing process parameters, multi-mode waveguides with a typical core size of $50 \times 50 \mu\text{m}^2$ as well as few-mode waveguides with a minimum achievable cross-sectional dimension of $3.5 \times 6 \mu\text{m}^2$ are structured at high precision.

Optical characterization and determination of application potentials and limitations of straight waveguides, bends, splitters and combiners, being fundamental building blocks of future optofluidic sensing units, is studied in great detail. In particular, the optical propagation losses induced by intrinsic material absorption and scattering at the sidewalls are determined at visible and infrared wavelengths depending on the used waveguide material combination and tempering parameters. For instance, multi-mode EpoCore/EpoClad waveguides fabricated according to optimized process parameters exhibit propagation losses of 0.59 dB/cm at a wavelength of 850 nm, which is in agreement with values of epoxy-based waveguides found in related works. In bent waveguides, propagation losses are accompanied by curvature-dependent bending losses, which are found to become significant for bending radii smaller than 6 mm. The dependence of bending losses on the radius of curvature at the wavelength of 850 nm is determined empirically for EpoCore/EpoClad waveguides.

Different laser beam shaping concepts in a custom-made laser direct writing setup are discussed in detail. Top-hat like laser intensity profiles with circular and rectangular beam cross sections are

^a FR-4 is a glass-reinforced epoxy laminate material

^b PMMA stands for poly(methyl methacrylate)

formed by apertures. This allows structuring of flat and curved waveguide end-faces, whose shape and size depend on the trajectory, profile, and diameter of the laser beam. The characteristics of light propagation across the gap between two end-faces of a discontinuous waveguide strongly depend on the geometry of the end-faces. Thus, insertion loss originating at the gap between two curved end-faces can be specifically improved by focusing through suitably curved end-faces, compared to flat end-faces.

The feasibility of the established technology for the fabrication of compact all-polymer EOCB-based lab-on-a-board systems is proved by four optofluidic demonstrators, whose operation principles are based 1) on light absorption in a fluid during free propagation of light in a microchannel, 2) on evanescent field absorption, 3) on partial back reflection at the waveguide end-faces, and 4) on thermo-optic interferometric effects. For each of the demonstrators, first, a design concept is created, then their fabrication parameters are optimized, and, finally, sensing performance is evaluated.

Although the integrated measuring platforms presented in this thesis do not (yet) come close to the sensitivity of conventional table-top fluidic laboratory measuring equipment, they provide a high level of functional integration, compactness, and the possibility of autonomous operation. The presented optofluidic EOCB-sensors expand the functionality of existing cost-effective lab-on-a-board devices and have a promising application potential e.g. in optical communications, biotechnological and environmental industries.

Keywords: electro-optical circuit board, optofluidics, fluid sensing, polymer optical waveguides, optical losses, EpoCore/EpoClad, FR-4, photolithography, laser direct writing, evanescent field spectroscopy, measurement of light absorption, refractometry, Mach-Zehnder interferometer, thermo-optic effect

Zusammenfassung

Leiterplatten der nächsten Generation, die mit Bauelementen bzw. Strukturen für die Verarbeitung und die Weiterleitung sowohl elektrischer als auch optischer Signale bestückt sind, werden als (hybride) elektrisch-optische Leiterplatten (engl. electro-optical circuit boards, EOCBs) bezeichnet. EOCBs können sowohl für die Datenkommunikation als auch für integrierte Messgeräte für physikalische Fluideigenschaften (optofluidische Lab-on-a-Board-Systeme) eingesetzt werden. In der Forschung ist ein zunehmendes Interesse an diesem Bereich zu verzeichnen. Nur wenige der existierenden und vorwiegend im industriellen Umfeld anzutreffenden Fertigungstechnologien sind für das kostengünstige Prototyping von polymerbasierten EOCBs einsetzbar.

Die vorliegende Dissertation fokussiert sich auf der Etablierung einer technologischen Prozesskette zum Prototyping von EOCB-basierten optofluidischen Messvorrichtungen mit polymerbasierten integrierten Lichtwellenleitern und mikrofluidischen Strukturen auf Glas-, FR-4^a- und PMMA^b-Substraten. Die Kombination aus maskenbasierter Photolithographie und flexiblem Laserdirektschreiben mit abschließender Abdeckung der Mikrokanäle mittels Auflaminieren von Trockenlacken bildet dafür die technologische Grundlage. Zu den Vorteilen des Laserdirektschreibens (engl. laser direct writing) zählen die hohe Flexibilität, schnelles Prototyping und die Skalierbarkeit auf große Substrate. Diese Technologie wurde für kommerziell erhältliche photolithographisch strukturierbare Epoxidharz-basierte Photopolymere (SU-8, EpoCore und EpoClad) umgesetzt. Auf die aufgetretenen technologischen Schwierigkeiten und deren Lösung wird in dieser Arbeit detailliert eingegangen.

Der Einfluss technologischer Parameter, wie Substratvorbehandlung, Laserintensitätsprofil, Größe und Form des fokussierten Laserspots, Belichtungs dosis und Parameter des Temperierungsprozesses auf die Qualität der gefertigten optischen Strukturen wird erforscht. Dabei werden Verfahren zur Verbesserung der Polymerhaftung, Homogenisierung der Brechzahlverteilung innerhalb des lasergeschriebenen Wellenleiterkerns, sowie zur Verbesserung der geometrischen und optischen Wellenleitereigenschaften ausführlich untersucht. Mittels optimierter Laserdirektschreiben-Prozessparameter konnten auf Polymerbasis sowohl Multi-Mode-Wellenleiter mit einer typischen Querschnittsgröße von $50 \times 50 \mu\text{m}^2$ als auch Wenig-Mode-Wellenleiter mit kleinstem erzieltm Querschnitt von $3,5 \times 6 \mu\text{m}^2$ strukturiert werden.

Gefertigte gerade und gebogene Wellenleiter, Verzweiger und Kombinerer, die als Basiskomponenten künftiger optofluidischer Messvorrichtungen fungieren werden, werden in dieser Arbeit eingehend optisch charakterisiert. Insbesondere die durch intrinsische Materialabsorption und Streuung an den Seitenwänden hervorgerufenen optischen Propagationsverluste werden im sichtbaren und infraroten Lichtspektrum in Abhängigkeit vom Kernmaterial und den verwendeten Temperierungsparametern ermittelt. So betragen die Propagationsverluste beispielsweise bei nach optimierten Prozessparametern gefertigten Multi-Mode EpoCore/EpoClad-Wellenleitern 0,59 dB/cm bei einer Wellenlänge von 850 nm, was mit von anderen Forschungsgruppen ermittelten Werten für Epoxidharz-basierten Wellenleitern übereinstimmt. In gebogenen Wellenleitern treten neben

^a FR-4 ist ein Epoxid-Glasfasergewebe

^b PMMA steht für Polymethylmethacrylat

Propagationsverlusten noch krümmungsinduzierte Biegeverluste auf, die für Krümmungsradien kleiner als 6 mm signifikant sind. Die Abhängigkeit des Biegeverlustes vom Krümmungsradius wird bei der Wellenlänge von 850 nm für die EpoCore/EpoClad Wellenleiter anhand gefertigter Teststrukturen experimentell bestimmt.

Verschiedene Laserstrahlformungskonzepte, die in der selbstkonstruierten Laserdirektschreiben-Anlage zum Einsatz kommen, werden ausführlich behandelt. Top-hat-ähnliche Laserintensitätsprofile mit kreisförmigem und rechteckigem Strahlquerschnitt werden durch Aperturen gebildet. Dies ermöglicht die Strukturierung von planen und gekrümmten Wellenleiterstirnflächen, deren Form und Größe von der Trajektorie, dem Profil und dem Durchmesser des Laserstrahls abhängen. Der Lichtübergang durch den Spalt zwischen zwei Stirnflächen eines diskontinuierlichen Wellenleiters ist stark von der Geometrie der Stirnfläche abhängig. So kann die Einfügedämpfung, die im Spalt zwischen zwei gekrümmten Stirnflächen entsteht, mittels Fokussierung durch entsprechend gekrümmte Stirnflächen im Vergleich zu Wellenleitern mit planen Stirnflächen gezielt eingestellt und verbessert werden.

Die breite Anwendbarkeit der entwickelten Technologie zur Herstellung von kompakten Lab-on-a-Board-Systemen auf EOCB-Basis wurde exemplarisch anhand von vier optofluidischen Demonstratoren bestätigt, deren Funktionsweise 1) auf Lichtabsorption in einer Flüssigkeit während einer freien Lichtausbreitung, 2) auf evaneszenter Feldabsorption, 3) auf partieller Rückreflexion an der Wellenleiterstirnfläche und 4) auf thermooptischen modulierter Interferometrie beruht. Zunächst wurde für jeden der Demonstratoren ein Designkonzept erstellt, anschließend eine optimierte Herstellung mittels Laserdirektschreiben durchgeführt und schließlich eine Bewertung der Sensitivität vorgenommen.

Wenngleich die in dieser Arbeit vorgestellten integrierten Messplattformen (noch) nicht die Empfindlichkeit herkömmlicher fluidischer Labormessgeräte erreichen, so zeichnen sie sich jedoch durch ihren hohen Integrationsgrad, Kompaktheit und die Möglichkeit zum autonomen Betrieb aus. Diese Demonstratoren erweitern die Funktionalität der bestehenden kosteneffektiven Lab-on-a-Board-Messvorrichtungen und haben ein großes Anwendungspotenzial z.B. in der optischen Kommunikation oder in biotechnologischen bzw. umwelttechnischen Anwendungen.

Schlüsselworte: elektro-optische Leiterplatte, Optofluidik, Fluidsensorik, Polymerlichtwellenleiter, optische Verluste, EpoCore/EpoClad, FR-4, Photolithographie, Laserdirektschreiben, Evaneszenzfeldspektroskopie, Messung der Lichtabsorption, Refraktometrie, Mach-Zehnder-Interferometer, thermooptischer Effekt

Acknowledgments

Firstly, I would like to thank Prof. Dr.-Ing. Dennis Hohlfeld, my scientific advisor at the Institute of Electronic Appliances and Circuits, for arousing my interest in this project. I am very grateful for the by you provided opportunity to perform this research, for your time, and for sharing your professional network and expertise with me.

I would like to express my sincere gratitude to Dr. rer. nat. Haldor Hartwig, who was co-supervising my work and encouraging me during the ups and downs of my scientific work. Without your guidance and support in scientific issues, wise advices, and willingness to help this study would have been impossible.

I am grateful for the invaluable and varied contributions of our former students to this thesis, as well as being motivated and well-organized. Particularly, I owe a great debt of thanks to M. Sc. Jendrik Schmidt for providing with an electrical circuit and co-development of the platform for turbidity measurements of water within the scope of his master thesis. Secondly, I thank M. Sc. Nils Thomas for assembling and programming a laser beam profiler and for conducting laser beam analysis. Additionally, I would like to thank B. Sc. Henning Bathel for his diligence to investigation of waveguide shape's and cross-sectional dimension's influence on the back-reflection signal and study of attenuation in polymer optical waveguides.

My special thanks go to Dr. rer. nat. Alexander Hause and Dr. rer. nat. Christoph Mahnke from the scientific group "Nonlinear Optics" of the Physics Department of the University of Rostock for providing an infrared laser for preliminary tests of the Mach-Zehnder interferometer structures, for giving access to a fiber fusion device for the fabrication of fibers with a curved tip, as well as for having friendly and productive lunches together. Your humorous statement "Aus diesen Ergebnissen kann man Interferenz nicht ausschließen" after an enormous number of unsuccessful measurements gave me more motivation for further experiments.

I would like to thank the entire team of the Institute of Electronic Appliances and Circuits for a great professional atmosphere and their positive attitude. Special thanks go to Michael Otto and Britta Wederka for a fast fabrication of printed circuit boards and related photomasks, to Dr.-Ing. Andrej Novikov and Dr.-Ing. Fred Lange for their practical advice and generously sharing their expertise with me. I greatly appreciate their cooperativeness and willingness to support young researchers.

Furthermore, I am grateful to the team of the Department of Piston Machines and Internal Combustion Engines, particularly to Dipl.-Ing. Thomas Sadlowski, for providing access to the laser scanning microscope, which made the measurements of sidewall roughness of our polymer microstructures possible.

I wish to acknowledge the state of Mecklenburg-Vorpommern and the University of Rostock for the financial support, and Mrs. Susanne Engler for her cooperation.

A special thank deserve members of my peer-mentoring group of KarriereWegeMentoring program, Anne Berthold, Merel Hofmeijer, Katrin Gärtner, and Fanny Romoth, for their constant emotional support and helpful advises.

Last but not least, my deepest and warmest acknowledgements are extended to my family members and close friends in my home country, Russia. Thank you for never questioning me, accepting a lifelong student. Mikhail, thank you for being a rock, I could not have gone through this academic journey without your unfailing understanding, encouragement, and unrelenting support. Без вашей поддержки и подбадриваний, мои родные, я бы не справилась с этой многосторонней задачей!

Table of contents

Abstract	i
Zusammenfassung	iii
Acknowledgments	v
Nomenclature.....	xi
Acronyms.....	xiii
1 Introduction.....	1
1.1 Motivation: Electro-Optical Circuit Boards for Data Communication and Optical Sensing	1
1.2 Fabrication of Optical Waveguides and Miniaturized Optical Fluid Sensors	3
1.3 Research Objectives and Thesis Outline	5
2 Theoretical Background	9
2.1 Light Guiding Theory	9
2.1.1 Refractive Index.....	9
2.1.2 Fresnel Equations	9
2.1.3 Internal Reflection.....	11
2.1.4 Numerical Aperture.....	12
2.1.5 Number of Modes and Mode Cutoff.....	12
2.2 Evanescent Field.....	15
2.3 Attenuation in Optical Waveguides	16
2.4 Propagation of Laser Beam - Gaussian Beam Optics	18
3 Establishment of a Process Chain.....	21
3.1 Material Selection: Optical Guiding Structures on EOCBs	22
3.1.1 Optical Material Requirements	22
3.1.2 Optical Polymers for Integrated Optics.....	23
3.1.3 Overview of the Most Relevant Optical Polymers	24
3.1.4 Substrate Materials	26
3.2 Pre-Processing: Substrate Cleaning and Adhesion Promotion	26
3.2.1 Chemical Treatment	27
3.2.2 Plasma Treatment	27
3.2.3 Dehydration Bake.....	28
3.2.4 Application of an Adhesion Promoter.....	28

3.3	Application of Photopolymer Films.....	28
3.3.1	Spin Coating	29
	Spin Coated Film Defects	30
3.3.2	Softbake Process	31
3.3.3	Adjustment of Photopolymer Layer Thickness	31
3.4	Photolithography	32
3.4.1	Mask-Based Photolithography.....	32
3.4.2	Laser Direct Writing Setup for Mask-less Lithography.....	33
	Laser Beam Shaping	35
	Laser Beam Parameter Calculation.....	37
	Threshold Model for Structure Dimensions and Exposure Series	38
	Program Code Design for Laser Direct Writing.....	40
3.4.3	Post Exposure Bake Process.....	41
	Inhomogeneities within a Core.....	42
3.4.4	Development.....	43
3.4.5	Towards Single-Mode Waveguides.....	44
3.5	Post-Processing.....	46
3.5.1	Polishing of the End-Faces	46
3.5.2	Board Level Integration: Light Coupling Concepts.....	48
3.5.3	Optofluidic Device Packaging – Fluidic Connection	49
4	Characterization of Optical Waveguide Components.....	51
4.1	Optical Characterization of Polymer Waveguides	51
4.1.1	Propagation and Coupling Losses Analysis	51
4.1.2	Spectral Light Absorption in Epoxy-based Polymer Waveguides	53
4.1.3	Geometry-Induced Losses: Propagation in 90° Waveguide Bends	56
4.2	Sidewall Roughness Analysis.....	58
4.3	Impact of End-Face’s Geometry on Light Focusing and Transmission in Discontinuous Waveguides.....	61
4.4	Mode Behavior in Fabricated Single-Mode Waveguides.....	66
5	Optofluidic Platforms and Lab-on-a-Board Demonstrators.....	69
5.1	Absorption-based Sensor Unit on EOCBs.....	69
5.1.1	Optical Board for a Miniaturized Turbidity Measurement Setup: Laboratory Tests	72
5.1.2	Absorption-based Demonstrator on EOCBs: Assembly and Performance	73

5.2	Evanescent Field-based Sensor Unit on EOCBs.....	76
5.3	Fresnel-Refractometer on EOCBs.....	81
5.3.1	Fiber-Based Implementation of Fresnel-Refractometer	83
5.3.2	Design of EOCB-Based Fresnel-Refractometer.....	84
5.3.3	Sensor Performance and Influence of Waveguide’s Tip Shape	86
5.4	Mach-Zehnder Interferometers on EOCBs.....	88
5.4.1	Mach-Zehnder Interferometer-based Refractometer	88
5.4.2	Thermo-optic Effect in Polymer MZI-based Tunable Attenuator.....	89
	Design of MZI-based Thermo-optic Light Attenuator	90
	Temperature Distribution over MZI Branches	90
	Performance of MZI-based Attenuator on EOCB.....	92
6	Conclusions and Outlook.....	97
6.1	Conclusions.....	97
6.1.1	Fabrication.....	97
6.1.2	Analysis of Optical Waveguides.....	99
6.1.3	On-Board Detection: Demonstrators Performance	100
6.2	Recommendations and Future Work	102
6.2.1	Technological Research Needs.....	102
6.2.2	Constructive Research Needs.....	103
	Laser Direct Writing Setup	103
	Design and Optimization of Waveguide Shapes	103
	Coupling Concepts.....	104
6.2.3	Further Testing Techniques and Device Designs.....	104
7	Bibliography.....	107
8	Appendix.....	121

Nomenclature

symbol	meaning	unit
λ	wavelength	nm
θ	divergence angle	rad
θ_i	incident angle	rad
θ_r	angle of reflection	rad
α	extinction coefficient	m^{-1}
τ	time constant	s^{-1}
φ	phase shift	rad
A	absorbance	-
b	depth-of-focus	$\mu\text{m} / \text{mm}$
c	analyte concentration	%
d_p	penetration depth of an evanescent wave	μm
D	exposure dose	J/cm^2
I	light intensity	W/cm^2
I	current	A
L	length	m / mm
$n (n_{cl} / n_c)$	refractive index (cladding / core)	-
P	optical power	W
r	bent radius, radius of curvature	mm
R	electrical resistivity	Ω
R_a	mean roughness	$\text{nm} / \mu\text{m}$
R_q	root mean square roughness	$\text{nm} / \mu\text{m}$
R_z	mean roughness depth	$\text{nm} / \mu\text{m}$
t	time	s
T	temperature	$^{\circ}\text{C} / \text{K}$
T_g	glass transition temperature	$^{\circ}\text{C}$

V ($V_{IL}, V_{BL}, V_{RL},$ V_{CL}, V_{TL})	optical losses (insertion, bending, reflection, coupling, and transmission losses)	dB, dB/cm
w	beam waist radius	μm
W	width of bent waveguide section	mm
z_R	Rayleigh length	mm
x, y, z	axis	-

Acronyms

3D	three-dimensional
AFM	atomic force microscopy
ATR	attenuated total reflection
BPP	beam parameter product
CAD	computer-aided design
CCD	charge coupled device
CTE	coefficient of thermal expansion
DI	deionized
EFR	effective refractive index
EM	electromagnetic
EOCB	electro-optical circuit board
FEM	finite element method
FR	flame retardant
GBL	γ -Butyrolactone
HDT	heat deflection temperature
HMDS	hexamethyldisilazane
LDW	laser direct writing
IPA	isopropyl alcohol, 2-Propanol
IR	infrared
LED	light-emitting diode
LSM	laser scanning microscopy
MEMS	micro-electro-mechanical systems
MM	multi-mode
MMF	multi-mode fiber
MZI	Mach–Zehnder interferometer
μ PIV	micro-scale particle image velocimetry
NA	numerical aperture
NIR	near-infrared
PCB	printed circuit board
PD	photodiode

PEB	post exposure bake
PMMA	poly(methyl methacrylate)
RI	refractive index
RIU	refractive index unit
rpm	revolutions per minute
SEM	scanning electron microscopy
SM	single-mode
SMF	single-mode fiber
SPR	surface plasmon resonance
TIR	total internal reflection
TPA	two-photon absorption/polymerization
UV	ultraviolet
Vis	visible light range
WG	waveguide

1 Introduction

1.1 Motivation: Electro-Optical Circuit Boards for Data Communication and Optical Sensing

In the field of high performance computing and high-speed data transfer, purely electrical printed circuit boards (PCB) will not be able to support future communication bandwidth requirements [1]. Parasitic capacitance and inductance of the densely arranged copper conductor paths cause capacitive coupling and signal delays. These effects limit practical bandwidth for electronic computing systems on PCBs to 1 GHz [2].

Optical waveguides (WG), i.e. optical structures confining light inside them, have many advantages over electrical circuits, such as immunity against crosstalk, and electromagnetic interference, and thus high integration density and downscaling the footprint, light weight and low heat generation [3, 4]. The ability to transfer signals in one line by means of multiple wavelengths (wavelength-division multiplexing) or multiple time slots (time-division multiplexing) with higher usable bandwidth in comparison to copper paths (THz versus GHz [4]), and the lower dispersion significantly increase data transmission rates and result in high performance, energy efficiency and cost savings [5].

By integrating optical paths along with wires for electrical signals on the same circuit board, a so-called electro-optical printed circuit board (EOCB) is formed. In this hybrid electro-optical unit, integrated optics and waveguides are used for optical signal transmission while copper paths maintain electrical signal processing and power distribution combining the advantages of optical and electrical circuits.

Besides data transmission, EOCBs can be applied in integrated optofluidic measurement devices for evaluation of physical properties of fluids, such as refractive index, concentration, and turbidity [6]. Optofluidics is an emerging research area focused on synergetic merging of optics and microfluidics e.g. by integration of optical waveguides into fluidic elements, such as microchannels or cuvettes, onto one compact carrier. Microfluidic laminar flows can efficiently transport various micro- and nanoobjects optical properties of which needs to be investigated. Those objects, which are usually difficult to deal with, can be easily delivered using microchannels into sensing area of an optical circuit. Miniaturized optofluidic devices incorporate principles of large-scale analysis on one single board, so measurements can be performed directly on the EOCB without external optical set-ups and detection units. Therefore, they are referred to as lab-on-a-chip or lab-on-a-board sensor systems [7, 8], see Fig. 1.1.

The integration into a variety of sensing schemes, wavelength selectivity, corrosion-resistance, electrical passivity, small instrumentation footprint, minimized consumption of reagents, and relatively low costs are the advantages of microfluidic optical sensors that make them attractive for several applications [8, 9]. Industrial, environmental, and biomedical optical sensing encompass fluid refractive index and concentration measurements [10–13], absorption spectroscopy [14–16], particle counting [17], flow cytometry (cell analysis comprising cell detection, counting, and sorting) [18, 19], lens-less microscopy [20], and light-driven manipulation [21].

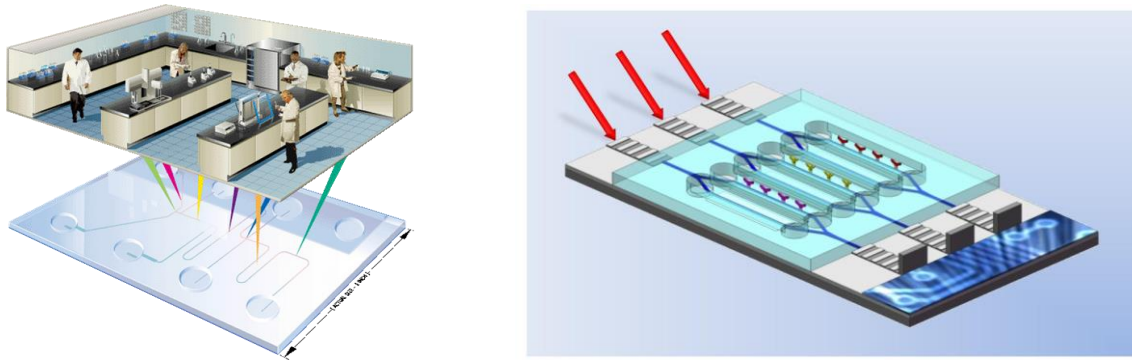


Fig. 1.1: (Left) Concept of a droplet microfluidic lab-on-a-chip/lab-on-a-board device that integrate laboratory functions on a single chip of only a few square centimeters footprint (picture source: <http://lab-on-chip.gene-quantification.info>); (right) Integrated optical devices for lab-on-a-chip biosensing applications: arrays of Mach-Zehnder interferometers are integrated into microfluidics channels, grating couplers are used for the light coupling, photodetectors and electronics for data processing, source: front cover picture of *Laser & Photon. Rev.* 6(4)/2012.

Most of the optical measurement principles were already implemented based on robust and chemically stable conventional glass fibers. The chemical stability and exceptionally broadband light transparency [22] make glass fibers a key component in many fluid chemical testing devises [12, 15, 16].

In refractive index or concentration analysis, the cladding-free glass fiber is placed into the fluid under test, allowing a part of the propagating light (evanescent field, for more details refer section 2.2) to be absorbed by it. The output and input signals comparison serves as a basis for conclusions about physical properties of the medium, such as refractive index, concentration, and chemical composition.

In absorption spectroscopy measurements and flow cytometry, light propagates freely within the testing region in a microchannel and interacts with a fluid under test. The transmitted light is then guided to the detector, which acquires its spectral composition. In case of particle / cell counting and flow cytometry, the stream with constant flow rate, containing the cells, is narrowed by microchannel or by hydrodynamic focusing in the sensing area [18, 23]. Here, the particles interrupt the light propagating through the channel causing variations in the detected signal. By counting and analyzing peaks of the output signal level, number and size of particles can be determined.

Despite robustness and high sensitivity of the fiber-based optofluidic setups, they should be supplemented by external optics. Compact and portable lab-on-a-board devices with integrated optical waveguides and other functionalities, such as electronics, microfluidic, and/or micromechanical components, present a promising alternative to the existing bulky and component expensive setups [6, 24, 25]. The integration of conventional glass fibers into a PCB enlarges the footprint and the fabrication costs associated with additional micromachining steps [26, 27]. Therefore, other techniques for waveguide integration should be considered. In the following section, state-of-the-art technologies for fabrication of integrated optical waveguides are discussed with respect to production costs, dimensional limitations, and suitability for possible integration into an EOCB production chain.

1.2 Fabrication of Optical Waveguides and Miniaturized Optical Fluid Sensors

The EOCB fabrication process should be cost-effective, compatible with conventional electronic circuitry fabrication facilities and scalable to standard panel sizes with dimensions of several dozens of centimeters. The necessity to fabricate high resolution optical structures, leads to narrow tolerances in coating of optical material with thickness control in μm range [28].

Several technologies for integrated polymer waveguides fabrication have been reported in literature. In addition to conventional mask-based lithography [29–31], less widespread laser direct writing (LDW) [32, 33], laser ablation [34, 35], nanoimprint lithography [36, 37], two-photon absorption / polymerization (TPA) [38], hot embossing [39], molding [39, 40], and inkjet printing [41–43] have been explored. Ion exchange in glass [44, 45], oxidation and etching of silicon [46, 47], and micromachining of embedded optical glass fibers [26, 27] complete the list of further manufacturing methods of non-polymeric waveguides.

These technologies have their advantages and disadvantages in terms of productivity, resolution, maximal production area, and desired clean room conditions. Some of them require masks, pre-existing patterns, while other are inflexible in terms of mass production and imply single substrate processes, which extend the fabrication cycle and raise fabrication costs. An extensive comparison of these technologies is summarized in Table 1.1. The large scale EOCB production using some of these technologies still remains a challenging task [48].

Among different available technologies for polymer structuring, laser-based techniques, such as laser direct writing, laser ablation, and two-photon absorption, are the most flexible and thus suitable for optimization of the waveguide designs during a prototyping phase since they require no masks or stamps. Two-photon absorption allows the fabrication of delicate polymer structures with a process resolution in a nanometer range but has a considerably long processing time, which makes two-photon absorption technique not suitable for production of large scale structures. Laser ablation is a precise and flexible fabrication technique. However, due to the necessity of ablation of bigger substrate areas, the layer structuring can take longer time in comparison to laser direct writing.

Laser direct writing allows precise, computer-controlled, contact-less, and quick patterning of two- and three-dimensional microstructures on any ultraviolet (UV)-sensitive polymers. This technique implies the movement of a focused laser beam relative to the polymer surface enabling a selective polymer exposure. Typical cross-sectional dimensions of polymer light guiding structures fabricated using laser direct writing fall in the range of 3 – 50 μm . The structure width is defined by laser spot diameter, laser power, and writing speed, i.e. speed of the relative beam-to-substrate movement. The writing speed lies in the range from mm/s to m/s and is limited by laser power, photoresist sensitivity and maximum speed of the computer-controlled translation stage. The cost-efficiency and the accuracy of this process along with design flexibility are the main arguments in favor of laser direct writing as a technological basis for prototyping of polymer-based photonic structures in scope of this research project. Photonic structures, such as straight and bent waveguides, splitters, couplers, tapers, and even lenses, can easily be fabricated at high precision using laser direct writing process.

Table 1.1: Comparison of the state-of-the-art technologies suitable for fabrication of hybrid EOCBs with integrated waveguides.

Technology	Minimal waveguide resolution	Optical structure quality (losses, roughness)	Robustness of optical structures (chemicals, pressure, T)	Flexibility	Fabrication time	Substrate size	Compatibility with PCB fabrication facilities
Mask-based lithography [29, 30]	+++ Si: 200-500 nm polymer: 1-10 μm	++	-	--- mask for each layout is required	+	-	+++ utilized within the PCB industry
Hot embossing [39] (roll-to-roll process)	++ 3-5 μm	++	-	--- stamp is required	++	++	+
Nanoimprint [36, 37]	++ 2-5 μm	++	-	--- stamp is required	+	-	++
Ink-jet printing [43]	-- 50-250 μm	--	--	+++	-	+++	+
Laser direct writing [49]	++ 3-5 μm	+	-	+++	-	+++	+
Two-photon absorption [38]	+++ 40-75 nm	+	-	+++	---	--	+
Silicon photonics (SOI) [46, 47]	+++ 200-500 nm	++	+++	--- mask for each layout is required	-	-	-
Ion exchange in glass [44, 45]	- 1-10 μm	+++	+++	--- mask for each layout is required	--	++	-
Embedded glass fibers [26, 27]	--- not adjustable fiber core diameter	+++	+++	+		--	+++

1.3 Research Objectives and Thesis Outline

A robust technological basis is an essential requirement for experiments and testing of the new measurement approaches. This work addresses the establishment of a flexible fabrication environment at the University of Rostock for prototyping of polymer-based EOCBs for optical fluid sensing. The advantages and limitations of the technology in terms of material combination, minimal structure size, their optical properties, cost effectiveness, process controllability, and repeatability should be investigated in detail. The evaluation of the process chain is performed on several optofluidic demonstrators.

For fabrication of EOCB-based optofluidic sensor systems, an optofluidic component is integrated with a typical PCB material, FR-4 (a glass-reinforced epoxy laminate material). As a result, the optofluidic part, which combines microfluidic channels and polymer-based optical waveguides, is placed on a PCB together with light-emitting diodes (LEDs), detectors, electrodes, heaters, and electrical interconnections.

The waveguides are structured by the precise laser direct writing approach. The microchannels do not require such level of precision and can be patterned using conventional mask-based photolithography, e.g. using a foil mask for cost saving reasons. Fluidic coupling and channel sealing can be implemented by dry film resist lamination, bonding or gluing with upper sealing [50]. Photonic elements can be also integrated into non-sealed cuvettes yielding an open fluidic platform. Elimination of external fluid delivery system can significantly reduce the required volume of sample fluid and makes the open fluidic platform handier and more portable. This technological concept is compatible with the established PCB production chain and equipment.

The thesis covers two main parts: (i) development of a technological process chain for the fabrication of EOCB-based optofluidic platforms and (ii) evaluation of the optical properties and sensing performance of the fabricated EOCB-based optofluidic demonstrators. Fig. 1.2 illustrates schematically the main research objectives of this thesis. The implementation of a robust and reversible optical coupling concept with active or passive alignment of waveguides to external optical components is still a bottleneck in EOCB fabrication and remains one of the main EOCB-related research objectives [51]. The fabrication process chain described in this thesis is used to develop novel optical coupling concepts. Fast and cost-effective fluidic sealing remains a challenge to microfluidic systems production [50]. A fluidic sealing concept compatible with PCB fabrication environment is proposed in this thesis.

Chapter 2 introduces a brief theoretical background of performed research. The theoretical model of laser beam propagation involved in laser direct writing fabrication process is presented. Since the light guiding is implemented by means of optical polymer waveguides, the background of reflection, refraction, and light propagation theory in rectangular waveguides is given.

In **Chapter 3**, the focus lies on the evaluation of selected laser direct writing technology in combination with mask-based photolithography in context of their applicability to the fabrication of integrated polymer waveguides and EOCB-based optofluidic devices. Here, the requirements of optical materials and their compatibility with substrate materials are discussed. Technological process flow is established and separate process steps along with occurring problems and their solution are described in detail. The influence of exposure parameters and substrate material on waveguide quality, such as sidewall steepness and roughness, and occurrence of inhomogeneities within the core, is discussed. Here, the exposure results using a Gaussian and a flat-top UV laser beam

profiles are compared. The use of solder mask laminate for sealing of microchannels is tested and evaluated.

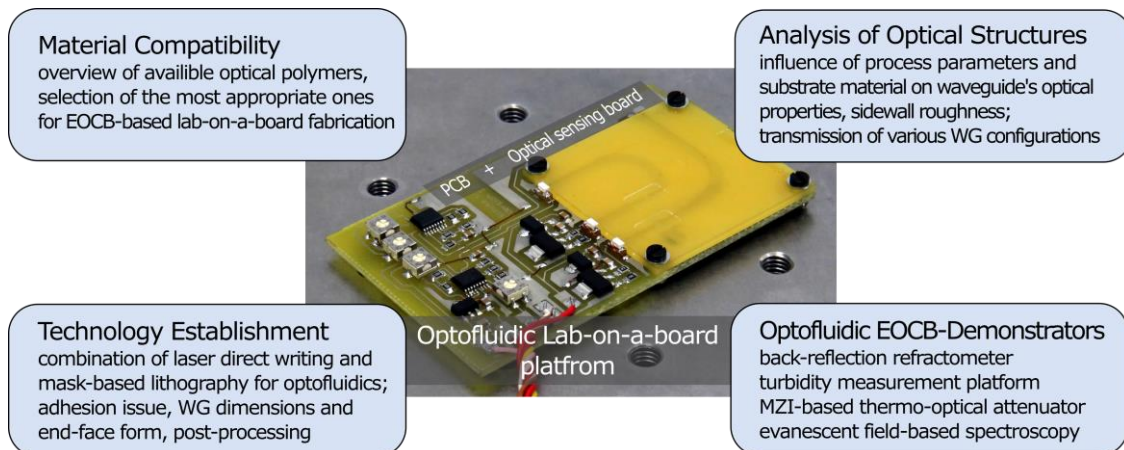


Fig. 1.2: An overview of the research scope of EOCB-based optofluidic sensor units within this project. The background picture shows the fabricated optofluidic lab-on-a-board platform for turbidity measurements on EOCB.

Chapter 4 details the characterization of optical waveguides as the main component of optofluidic platforms. The influence of process parameters and substrate material on morphology and optical properties of the waveguides are studied. In particular, propagation and bending losses, optical transmittance, and sidewall roughness of fabricated waveguides are analyzed.

The main objective of the second part of this thesis is the validation of developed fabrication technology. For this purpose, several lab-on-a-board optofluidic demonstrators are designed. The selected sensing approaches of each demonstrator are based on industrial demand for fluid analysis, with design complexity and technological feasibility taken into account. More specifically, in **Chapter 5**, well established fiber-based measurement techniques, based on absorption, scattering, and light interference effects, are adapted for implementation on EOCBs resulting in four proof-of-principle optofluidic demonstrators:

1. sensor unit with discontinuous waveguides for absorption measurements and concentration determination using a monochromatic light source (section 5.1),
2. evanescent field-based spectroscopic measuring system using broadband light source for chemical fluid analysis (section 5.2),
3. back reflection-based sensor unit for refraction index determination (section 5.3),
4. interferometric thermo-optic modulator / attenuator with integrated heater (section 5.4).

Table 1.2 gives an overview of the most relevant physical and technological properties of these four demonstrators. **Chapter 5** describes in detail the selection of optofluidic sensors, their design, and performance evaluation.

Chapter 6 summarizes the results of the study and gives an outlook about possible future work objectives.

Table 1.2: Classification of the optofluidic demonstrators selected for EOCB-implementation.

Demonstrator / properties	absorption-based	evanescent field-based	reflection-based	interferometric
Nature of light	ray optical	wave optical	ray optical	wave optical
Light propagation	free space	confined in waveguide	confined in waveguide	confined in waveguide
Light interaction phenomenon	free propagation, absorption	evanescent field, absorption	reflection on a boundary	light interference
Mode behavior	multi-mode	multi-mode	multi-mode	single-mode
Waveguide size [μm^2]	50 × 50 ... 50 × 250	50 × 50 ... 50 × 250	50 × 50	3.5 × 6
Working principle	passive	passive	passive	active
Importance of light polarization	-	+	-	+
Wavelength [nm]	650, 850 or broadband	broadband (white light)	650, 850	850, 1310

2 Theoretical Background

This chapter gives a brief theoretical background of performed work. Principles of light transmission in optical waveguides, electromagnetic nature of single- and multi-mode operation, Gaussian beam propagation, and beam shaping are described. This will be followed by a discussion on the sources of optical light attenuation in optical fibers and waveguides.

2.1 Light Guiding Theory

To understand and predict the behavior of light in waveguides, the light guiding theory should be described in detail. This is indispensable for design improvement of the selected optofluidic demonstrators. In this section, the fundamental laws of light propagating phenomena are introduced theoretically based on derivations given in [52].

2.1.1 Refractive Index

An important characteristic of an optical medium is the refractive index (RI) n . In a medium, the light propagation speed c decreases and the wavenumber k increases compared to the corresponding values in vacuum. The refractive index is defined as the ratio of the speed of light c_o or wavenumber k_o in vacuum to the corresponding values in the medium c_m, k_m :

$$n = \frac{c_o}{c_m} = \frac{k_m}{k_o} \quad (2.1)$$

Optical waveguides (WGs) and fibers are the optical structures guiding light inside them. An optical waveguide consists of two materials: *core* in which the light is guided surrounded by the medium that is called *cladding*. For efficient light guiding by means of total internal reflection, core material should have a higher refractive index when compared to the cladding (see section 2.1.3).

The refractive index depends on wavelength, which is known as *material dispersion*. Refractive index of dielectric materials, such as polymers, can be described according to the Sellmeier equation [52], e.g. for EpoCore n_c and EpoClad n_{cl} , the following wavelength dependence is expressed [53]:

$$\begin{aligned} n_c(\lambda) &= 1572 \cdot 10^{-3} + 10^2 \cdot \frac{76}{\lambda^2} + 10^7 \cdot \frac{46}{\lambda^4} \\ n_{cl}(\lambda) &= 1560 \cdot 10^{-3} + 10^2 \cdot \frac{73}{\lambda^2} + 10^7 \cdot \frac{38}{\lambda^4} \end{aligned} \quad (2.2)$$

In this thesis, if not specified, the values of refractive indices are usually given for a wavelength of $\lambda = 850$ nm, thus $n_c = 1.5834$ and $n_{cl} = 1.5708$.

2.1.2 Fresnel Equations

Fresnel equations describe the transmission and reflection of light at the ideally smooth planar interface between two optical media (the amplitudes, phases, and polarization). They are valid for isotropic and homogeneous media [52]. In the case of a rough surface, especially, when the

characteristic dimensions of roughness are in the same order as the wavelength of the incident electromagnetic (EM) wave, diffuse reflection of light on the interface should be considered.

During electromagnetic wave propagation in a transparent dielectric medium, the certain electromagnetic field patterns occur that are termed *modes*. Each light polarization state may be considered as a superposition of two electric field vector components: orthogonal and parallel to the incident plane. In case of *transverse electric (TE) mode* or *s-polarization*, the electric field vector is perpendicular to the plane of incidence ("s" comes from German "senkrecht", meaning "perpendicular"), see Fig. 2.1. *Transverse magnetic (TM) mode* or *p-polarization* occurs when the magnetic field is orthogonal to the plane of incidence and electric field vector lies parallel to it.

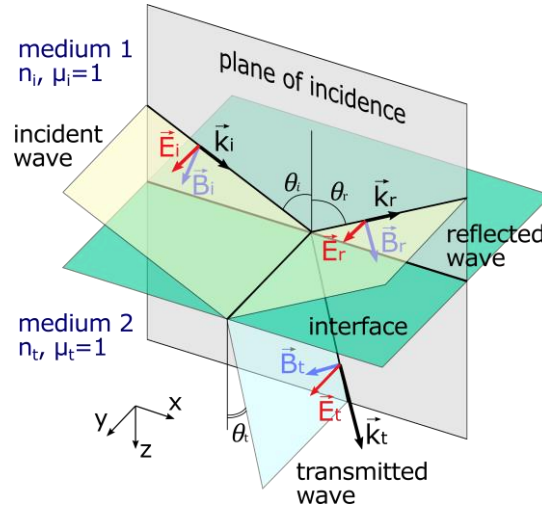


Fig. 2.1: Reflection and transmission of an electromagnetic wave at an interface for special case of *s-polarization* of incident light, arrows correspond to the electromagnetic field vectors.

When an electromagnetic wave impinges at the interface formed by two media with different refractive indices n_i and n_t at an incident angle θ_i , it is partially reflected at an angle θ_r and partially transmitted into the second medium at a transmission angle θ_t (see Fig. 2.1). The light refraction can be described by Snell's law equation (2.4):

$$n_i \sin \theta_i = n_t \sin \theta_t \quad (2.3)$$

For a detailed derivation of the Fresnel equations, refer to the relevant optics books [52, 54]. In brief, it is based on Snell's law with electrostatic boundary condition that the projection of electric \vec{E} and magnetic \vec{B} fields onto the XY -plane (see Fig. 2.1) must be continuous across the interface plane [55], i.e. by assuming that light propagates in non-magnetic media (i.e. $\mu_i = \mu_t = 1$). For an *s-polarized* light it takes the form:

$$E_{i,y} + E_{r,y} = E_{t,y} \text{ and } B_{i,x} + B_{r,x} = B_{t,x} \quad (2.4)$$

Then considering the equations (2.3), (2.4) and that $\cos \theta_t = \sqrt{1 - \sin^2 \theta_t} = \sqrt{1 - \left(\frac{n_i \sin \theta_i}{n_t}\right)^2}$, the reflection r_s and transmission t_s coefficients for *s-polarized* light can be obtained as [54]:

$$\begin{aligned}
r_s &= \frac{E_r}{E_i} = \frac{n_i \cos \theta_i - n_t \cos \theta_t}{n_i \cos \theta_i + n_t \cos \theta_t} = \frac{n_i \cos \theta_i - \sqrt{n_t^2 - n_i^2 \sin^2 \theta_i}}{n_i \cos \theta_i + \sqrt{n_t^2 - n_i^2 \sin^2 \theta_i}} \\
t_s &= \frac{E_t}{E_i} = \frac{2n_i \cos \theta_i}{n_i \cos \theta_i + n_t \cos \theta_t} = \frac{2n_i \cos \theta_i}{n_i \cos \theta_i + \sqrt{n_t^2 - n_i^2 \sin^2 \theta_i}}
\end{aligned} \tag{2.5}$$

The equations (2.5) are known as the Fresnel equations for s-polarization (TE). The fractions of reflected and transmitted incident power are expressed by:

$$R = \frac{P_r}{P_i} = \frac{|E_r|^2}{|E_i|^2} \text{ and } T = \frac{P_t}{P_i} = \frac{n_t \cos \theta_t |E_t|^2}{n_i \cos \theta_i |E_i|^2}, \tag{2.6}$$

where R and T are the ratios of reflected and transmitted powers to the incident power, respectively.

Transmittance is derived from energy conservation:

$$T_{s,p} = 1 - R_{s,p} \tag{2.7}$$

For a special case of normal light incidence ($\theta_i = \theta_t = 0$), the expressions (2.5) and (2.6) take the form:

$$R = \left| \frac{n_t - n_i}{n_t + n_i} \right|^2 \text{ and } T = \frac{4n_i n_t}{(n_t + n_i)^2} \tag{2.8}$$

This is relevant for the most of the polymer waveguides. Although there are rays impinging the end-face boundary in a non-90° angle, due to the small acceptance angle (section 2.1.4), most of the propagating rays are perpendicular to waveguide's end-face. For air ($n_{\text{air}} = 1$) and EpoCore polymer ($n_c = 1.5834$) interface at normal incidence: $R = 5.1\%$ and $T = 94.9\%$. This implies that 5.1% of incident light power will be back-reflected at the boundary in the incidence direction.

2.1.3 Internal Reflection

If light is incident in an optically dense medium towards optically less dense medium ($n_i > n_t$) and the transmission angle $\theta_t = 90^\circ$, then $\sin \theta_t = 1$ (see Fig. 2.2). The *critical incident angle* θ_c can be derived using Snell's law (2.3):

$$\theta_c = \arcsin\left(\frac{n_t}{n_i}\right), \tag{2.9}$$

For incident angles $\theta_i > \theta_c$, all the light undergoes reflection and no light is transmitted across the medium interface. This phenomenon is known as *total internal reflection (TIR)* and is used for light confinement in guided-wave optics.

The working principle of waveguides is based on total internal reflection of electromagnetic waves on the boundary between core and cladding. In this work, EpoCore or SU-8 serve as core of the waveguides, and EpoClad as cladding. This material combination results in a critical angle $\theta_c = 82.77^\circ$; for EpoCore-air interface critical angle is $\theta_c = 39.16^\circ$. As mentioned before, both values are calculated for a wavelength of $\lambda = 850$ nm.

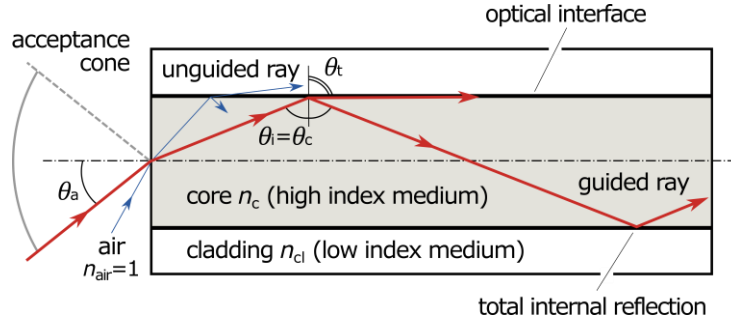


Fig. 2.2: The incident light from a medium with higher refractive index n_c (gray) striking an optically less dense medium n_{cl} (transparent) can be totally reflected at the interface, in case of total internal reflection: $\theta_t = 90^\circ$; illustration of the numerical aperture and acceptance angle of an optical fiber. Rays within acceptance cone are guided by multiple total reflections; otherwise they are refracted to the fiber cladding and not guided by the fiber.

2.1.4 Numerical Aperture

When the rays from a light source are incident on an optical fiber or a waveguide, not all the incoming rays (especially for light sources with wide emission angles, e.g. light emitting diodes) are accepted. The bundle of rays that are incident from air ($n_{\text{air}} = 1$) builds so-called acceptance cone (see Fig. 2.2). The *numerical aperture*, NA is defined by the half-angle θ_a of this acceptance cone:

$$NA = \sqrt{n_c^2 - n_{cl}^2} = \sin \theta_a, \quad (2.10)$$

where θ_a is an *acceptance angle*. For optical polymer waveguides with EpoCore/EpoClad material combination, the numerical aperture is $NA_{WG} \approx 0.199$, and for typical graded-index multi-mode optical glass fiber OM2 with $\varnothing 50 \mu\text{m}$ core the numerical aperture is $NA_{\text{fiber}} \approx 0.2$ [22] ensuing in an acceptance angle of $\theta_a = 11.5^\circ$.

A good match between the numerical apertures of the coupling glass fiber and the polymer waveguide results in minimal coupling losses. For example, in the input side, a fiber with a smaller NA can be chosen to ensure that all light leaving the fiber enters the polymer waveguide, given that the latter has a similar or larger core diameter. A fiber with a larger numerical aperture is chosen accordingly in the output side in order to collect all light leaving the polymer waveguide. There is an additional possibility of minimization of launch losses by applying index matching gel between the fiber and the optical waveguide. The gel has a refractive index value between the refractive index of the fiber and the refractive index of the waveguide material, which leads to splitting the large refractive index difference between these two media into two smaller refractive index discontinuities [56].

2.1.5 Number of Modes and Mode Cutoff

The lowest order mode of appearing electromagnetic modes is called the *fundamental transverse electromagnetic mode*, TEM_{00} . The shape and the number of supported modes are influenced by the geometrical complexity of the guiding structures, the refractive index contrast between core and cladding, and the wavelength of the guided light. The number of guided propagation modes N in a rectangular waveguide or in a circular step-index fiber is finite and can be approximately estimated by the following expressions [52]:

$$N_{\text{rectangular}} \approx \frac{\pi}{4} \left(\frac{2a}{\lambda_0} \right)^2 NA^2, \quad (2.11)$$

$$N_{\text{circular}} = \text{int} \left(\frac{2a}{\lambda} NA \right) + 1, \quad (2.12)$$

where $\text{int}(x)$ is an integer function, a is the largest cross-sectional dimension of a waveguide (in case of a rectangular waveguide its width and for circular waveguide its radius), NA denotes the numerical aperture of the waveguide, and λ_0 is the operating wavelength. From expression (2.11), it can be seen that the shorter the wavelength is, the more modes are supported by the waveguide. For example, a $3.5 \times 6 \mu\text{m}^2$ waveguide supports four TE and four TM modes at $\lambda_0 = 850 \text{ nm}$ (see Fig. 2.3), and two modes TE/TM₀₀ and TE/TM₀₁ at $\lambda_0 = 1310 \text{ nm}$.

A numerical calculation is performed using an open-source 2D multilayer waveguide mode solver from the University of Twente [57, 58]. This solver calculates the approximate effective indices, propagation constants, and coupling lengths for each mode based on modified effective index and film mode matching [58–61] methods with input parameters of waveguide dimensions, refractive indices of core and cladding, and the light wavelength in vacuum. Each mode has its own distinct propagation velocity. Any electromagnetic field distribution on the waveguide output can be expressed as a superposition of the allowed modes.

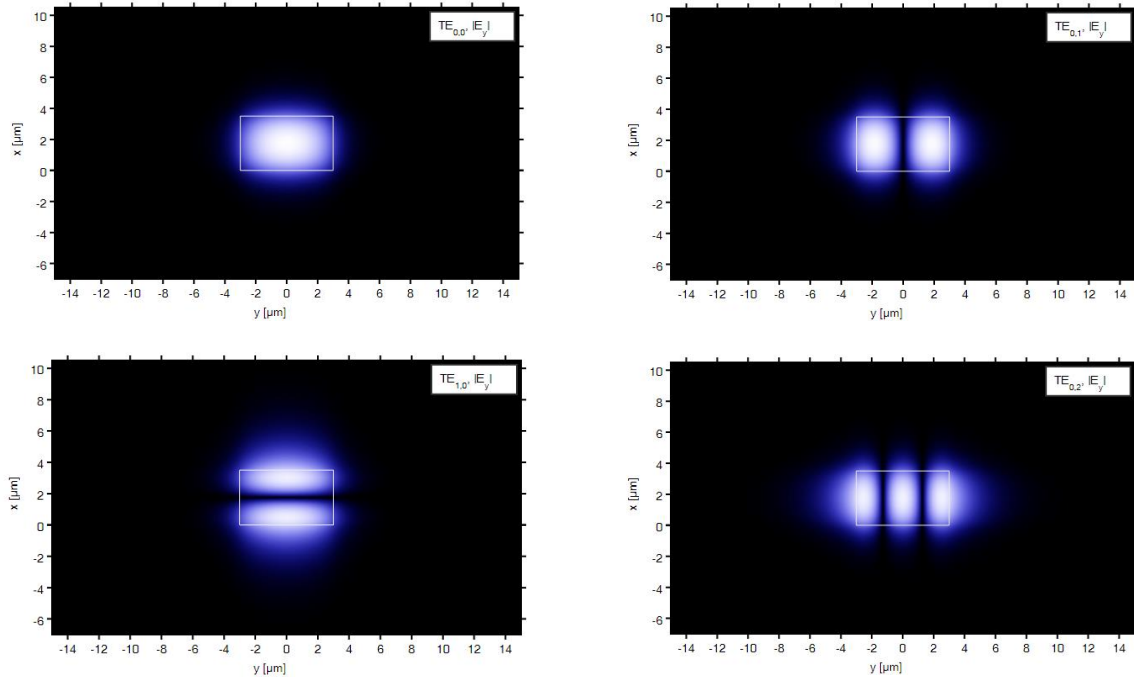


Fig. 2.3: Intensity profiles for lowest order modes supported by a rectangular $3.5 \times 6 \mu\text{m}^2$ EpoCore waveguide at $\lambda = 850 \text{ nm}$, starting from TE_{00} and going up to TE_{02} . The boundaries of waveguide cores are marked as white rectangles.

Depending on the number of propagating light modes, the waveguides and optical fibers could be classified as *single-mode (SM)*, *few-mode*, and *multi-mode (MM)*. In a single-mode waveguide, only one fundamental mode per polarization direction is allowed. The differentiation between few- and multi-mode waveguides is diffuse. In this research project, all-polymer buried and strip loaded rectangular waveguides are considered to be few-mode if the number of supported modes $N < 10$.

In case of single-mode and high order modes of multi-mode waveguides, where the electromagnetic wave extends significantly beyond the boundary of core and cladding, *effective refractive index* $n_{\text{eff_pm}}$ is used to describe the increase of wavenumber for a m^{th} mode with p -polarization in an optical fiber or waveguide in direction of light propagation (z) compared to wavenumber of light in vacuum, i.e.

$$n_{\text{eff_pm}} = \frac{k_{z_pm}}{k_o} = \frac{\beta_{pm}}{k_o} = \beta_{pm} \frac{\lambda_o}{2\pi}, \quad (2.13)$$

where $k_{z_pm} = \beta_{pm}$ is called the *propagation constant* of m^{th} mode with p -polarization in z direction, and $k_o = 2\pi/\lambda_o$ is a free space wavenumber for wavelength λ_o . Effective refractive index and propagation constant are important parameters for prediction of propagation of modes in a waveguide or an optical fiber. It can be calculated either analytically or numerically, depending on the geometry and complexity of an optical waveguide, and wavelength of guided light.

For a proper waveguide operation, the total internal reflection condition should be fulfilled (see section 2.1.3). Therefore, the value of effective refractive index should lie between values of the refractive indices of core and cladding: $n_{\text{cl}} < n_{\text{eff}} < n_c$.

In an ideal circular step-index fiber, the fundamental mode is mathematically always guided. This is different in rectangular waveguides [52, 62]. There is the wavelength above which the rectangular waveguide cannot support any modes which is called the cutoff wavelength λ_c . It depends on the square cross-sectional dimension a of the waveguide and its numerical aperture NA . Cutoff wavelength can be driven from expression (2.11) assuming that $N = 1$ [52]:

$$\lambda_c = a NA \sqrt{\pi} \quad (2.14)$$

At wavelengths longer than the cutoff wavelength, the guidance become weak until the waveguide eventually ceases to operate because of the disappearance of the fundamental mode [52, 62].

From equation (2.11), the critical edge length a_c for a single-mode operation at the wavelength λ_o can be determined in the following way considering that $1 \leq N < 2$:

$$\frac{\sqrt{2}\lambda_o}{\sqrt{\pi} NA} \leq a_{\text{SM}} < \frac{\lambda_o}{\sqrt{\pi} NA} \quad (2.15)$$

Therefore, for wavelengths below cutoff wavelength and cross-sectional dimensions $a > a_{\text{SM}}$ higher order modes are allowed and the waveguide operates in a few- or multi-mode regime. The polymer waveguides fabricated in this research work have typically a rectangular cross section. The numerical estimation (2.15) is also valid if there is a slight deviation from square shape towards rectangular shape. For higher aspect ratios (width : height), the numerical calculation should be performed for the larger edge length.

Polymer waveguides made of EpoCore and EpoClad have $NA = 0.19$ and operate in the single-mode regime for cross-sectional dimensions of $2.52 \mu\text{m} \leq a_{\text{SM}} (850 \text{ nm}) < 3.57 \mu\text{m}$ at $\lambda = 850 \text{ nm}$ and $3.88 \mu\text{m} \leq a_{\text{SM}} (1310 \text{ nm}) < 5.51 \mu\text{m}$ at $\lambda = 1310 \text{ nm}$. For the fabricated polymer waveguide with cross sectional dimension of $3.5 \times 6 \mu\text{m}^2$, the single-mode operation is possible only below the cutoff wavelength of $\lambda_c = 2.02 \mu\text{m}$.

2.2 Evanescent Field

By internal reflection, most of the light remains on the incident side and is reflected from the interface. However, there is an electric field with exponentially decaying amplitude E , the so-called *evanescent field*, which extends beyond the boundary into the surrounding medium (see Fig. 2.4)

$$E = E_0 e^{-\alpha y}, \quad (2.16)$$

where y is the direction normal to the interface and α is known as the extinction coefficient [54].

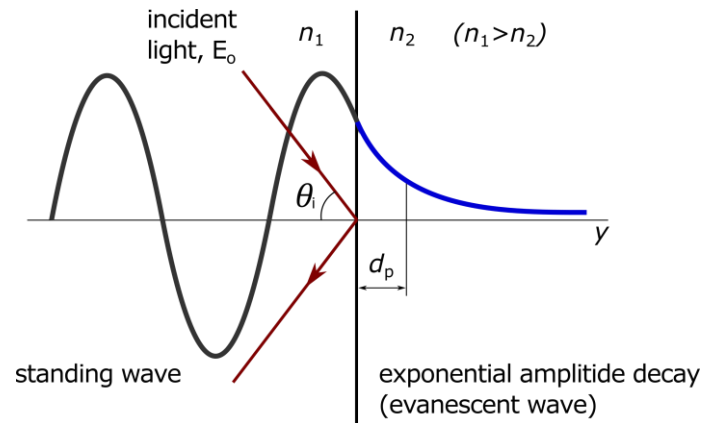


Fig. 2.4: Propagation of evanescent field on the boundary between two media.

The *penetration depth* d_p of the evanescent field is defined as the distance at which the electric field amplitude E falls to $1/e$ ($\approx 37\%$) of its maximum value E_0 . It depends on the wavelength of the incident light λ and the incident angle θ_i . It is expressed as follows:

$$d_p = \alpha^{-1} = \frac{\lambda}{2\pi \sqrt{n_1^2 \sin^2 \theta_i - n_m^2}} \quad (2.17)$$

where n_i and n_m are the refractive indices of the medium of the incident side and the surrounding medium, respectively [63]. For example, for an EpoCore waveguide core with $n_i = 1.587$, water as a surrounding fluid with $n_m = 1.33$ and a critical angle $\theta_c = 56.9^\circ$ calculated using equation (2.9), the depth of penetration yields $d_p = 250$ nm at a wavelength $\lambda = 850$ nm. The depth of electrical field penetration will reduce with shorter wavelength and steeper incident angles.

Evanescent field phenomenon finds its application mostly in photonic couplers and (de)multiplexer [64], microscopy (total internal reflection fluorescence microscopy [65]), and several optical sensors based on attenuated total reflection (ATR) principle [14, 66]. It is used in one of the demonstrators of this thesis as described in section 5.2. In a conventional attenuated total reflection setup, light is propagating in a crystal (most often diamond or germanium) or in an optical fiber with removed cladding by means of total internal reflection under a distinct incident angle θ_i . At points where the light strikes the surface by multiple internal reflections, the evanescent wave penetrates into the sample located straight above the crystal and a portion of the light energy is absorbed by the sample. This effect can be detected as a decrease in light intensity at the end of the crystal or optical fiber. The output signal depends also on the incident light wavelength. This technique is widely used for spectroscopic analysis or concentration determination of highly absorbing sample media [66].

2.3 Attenuation in Optical Waveguides

The exponential reduction in the optical power transmitted by an optical waveguide is called *attenuation* or *optical loss*. It is measured in the logarithmic unit [dB]. Attenuation in an optical waveguide or fiber occurs by three major mechanisms: scattering, absorption, and radiation [67]. The predominant factors depend either on material, geometry, and/or quality of the fabricated light guiding structure. Attenuation reduces the total transmitted optical power reaching the detector and is therefore an essential waveguide design criterion: attenuation should be held minimal in order to obtain a better device performance.

Optical insertion loss V_{IL} results from the insertion of a light guiding structure into an optical link. It combines all of the loss sources contributing to the observed reduction in light power. Insertion loss is calculated by relating the initial optical power emitted from the light source (P_{in}) to the output power (P_{out}) accepted and guided by the waveguide or fiber to the detector after insertion:

$$\text{Optical insertion loss: } V_{IL} \text{ [dB]} = -10 \log_{10} \left(\frac{P_{out}}{P_{in}} \right) \quad (2.18)$$

It is also important to distinguish between waveguide's optical losses (propagation, bend and reflection losses), and other optical losses that appear only while inserting a light guiding structure into an optical system (coupling losses). Figure 2.5 illustrates some sources of intrinsic attenuation in an optical guiding structure, such as scattering at rough sidewalls, at intrinsic defects, and at microbends, losses at unpolished end-faces, and material absorption [68].

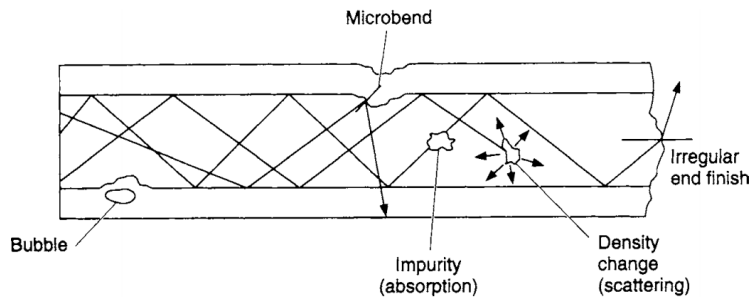


Fig. 2.5: Intrinsic imperfections in an optical fiber (particles, bubbles, cracks, microbends, and density fluctuations) and on the fiber end-face leading to optical losses [68].

Absorption and scattering are the prominent reasons of loss in optical waveguides. They are hard to distinguish from each other and result in the length-dependent *propagation losses* V_{PL} . Propagation losses are specified in [dB/length] and can be experimentally differentiated from the total insertion losses using the cutback technique (see section 4.1.1). Commercial glass fibers have propagation losses in the order of 0.2 dB/km at typical telecom wavelength of 1550 nm [22], which is significantly smaller than the propagation losses observed in polymer waveguides, where the propagation loss typically amounts to 0.2 – 0.5 dB/cm.

Applications in short-distance telecommunications and sensing often require the fibers and waveguides to be bent through a curve in various configurations. Sharp bending causes additional radius-dependent *bending losses* V_B in curved regions. These losses occur mainly at start and finish of the bent section of the waveguide. From the view of ray optics, radiation losses are caused due to failure to comply total internal reflection condition at sharp bends: i.e. some rays exceed critical angle, extend to the cladding and get lost there. For single-mode waveguides and for high order modes of

multi-mode waveguides, which are penetrating deeply into the cladding, light should be considered as an electromagnetic wave. From this point of view, the losses occur due to mode mismatch between straight and curved regions [69] and due to effect of the evanescent field penetration in outer regions of the guiding structure. According to the mode field approach [70, 71], the wave front is considered to be perpendicular to propagation direction (see Fig. 2.6), which means that at the bent part of a waveguide light should move faster at the outer side of the bend to maintain the wave front. It is impossible and leads in reality to light penetration into outer cladding area causing there energy losses through radiation.

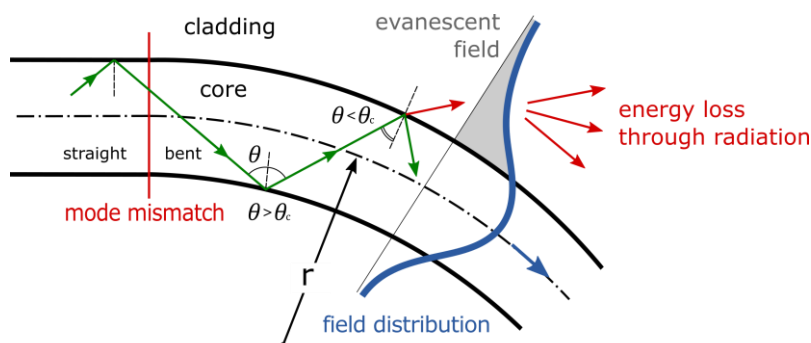


Fig. 2.6: Bending losses in a bent waveguide section: failure of total internal reflection at sharp bends with incident angles less than critical angle ($\theta < \theta_c$) resulting in light transmitted into the cladding; mode field approach: penetration of evanescent field into cladding and induced energy losses through radiation.

A guiding structure starts exhibiting excessive bending losses when the critical bend radius is reached. The critical radius depends on such factors as the refractive index contrast of the core and cladding materials, waveguide width, and light wavelength. The critical radius and bending losses could be reduced by using combinations of core and cladding with a larger refractive index contrast, for instance air-exposed waveguides [70, 72]. Bending losses are specified in [dB/cm] for 90° waveguide bends and can be numerically determined using either beam propagation method, ray-tracing or other simulation techniques [73–75]. In section 4.1.3, the bending losses are experimentally investigated for various radii of curvature of a $50 \times 50 \mu\text{m}^2$ multi-mode waveguide made of EpoCore/EpoClad material combination.

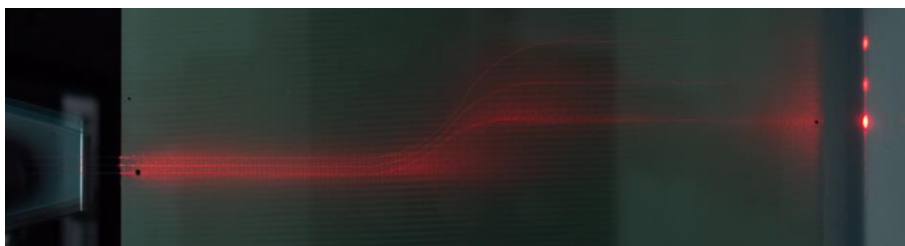


Fig. 2.7: Light leaving the waveguide cores in bent region of multi-mode waveguides at $\lambda = 650 \text{ nm}$ (the picture is taken by multiple exposure by Dr. rer. nat. H. Hartwig).

The Fresnel reflections occur at the boundaries between two media with different refractive indices (see section 2.1.2), such as optical fiber connections, cleaved pigtail fiber tips, and waveguide end-faces. This results in appearance of *Fresnel reflection loss*. Here, a fraction of the light is returned back to the optical source. The reflection loss is calculated from the reflection coefficient R (see equation (2.8)) by applying following rule:

$$\text{Reflection loss: } V_{RL} [\text{dB}] = -10 \log_{10} R \quad (2.19)$$

Coupling losses V_{CL} only appear when inserting a waveguide into an optical system and are a sum of losses due to dimensional and NA discontinuity, mode mismatch between the waveguide and a coupling fiber, and reflection losses on the boundaries. In order to minimize coupling losses, NA discontinuity and reflection loss should be reduced. Therefore, an index matching gel can be applied between the waveguide and launch fiber end-faces for gradual reduction of refractive index difference.

The above mentioned losses are important for characterization of fabricated optical waveguides and will be addressed separately in chapter 4.

2.4 Propagation of Laser Beam - Gaussian Beam Optics

In this research, ultraviolet (UV) laser beam irradiation is used for exposure of polymer structures. A real laser beam can be approximated as a radially symmetric Gaussian beam intensity profile. Thus, it is important to know the propagation parameters of the Gaussian laser beam.

In this work, it is assumed that the laser operates in the fundamental transverse mode, TEM_{00} mode, whose intensity distribution as a function of longitudinal position z is given by the following equation:

$$I(\rho, z) = I_0 \left(\frac{w_0}{w(z)} \right)^2 e^{-2\rho^2/w(z)^2}, \quad (2.20)$$

where $w(z)$ is a beam radius in propagation direction z and $\rho = \sqrt{x^2 + y^2}$ is the radial distance [52]. The beam intensity has maximum value I_0 in the beam center at $\rho = 0$ and decays with increasing ρ (Fig. 2.8). Beam diameter (or beam width) is defined as the distance at which the light intensity has decreased to $1/e^2$ (13.5 %) of its peak value I_0 [76].

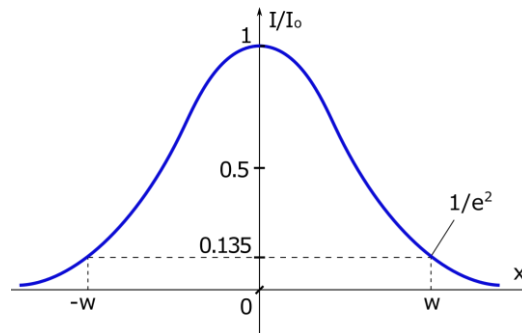


Fig. 2.8: The normalized Gaussian beam intensity profile I/I_0 as a function of the radial distance x . The $1/e^2$ of total intensity value is plotted as dashed lines, which is the standard definition for the Gaussian beam diameter $2w$ [52].

The *beam radius* varies along the propagation direction according to following formula:

$$w(z) = w_0 \sqrt{1 + \left(\frac{z}{z_R} \right)^2}, \text{ where } z_R = \frac{\pi w_0^2}{\lambda} \quad (2.21)$$

Its evolution along the propagation direction z is schematically shown in Fig. 2.9. The beam spot size has minimum value w_0 at the beam waist ($z = 0$) and then gradually grows along the propagation axis. Thus, w_0 defines the beam waist radius. The distance to the beam waist over which the beam

can propagate without diverging significantly and the beam diameter widens by a factor of $\sqrt{2}$ is known as *Rayleigh length*, z_R :

$$w(z_R) = \sqrt{2}w_0 \quad (2.22)$$

The distance between these two points located on each side of the beam waist is known as *depth-of-focus* b :

$$b = 2z_R = \frac{2\pi w_0^2}{\lambda} \quad (2.23)$$

Far from the beam waist ($z \gg z_R$), the divergent Gaussian beam is asymptotically approaching a cone with a half angular aperture θ , see Fig. 2.9. This angle is called *far-field divergence angle* of the beam and is governed by

$$\theta = \frac{w_0}{z_R} = \frac{\lambda}{\pi w_0} \quad (2.24)$$

Rewriting (2.24), an invariant of Gaussian beam propagation, the *beam parameter product* (BPP) can be obtained:

$$BPP = \theta w_0 = \frac{\lambda}{\pi} = \text{const} \quad (2.25)$$

The beam parameter product quantifies the quality and the focusability of a laser beam. Therefore reducing the beam waist diameter w_0 leads to an increased beam divergence angle θ [52].

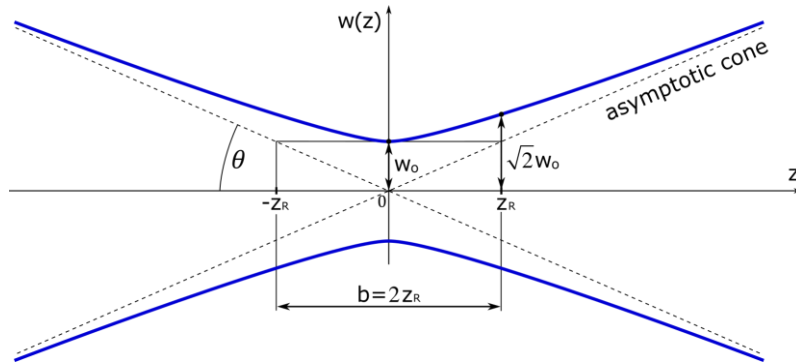


Fig. 2.9: Evolution of a Gaussian beam radius (blue line) and characteristics of Gaussian beam: Rayleigh length, z_R , depth-of-focus, b . Dashed lines indicate the asymptotic behavior of Gaussian beam far from the beam waist.

In reality, most of the laser beams deviate from an ideal Gaussian beam by operating in higher TEM modes or due to other distortions, such as astigmatism and beam asymmetry. However, this approximation can be accepted for the experimental determination of the beam waist, the depth-of-focus and the divergence angle of a highly focused ultra-violet laser beam (375 nm) involved in fabrication of polymer-based single-mode waveguides. For the real beam parameters calculations see section 3.4.2.

3 Establishment of a Process Chain

For industrial integration, the technological process of electro-optical circuit board (EOCB)-based devices should be compatible with conventional electronic industry equipment, scalable to standard panel sizes and cost-effective [77]. Section 1.2 gives an overview of existing approaches of the fabrication of high resolution microstructures.

Photolithography is one of the most important technologies in microsystems and microelectronics production industry [78], which is used to achieve a specific pattern on a photosensitive polymer. In this research project, a combination of laser direct writing (LDW) with established mask-based photolithography technique is used as a basis technology for fabrication of optofluidic platforms. It has the potential of integration into the standard printed circuit board (PCB) fabrication chain^a. A schematic of the simplified process chain of the combined photolithography process is shown in Fig. 3.1.

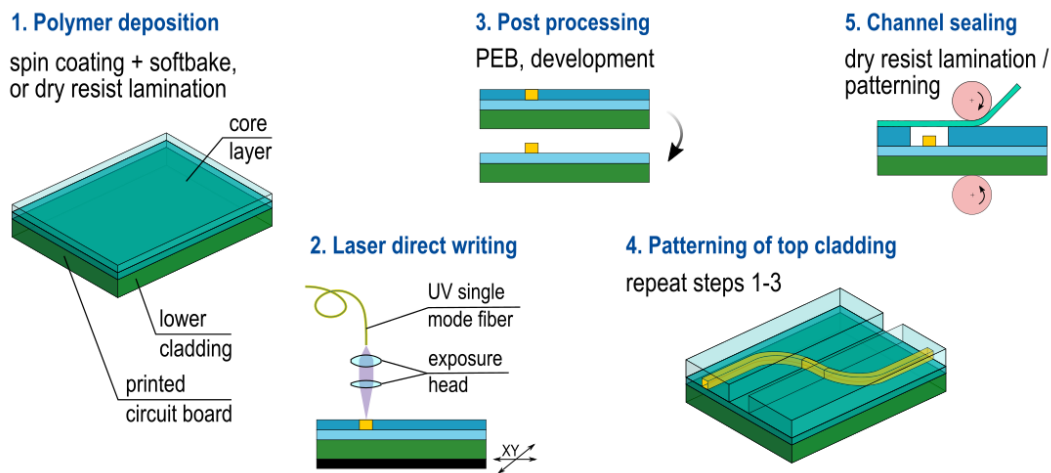


Fig. 3.1: Technological process chain for manufacturing of optofluidic sensor platform.

The standard manufacturing process chain is categorized as follows, a detailed description of the specific process parameters discussed later in this chapter:

1. Substrate preparation and spin-coating

The substrates are prepared to improve polymer adhesion. It includes chemical cleaning and physical plasma treatment, dehydration bake, and dispensing of adhesion promoter. Photosensitive resist is then spin-coated or laminated on the prepared substrate. In case of spin coating, a certain amount of the liquid photoresist is dispensed (substrate size dependent) on a fixed substrate and then the substrate is spun at a strictly defined speed. The solvent in which the photosensitive component is

^a The proposed manufacturing technology and waveguides evaluation are new research areas for the Institute of Electronic Appliances and Circuits. Materials, accessories, and some of desired equipment had to be selected and purchased or be put back into operation.

dissolved is partly evaporated during the spin coating. To remove the remaining solvent from the spin-coated resist layer, a two-ramp tempering, softbake, is undertaken.

2. Lithographic patterning: exposure

The photosensitive resist is exposed with ultraviolet (UV) radiation. This can be performed by either mask-less laser direct writing or by mask-based lithography by means of flood exposure through a pre-aligned photomask (glass or foil masks). This exposure leads to the latent transfer of the negative of photomask pattern into the photoresist layer and creates a solubility differential between exposed and unexposed photoresist parts.

3. Lithographic patterning: post processing

During exposure, a photochemical reaction of crosslinking is initiated in the photoresist. The process can be accelerated by temperature during so-called post exposure bake (PEB) tempering step. It ends irreversibly, whereby, in case of negative tone resist^a, the exposed areas become insoluble in the developer. During development, the soluble unexposed areas are removed and the latent pattern is transferred to the substrate surface.

4. Subsequently, the microchannels are structured by repeating steps 1-3 described above for the upper cladding layer.

5. Channel sealing

The fabricated microchannels are typically 100 – 500 μm wide and 50 μm deep. They must be hermetically sealed. For this purpose, epoxy resin-based dry resist could be used, because it can be easily laminated over large and inhomogeneous surfaces, and can be photolithographically patterned. These features are of a great importance for a leak-free sealing of microchannels. With the connection/gluing of fluidic connectors and tubings, the fabrication of fluidic part of the optofluidic device is completed.

The requirements for EOCB substrate and polymer materials for optical structures together with the individual technological steps and the optimized process settings are described in the following sections.

3.1 Material Selection: Optical Guiding Structures on EOCBs

3.1.1 Optical Material Requirements

The selection of a suitable optical waveguide (WG) material is a key part of the optofluidic device design process. There are several requirements of optical materials for their possible integration into a standard PCB fabrication chain. They should be applicable under clean room conditions, provide good adhesion to rigid and flexible substrate materials, and withstand mechanical treatment if needed. They should be structured by means of cost-effective fabrication techniques compatible with standard technological processes in electronic technology, such as photolithography, pressing, lamination, milling, drilling, and soldering. Optical layer deposition and waveguide patterning should be scalable to larger substrate areas [33, 77].

^a Negative tone refers to a photoresist whereby the parts exposed to UV radiation become cross-linked, while the unexposed areas of the film remain soluble and can be washed away during development.

Thermal stability is another optical material parameter important for PCB-integration. The optical materials must be able to withstand elevated temperatures during PCB manufacturing, e.g. when subjected to press-fitting of optofluidic layer to a PCB ($T \approx 180\text{ }^\circ\text{C}$), conventional short-time lead-based soldering ($T \leq 250\text{ }^\circ\text{C}$ for 2 – 3 min) or alternative soldering with low-melting tin-bismuth solders ($T \leq 170\text{ }^\circ\text{C}$ for 2 – 3 min) [6], and during system operation (temperature/humidity stability by 85 °C/85% rH test) [33]. The glass transition temperature T_g of the involved materials is therefore the critical selection parameter. Considering high possible process and operation temperatures, it is also important for optical materials to have a coefficient of thermal expansion (CTE) close to the value of PCB substrate material in order to minimize the internal stresses in light-guiding structures [44, 67].

In terms of optical properties, the material should have low intrinsic absorption at relevant wavelengths of 830 – 860 nm, 1310 and 1550 nm. Nowadays, optical glass fibers, which are conventionally used in telecommunication, exhibit extremely low propagation losses of $\sim 0.5\text{ dB/km}$ in infrared range [22]. This makes them indispensable for high-speed data transmission over long distances. In comparison to conventional glass fibers, the propagation losses in optical polymers are in the range of several fractions of dB/cm, e.g. 0.2 dB/cm for EpoCore at 830 nm [79]. This significant difference in propagation losses in visible to infrared segment of light spectrum is due to the polymer chemical structure and molecular vibrational infrared absorption [80]. The transmission losses for some optical polymers could be reduced by halogenation [67], however, material absorption remains the main issue of most optical polymers.

For light guiding by total internal reflection (for the light guiding theory see section 2.1.3), a waveguide should consist of a more optically dense material (core) surrounded by an optically less dense medium (cladding), meaning that the refractive index n of the core material is larger than cladding ($n_c > n_{cl}$). A sufficient refractive index contrast should be present. If the required contrast is not maintained, light guidance cannot take place.

Additionally, the polymer photoresists should have good chemical stability in water and alcohols. For biomedical applications, such the encapsulation and neuronal optrodes [81, 82], the involved materials should be biocompatible as well, i.e. being not cytotoxic and harmless for a patient while retaining its functionality.

3.1.2 Optical Polymers for Integrated Optics

Despite cost-effectiveness and chemical and mechanical robustness of conventional glass fibers, their size, fragility, and necessity of additional machining hinder their compact integration into complex optical circuits. Optical polymers, conversely, are a promising alternative in the field of integrated optics. Polymers are less expensive in comparison to glass but have higher absorption-induced propagation losses. Due to this material absorption issue, polymer waveguides are applied in a short-distance on-board signal transfer [83].

The number of propagation modes in an optical waveguide, i.e. single- (SM) or multi-mode (MM) operation, and light coupling efficiency correlate with its cross-sectional dimensions and refractive index contrast (refer sections 2.1.4 and 2.1.5). The polymer combination with low refractive index contrast allows fabrication of waveguides with larger dimensions yet achieving single- or few-mode operation. Polymers can also form multilayered, three-dimensional structures with vertical couplers, tapers, splitters, etc. [64]. In contrast to high refractive index silicon waveguides, which require tapers or Bragg-grating couplers for efficient light coupling to few-mode glass fibers [84], polymer waveguides

allow direct butt-coupling with fibers [64]. This makes optical polymers suitable for mass production of compact low-cost photonic circuits with extra design freedom [67].

One of the fundamental properties of polymers is their relatively large thermo-optic effect, i.e. that the refractive indices of polymers are highly temperature-dependent, at the rate of approximately 10^{-4}K^{-1} , e.g. $-7.1 \cdot 10^{-5}\text{K}^{-1}$ for EpoCore [85], while for glass they are one order of magnitude smaller [3]. This allows the fabrication of power efficient thermo-optic switches, attenuators, and tunable optical devices [86–88]. The above mentioned features make optical polymers a preferable material for cost-effective fabrication of EOCB-based optofluidic sensing platforms.

3.1.3 Overview of the Most Relevant Optical Polymers

Table 3.1 gives an overview of the optical polymers used in contemporary research activities together with their optical properties. All of them are photosensitive materials and thus can be patterned by UV light radiation using various technological processes [89].

Table 3.1: List of optical polymers and their reported optical transmission losses [90].

Manufacturer/ Commercial name	Polymer class	Optical loss [dB/cm] wavelength [nm]
Exxelis / Truemode [89, 90]	acrylate	0.04 (850)
		0.18 (800)
Dupont / Polyguide™ [67, 90]	acrylate	0.35 (1300)
		0.6 (1550)
		0.91(266)
Dow Chemical / Cytop™/Cyclotene™ [67, 90–92]	benzocyclobutene	0.77 (355)
		0.51 (633)
		0.81 (1300)
		1.5 (1550)
Epoxy Technology / Epo-Tek® OG169; 146 [93]	epoxy	0.28 (1300)
		0.26 (1550)
MicroChem Corp./ SU-8 [94]	epoxy	0.48 (850)
		0.5 (1310)
		1.8 (1550)
Micro resist technology GmbH / EpoCore, EpoClad [95–97]	epoxy	0.25 (633)
		0.36 (650)
		0.2 (830)
		0.32 (850)
		0.53 (1310)
Norland / NOA series [98]	mercapto-ester with acrylates	0.4 (633)
		0.43 (1310)
		0.51 (1550)
Dow Chemical / LightLink™ [49, 90] XP-6701A (core) / XH-100145 (clad)	polysiloxane	0.03 (850)
		0.30 (1310)
Dow Corning Corporation [29] / Silicones (OE-4141/OE-4140, WG-1017/WG-1010)	polysiloxane	<0.05 (760-860)
		0.28 (1310)
Micro resist technology / Ormocore, Ormoclad [90, 99]	inorganic-organic hybrid (silicon-containing)	0.06 – 0.1 (633)
		0.23 (1310)
		0.5 – 0.6 (1550)

Most of the optical polymers have acceptable propagation losses in range of 0.2 – 0.6 dB/cm at the typical data transmission wavelengths of 850, 1310 and 1550 nm. In close collaboration of IBM and Dow Corning Corporation, the fabrication of flexible board-level optical waveguides made of high-performance silicone polymers OE-4141 / OE-4140 and WG-1017/WG-1010 with low optical losses of 0.05 dB/cm at wavelengths of $760 \text{ nm} < \lambda < 860 \text{ nm}$ is presented [29]. These materials are still under development and not commercially available.

Since at the University of Rostock, no prior work existed on the photolithographic fabrication of polymeric microstructures, a preliminary literature review is conducted. The epoxy-based photopolymers SU-8 and EpoCore/EpoClad are chosen as a basic material combination for the fabrication of integrated optical circuits within the scope of this research project. They show slightly higher propagation losses compared to silicones OE-4140 / WG-1017 from Dow Corning Corporation (see Table 3.1) but since they are widely used in fabrication of micro-electro-mechanical systems (MEMS), establishing a new technological process chain can be supported by research articles and information obtained directly from the photopolymer manufacturer (micro resist technology GmbH).

EpoCore and optically less dense EpoClad are chemically amplified negative tone photoresists with refractive indices of 1.587 and 1.579, respectively [79, 85]. This gives the sufficient refractive index contrast of $\Delta n = 0.008$ at a wavelength of 850 nm. These resists consist of a photosensitive photoacid generator (an onium salt) and a polymeric epoxy resin dissolved in an organic solvent (gamma-Butyrolactone, GBL), which keeps the resist liquid at room temperature. When the photoresist is exposed to UV light, the photochemical reaction takes place in the exposed regions: the photoacid that is photochemically formed in the solid photoresist film opens the epoxide rings of the resist, acting as a catalyst, and promotes a cross-linking reaction that gets further activated by the thermal energy imposed during post exposure bake (PEB) process. A cross-linking process takes place between the epoxy groups creating a three-dimensional molecular network. This dense fully polymerized network becomes insoluble in the developer and resistant to acids, alkalis and solvents [100, 101].

Due to thermal stability up to 230 °C and glass transition temperature $T_g > 180 \text{ °C}$ [79, 102], epoxy-based polymers are suitable to sustain the temperature by pressing-in and short-time soldering processes, which makes them good candidates for integration into the PCB production chain. Other arguments for use of epoxy-based optical polymers are their compatibility with the existing laboratory equipment and their chemical similarity to the standard PCB material, FR-4, a glass-reinforced epoxy laminate material, which results in a better polymer layer adhesion and reduced intrinsic stresses due to their comparable coefficients of thermal expansion (see section 3.1.4).

Another applicable polymer combination could be Ormocer/Ormocore. These hybrid photoresists can be also structured with near UV light (350 – 400 nm) by laser direct writing. They are slightly more expensive than epoxy-based photopolymers and after the fabrication and evaluation environment is set up, the use of Ormocer/Ormocore can be the next step in reducing optical propagation losses.

An interesting material combination is liquid photopolymers Cytop™/Cyclotene™ with a refractive index of 1.34 at $\lambda = 589 \text{ nm}$, showing low optical losses in the wide spectral range 200 – 2000 nm, which is essential for biochemical sensing [25, 103]. Other optical photoresists from Table 3.1 are mentioned only for reference and are not considered within this thesis due to their difficult availability and lack of technological documentation.

3.1.4 Substrate Materials

The substrate material plays an important role in quality and cost-efficiency of EOCB fabrication. The surface properties, namely flatness, roughness, reflectivity and surface energy, are important for the choice of technological process parameters and necessary process steps. The most commonly used substrate materials in EOCB fabrication are silicon [36, 49], glass [44, 45, 93], poly(methyl methacrylate), PMMA [26, 90], flexible Pyralux substrates [29], and FR-4 [6, 96].

FR-4 is a glass-reinforced epoxy laminate material used for standard inexpensive PCB fabrication. Coefficients of thermal expansion in x -, y -axes of FR-4 IS400 of $CTE = 1.3 - 1.4 \cdot 10^{-5} K^{-1}$ [104] are closer to epoxy resin-based photopolymers, e.g. for SU-8 $CTE = 5.2 \cdot 10^{-5} K^{-1}$ [102] in comparison to borosilicate glass SCHOTT Borofloat 33 with $CTE = 3.3 \cdot 10^{-6} K^{-1}$ [105]. It is important for reduction of intrinsic stresses within the exposed and tempered photopolymer layers. The main disadvantage of this material is its significant roughness. However, this can be eliminated by substrate planarization with a lower polymer cladding layer.

Silicon wafers have excellent flatness, thermal and mechanical properties. The adhesion of epoxy-polymer films to silicon is better than to glass [106]. However, the silicon's $CTE = 2.6 \cdot 10^{-6} K^{-1}$ makes it less compatible with epoxy-based resins in comparison with FR-4. The main disadvantage of silicon substrate is its high price: they are approximately four times more expensive than glass and almost thirty times more expensive than FR-4 substrates of the same size. Additionally, the silicon wafers are round with limited choice of substrate diameters.

The glass substrates have the advantage of better flatness, planarity and surface quality than FR-4, as well as excellent chemical and thermal stability [105]. The transparency of the glass substrates is beneficial during the exposure process, which means that, unlike for FR-4 material, the light is not reflected diffusely by rough substrate surface. However, glass is expensive and hard to post-process (cutting, grinding, and polishing). Apart from that, the polymer to glass adhesion is poor [102, 106] and thus the glass surface requires additional multi-step treatment (see chapter 3.1) in order to assure proper adhesion.

PMMA is a transparent substrate material with $CTE = 7 \cdot 10^{-5} K^{-1}$ very close to SU-8, excellent surface flatness and roughness. However, PMMA is thermally and chemically unstable in alcohols and other solvents having the heat deflection temperature under load of 93 – 115 °C depending on the composition [107, 108]. Therefore, PMMA substrates can only be used for testing purposes as an alternative to transparent glass substrates.

For prototypes of EOCB-based lab-on-a-board devices, borosilicate glass Borofloat 33 with the thickness of 0.7 mm and FR-4 substrates with thickness of 1.5 – 2.0 mm are chosen as substrate materials. Typical substrate dimensions are $50 \times 50 \text{ mm}^2$. In this project, substrate dimensions are limited to $130 \times 130 \text{ mm}^2$ by the capacity of the chamber of spin coater used for application of liquid polymer layers. However, the limiting spin coating process, if necessary, can be replaced by a doctor blade application approach [29].

3.2 Pre-Processing: Substrate Cleaning and Adhesion Promotion

The processing starts with substrate cleaning in acetone and isopropanol (IPA). The very first problem that arose in the experimental process of polymer application is the poor adhesion of the photoresist to the substrate surface, especially, to glass substrates, which is expressed in layer

inhomogeneity and layer delamination during the separation process. Therefore, more thorough chemical and physical treatment of the substrates is conducted.

3.2.1 Chemical Treatment

In order to improve the adhesion of photoresists to glass substrates, experiments on chemical cleaning are carried out. The desired result of such treatment is a homogeneous polymer layer. For this, piranha solution is applied (3:1 mixture of 180 ml sulfuric acid H_2SO_4 (95%) with 60 ml 30% hydrogen peroxide H_2O_2). Glass substrates are left in piranha solution under room temperature for 3 hours and then rinsed with deionized (DI) water and dried in a stream of compressed air.

The left section of Fig. 3.2 shows a resulting uniform, continuous spin-coated photoresist layer (for more details about spin coating process see subchapter 3.3.1) on a piranha solution pre-treated glass substrate. The right section of Fig. 3.2 presents an inhomogeneous photoresist layer with many defects on a glass substrate that is cleaned in acetone and isopropanol (IPA) and rinsed with DI water without harsh chemical pre-treatment. The positive influence of the chemical treatment on polymer to glass adhesion can be obviously observed.

The piranha solution pre-treatment is associated with health hazards and should be performed using special chemical lab environment by trained personal. Since plasma treatment provided similar results, it is decided to clean and activate the substrates physically by means of oxygen plasma (see subchapter 3.2.2).

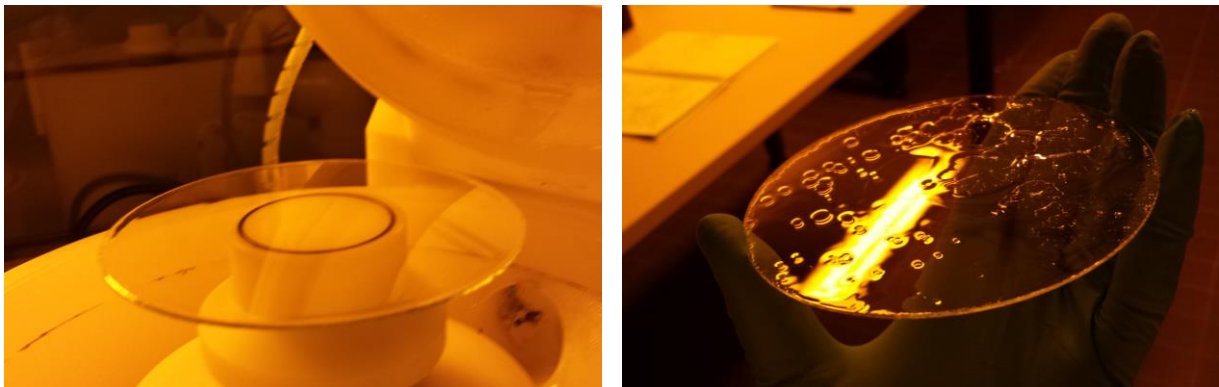


Fig. 3.2: (Left) The glass substrate chemically cleaned with piranha solution and then coated with epoxy-based photoresist showing homogeneous coating; (right) inhomogeneous photoresist layer on the isopropanol cleaned glass substrate without harsh chemical treatment.

3.2.2 Plasma Treatment

A plasma oven Femto^a, version "D" (Diener electronic Plasma-Surface-Technology GmbH), is used to remove the remaining organic residues and activate the substrate surface (FR-4, glass, lower waveguide cladding, EpoClad) to improve adhesion of the polymer to the substrate. The physical substrate surface cleaning is performed by means of ion bombardment. Herewith, the residual particles transit to a gaseous state and are sucked away by a vacuum pump.

^a The device is funded by the European Regional Development Fund

After air plasma treatment, the substrate surface shows hydrophilic wetting resulting in a significantly smaller water contact angle, which leads to significant improvement of the photoresist to substrate adhesion and helps to form a uniform spin-coated polymer layer. Plasma treatment is performed under following settings: air imitating gas mixture (nitrogen N_2 - 70%, oxygen O_2 - 30%), process pressure 0.3 mbar; power 90%, chamber temperature $T = 120$ °C for 5 min.

The air plasma treatment is also performed to the lower cladding layer (EpoClad) for adhesion improvement of waveguide cores. The process parameters are set as follows: process pressure 0.3 mbar; power 90%, chamber temperature $T = 50$ °C for 2 min.

3.2.3 Dehydration Bake

In order to achieve a good resist adhesion, it is important to remove water molecules from the substrate surface that remain after cleaning and rinsing with DI water. This procedure is implemented in a dehydration step, which takes place in a vacuum chamber of plasma oven under a low pressure of 0.3 mbar at temperature $T = 120$ °C for 30 min. Directly after the dehydration bake an air-plasma treatment is carried out. This process is especially important to FR-4 substrates, which can absorb considerable amount of moisture. The glass substrates also require the dehydration bake to insure a water-free substrate surface.

3.2.4 Application of an Adhesion Promoter

In addition to plasma treatment, MCC 80/20 primer (MicroChem Corp.) based on a combination of 20% hexamethyldisilazane (HMDS) and 80% propylene glycol monomethyl ether acetate is applied as an additional adhesion promoter. The "upwards" directed nonpolar methyl groups form a monomolecular layer on the hydrophilic substrate surface (after plasma treatment) with good resist wetting and adhesion.

The following procedure is used: a 2 ml puddle of primer is dispensed onto the 50×50 mm² substrate using a manual syringe or aerosol dispenser. The evenly distributed primer is left in contact with the surface for at least 60 s followed by two ramp spin rising: 10 s at 500 rpm, 50 s at 3500 rpm, acceleration ramp is 200 rpm/s.

The substrate pre-treatment is an essential technological step. As a result, the resist layer uniformity and the resist adhesion to the substrate surface are significantly improved: these coatings can resist the scalpel cutting, circular saw separation process, and polishing – the boundary line is not affected during these mechanical treatments and remained unchanged.

3.3 Application of Photopolymer Films

Photolithography is performed on already solid uniform photosensitive resist layers. Directly after cleaning and primer dispensing, the photoresist layer is applied to the substrate (step 1 in Fig. 3.1). The main requirements of a coating process are formation of smooth, crack- and bubble-free films, layer thickness uniformity and possibility to adjust, predict and reproduce the film thickness, and good resist adhesion to the substrate. The uniform layer of liquid photoresist with thickness within nm and μ m range can be applied to the substrate surface by different techniques: spin coating [85], drawdown / doctor blade coating technique [29], extrusion (Mosquito method) [42], and lamination [109].

Spin coating is one of the most common and well-established techniques for applying thin films to substrates and is widely used in semiconductor manufacturing and other industrial sectors. Besides some disadvantages, such as wasting of material being flung off the substrate and relatively low throughput compared to doctor blade and roll-to-roll processes, the spin coating process is a simple, fast, and reproducible technique. In this work, thin photopolymer films are applied by a spin coater WS-650-HZB-23NPP-UD3 (Laurell Technologies Corp.).

3.3.1 Spin Coating

The spin coating can be divided into several key stages: a) application of a small amount of photoresist onto the center of the static substrate (static dispense), b) spread cycle for spreading and evenly distribution of liquid photoresist, c) spin cycle dominated by radial liquid resist flow, and d) air flow driven evaporation, which ensures that the desired layer thickness and uniformity is achieved (Fig. 3.3, left).

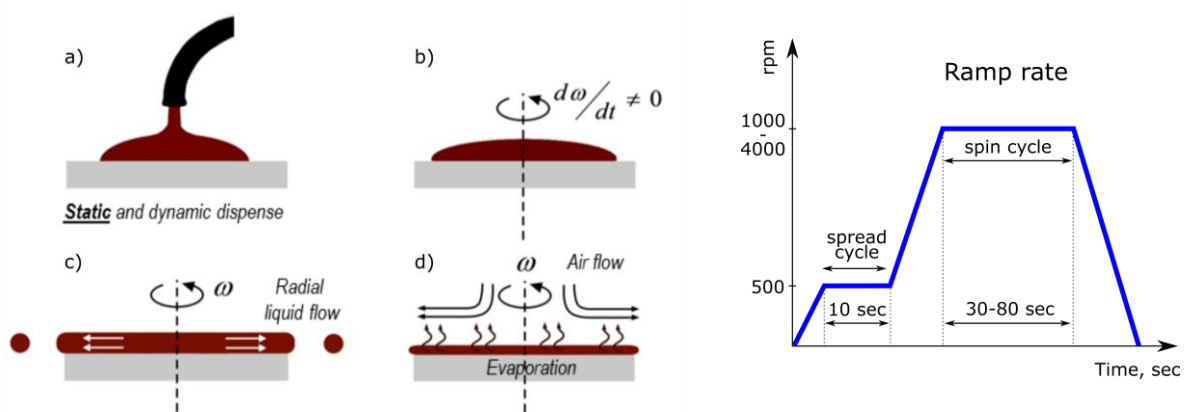


Fig. 3.3: (Left) Stages of a spin coating process: a) deposition; b) acceleration; c) flow dominated; d) evaporation dominated [110]; (right) two ramps of spin coating process: spread and spin cycles with acceleration ramps in between.

The thickness of the applied photoresist layer is influenced by several parameters. The rotation speed, spin duration and ramp rates as well as the viscosity and the surface tension of the photoresist (controlled by polymer/solvent ratio), the evaporation rate of the solvent in which the resist is dissolved are the main contributors. For sufficiently long spin time, equilibrium is established, in which the layer thickness ultimately depends only on the revolution speed and resist viscosity. The relationship between spun film thickness d and angular velocity ω may be defined as $d \propto 1/\sqrt{\omega}$, a so-called *spin speed curve* [111]. In Fig. 3.4 (left), the achieved coating thickness is shown for two SU-8 photoresists as a function of the rotation speed and the resist viscosity.

Epoxy-based photoresists are a two-component mixture of a photosensitive material and a solvent. In case of EpoCore, γ -Butyrolactone (GBL) serves as a solvent. As mentioned above, besides the spin speed, the resulting thickness depends on resist viscosity (see Fig. 3.4) and therefore on solvent concentration. For application of 3 – 5 μm thick EpoCore films, which is essential for fabrication of single-mode and few-mode waveguides, the commercially available EpoCore 50 photoresist is diluted in GBL with a weight ratio: 100 g EpoCore 50 + 27.22 g GBL. The obtained low-viscosity solution (EpoCore 5 in common notation) should be mixed carefully and left for more than 12 h in order to allow all the air bubbles occurred during intensive mixing to leave the resist mixture. In Table 3.3, the optimal spin-coating processes parameters determined for different photoresists layers are listed.

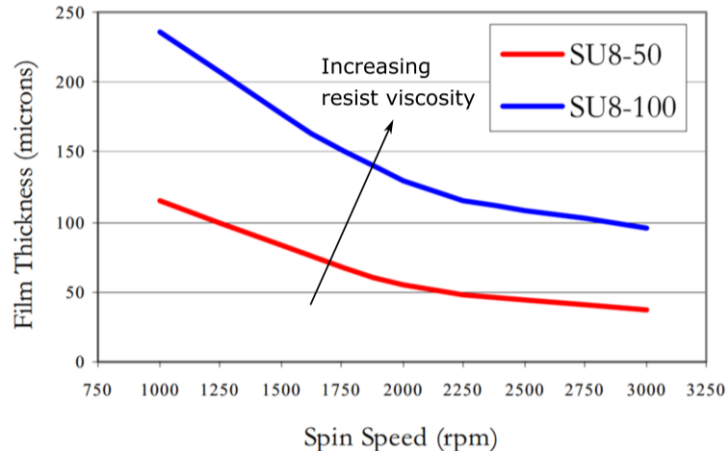


Fig. 3.4: Spin speed curves: coated film thickness vs. spin speed for different viscose resists SU-8 50 and SU-8 100 [112].

SU-8 50, EpoCore 50 and EpoClad 50 are highly viscous liquid resists with dynamic viscosities of more than $9500 \text{ mPa} \cdot \text{s}$. For covering $50 \times 50 \text{ mm}^2$ square substrate surfaces by means of spin coating, 2 ml of liquid resist are required. For multi-mode waveguides, the highly viscous photoresist (e.g. EpoCore 50) is poured out straight from the bottle. The use of the integrated syringe dispenser is avoided in order to minimize resist contact with potential contamination sources and formation of microbubbles during syringe application. In case of fabrication of single-mode waveguides, the contamination with particles in sub-micrometer size range leads to critical film defects and waveguide malfunction. Here, low-viscosity resists, such as EpoCore 5 (dynamic viscosity of $350 \pm 30 \text{ mPa} \cdot \text{s}$), are applied using manual syringe and before spin-coating additionally purified by syringe filters with pore size of $0.2 \mu\text{m}$.

Spin Coated Film Defects

Some frequently observed defects of spin-coated polymer films, which have occurred more often during optimization of the technological process, are shown in Fig. 3.5 and described below [113, 114]:

- a) incomplete coating of substrate - insufficient volume of dispensed resist (general rough rule of thumb: 1 ml resist for each inch of the substrate diameter) or poor adhesion of the film to the substrate (poor wettability), liquid resist is not being dispensed at the substrate center;
- b) pinholes, air bubbles or dust on polymer surface - dust particles in dispensed resist or on substrate surface due to poor cleansing; air bubbles could be included in the resist prior dispensing or emerge during tempering process due to missing or insufficient dehydration bake;
- c) comets and streaks on polymer surface – relatively large dust particles in the resist, spin speed and acceleration rate are too high;
- d) spiral pattern on polymer surface- due to evaporation driven surface tension effects: exhaust rate of the spin chamber is too high, spin speed and acceleration rate are too high, spin time is too short, long time between dispensing and spinning steps, an environmental effect (humidity).

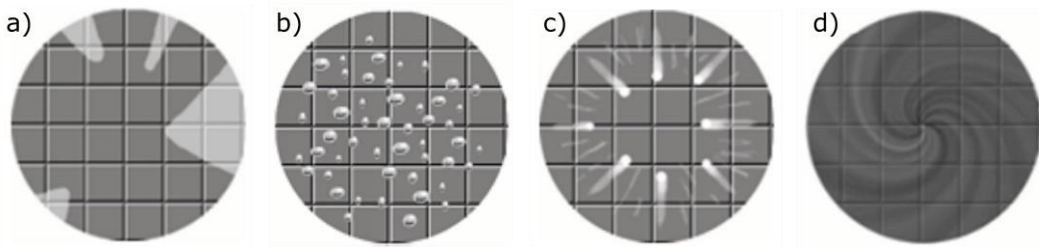


Fig. 3.5: Common deviations from the ideal spin-coated film [113].

Unstable spin parameters and too high acceleration rates may result in insufficient film quality and poor process reproducibility. Most of these defects can be prevented by working in an air-conditioned clean room facility and by filtering of coating polymers. However, the edge bead, i.e. thickening at the edges of the substrate, occurs always at the substrate rim zone, along the distance of around 5 mm from the substrate edge, where the film is 20 – 30 μm (for an EpoCore 50 layer) thicker than in the substrate center. Surface tension leads to thicker coatings at the substrate perimeter (edge effect). For square or rectangular substrates, the turbulent air flow over corners additionally disturbs the process resulting in film non-homogeneities at substrate corners. The removal of edge bead is essential for contact or proximity mask-based exposure, otherwise, it could cause mask sticking and lead to undesired gap between photomask and polymer and thus to deviations in size of exposed structures. For contact-less laser direct writing technique it is less critical, and the substrate rim zone could be cut off after processing.

3.3.2 Softbake Process

After the photoresist has been applied to the substrate, it must be softbaked to evaporate the remaining solvent and to densify the polymer film. Softbake is a two-ramp tempering process taking place on a leveled hot plate, model HPP-150-L from UniTemp GmbH. After this, the photoresist film becomes solid and ready for exposure. The necessary temperature and duration of the tempering ramps are polymer and layer thickness dependent. Table 3.3 presents the softbake temperature regimes for different photoresists and layer thicknesses.

The refractive indices of photoresist strongly depend on process conditions. The high dependence of the refractive index of the epoxy-based resist (SU-8) on the softbake temperature and exposure dosage has been reported [94, 115]. It affects the light guiding properties of the polymer waveguides and thus, the repeatability of such process parameters as temperature, ramping rate, and duration must be guaranteed for all tempering steps. For thick photoresist layers ($> 500 \mu\text{m}$), the refractive index distribution can occur within one polymer layer. For the maximal polymer layer thickness of 150 μm , the influence of softbake on refractive index distribution within one polymer layer is considered as insignificant.

3.3.3 Adjustment of Photopolymer Layer Thickness

Control of resist thickness should be performed as part of technology process optimization. Dynamic viscosity of polymers is slightly batch dependent, especially for self-mixed EpoCore 5, where the variation of a solvent weight could lead to significant deviations in viscosity and thus in desired film thickness.

Typically, the applied polymer film thickness is measured using surface profilometry. For determination of the layer thickness, the edge cavities in the resist layer are photolithographically structured by successive spin coating, softbake, exposure, and development steps. Since the desired layer thickness is a function of the rotation speed and the resist viscosity (see Fig. 3.4), the process parameters of the spin coating are optimized based on the measured thickness distribution. The rotation speed is then adjusted to ensure the desired film thickness. A surface profiler Alpha-Step 500 (Tencor Corp.) is used for tactile layer thickness analysis. It operates in the following manner: a diamond tip is moved to the area where the substrate surface is not covered with film until it touches the surface; then the diamond tip is moved horizontally over the sample recording the surface topography and edge height. As a result, the layer thickness is determined. Additionally, a digital microscope VHX-5000 from Keyence^a is used as a non-contact instrument for extensive inspection of topography profiles and, thus, can greatly facilitate the layer thickness analysis.

Beside the edge effect, the measured film thickness deviation over the substrate is less than 3 μm for 50 μm thick polymer layers and less than 0.8 μm for 5 μm thick EpoCore layers (measured on a borosilicate glass substrate with an Alpha-Step 500 surface profilometer).

3.4 Photolithography

The structuring of photosensitive polymers is performed by means of conventional mask-based or mask-less photolithographic UV exposure. As stated at the beginning of this chapter, the flexible and precise laser direct writing is used for structuring of polymer waveguides (step 2 in Fig. 3.1), while established mask-based photolithography is used for the formation of microfluidic layers (step 4 in Fig. 3.1). Here, the details, benefits, and limitations of these two technologies are discussed.

3.4.1 Mask-Based Photolithography

Mask-based photolithography is a conventional and well established method for structuring of photosensitive polymers. In this case, the mask topography is transferred to photopolymer film using flood exposure through a glass or foil photomask (depending on the desired resolution). This method has the advantage of quick and complete exposure of the entire substrate, which is essential in mass production if multiple identical substrates are processed. For fabrication of structures in μm range, chrome glass masks are required. The fabrication of such glass masks is an expensive procedure and is therefore ineffective in low to mid-volume production, in prototyping, and in the design optimization project phase. Foil photomasks are favorable in sense of production costs and could easily be re-designed. However, the structure accuracy and resolution are not guaranteed for smaller feature sizes smaller than 50 μm . In this project, foil masks are used for fabrication of structures with lower precision and sidewall roughness requirements, such as microfluidic channels and structures for coarse fiber alignment in lower and upper polymer cladding layers. Figure 3.6 demonstrates the quality of a standard foil mask fabricated at our department.

^a The device is funded by the European Regional Development Fund

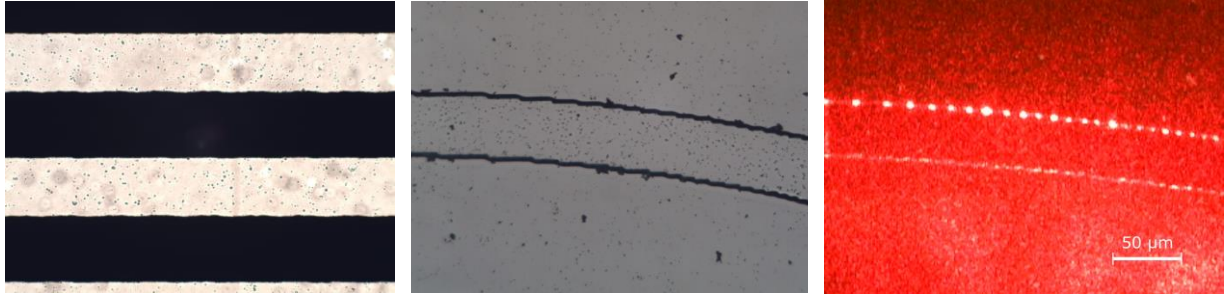


Fig. 3.6: (Left) Photograph of a foil mask demonstrating pure mask quality; (center) light microscopic image of a bent waveguide fabricated using a foil mask; (right) light guiding operation of the bent waveguide - radiation losses on a zigzag waveguide surface.

For the photolithographic structuring of photosensitive resists, the sufficient exposure time t [s] can be calculated from material-dependent exposure dose D [mJ/cm^2] recommended in a corresponding data sheet and the light intensity I [mW/cm^2] of the UV source as follows:

$$t = \frac{D}{I} \quad (3.1)$$

In conducted experiments, a flood exposure unit Typ 2004 (Welisch Elektronik GmbH) with broadband mercury vapor lamps serves as a UV radiation source and gives the possibility of a contact exposure through a photomask. The light intensity of the mercury vapor lamps is measured as $I_{365 \text{ nm}} = 4.7 \text{ mW}/\text{cm}^2$.

For a EpoClad 50 layer with a recommended exposure dose of $D = 500 \pm 100 \text{ mJ}/\text{cm}^2$ [116], the calculation gives a wide range of possible exposure times $t = 85 - 128 \text{ s}$. Therefore, the optimal exposure time leading to a better topographical result should be determined experimentally. Accomplish this, series of foil mask-based exposures of an EpoClad 50 layer are performed. Exposure times slightly deviating from the calculated values are tested. In the following, the cross-section profiles of the obtained structures are analyzed. As a result of insufficient exposure dose, the fabricated structures will not have desired steep vertical profiles, but rather be trapezoidal having overhangs or undercuts, concave or bell-shaped, and be wider / narrower than intended.

From these exposure series, the resolution limit for the particular layer thickness and the foil mask quality can be specified by determination of the minimal distance at which the adjacent microstructures are still separated. The experimental optimization of exposure time for EpoClad 50 layer yielded $t_{\text{EpoClad 50}} = 90 \text{ s}$ with the resolution limit of $50 / 50 \mu\text{m}$ for line width / space width.

3.4.2 Laser Direct Writing Setup for Mask-less Lithography

In case of the dynamic, flexible, and accurate laser direct writing approach, a focused laser beam is used to "write" the desired patterns and moves relatively to the photopolymer layer. The velocity of the relative substrate to laser beam movement is called *writing speed*. During the exposure, the laser beam profile and trajectory will be latently transferred into the photopolymer layer. It therefore belongs to a group of mask-less photolithography techniques. This highly versatile approach eliminates some of the disadvantages of a mask-based photolithography, such as inflexibility, high mask production costs, and limited mask size. For multilayer systems, the mask-based technology can fail if masks do not match due to distortions; in contrast, for laser direct writing, a linear distortion correction can be easily carried out on a CAD layout via scaling and rotation resulting in

higher yield. Using this technique, different waveguide widths can be achieved with the same setup, just by changing the focusing lens or relative substrate-to-exposure head position. It is more suitable for fabrication of polymer waveguides and EOCBs on large scale substrates than mask-based lithography. However, the laser direct writing exposure technique is less accurate (resolution of nm by mask-based lithography vs. μm by laser direct writing), not extensive, and thus takes considerably longer time (minutes vs. seconds) compared to the conventional mask-based exposure.

There are commercially available mask-less exposure systems, e.g. MLA series (Heidelberg Instruments) and the PicoMaster line (4PICO B.V.). They are made for industrial applications, have an internal alignment system, enable fast writing speeds, and are equipped with a suitable UV-light source (g-, h-, i-lines). However, complementary to high purchase costs, to our knowledge, they all use rasterizing and stepping, which means that the fabrication of smooth bent structures is impeded. Furthermore, most of them are constructed for a substrate size up to 8 inch having quite limited working area.

In order to eliminate these problems, a customized laser direct writing system illustrated in Fig. 3.7 is designed, assembled, and built in-house mainly by Dr. rer. nat. H. Hartwig with some ideas and suggestions from the author. It enables writing of complex trajectories by linear servomotors and position changes in four degrees of freedom (rotation and x, y, z), and precise laser beam alignment relative to the pre-structured patterns on the substrate surface.

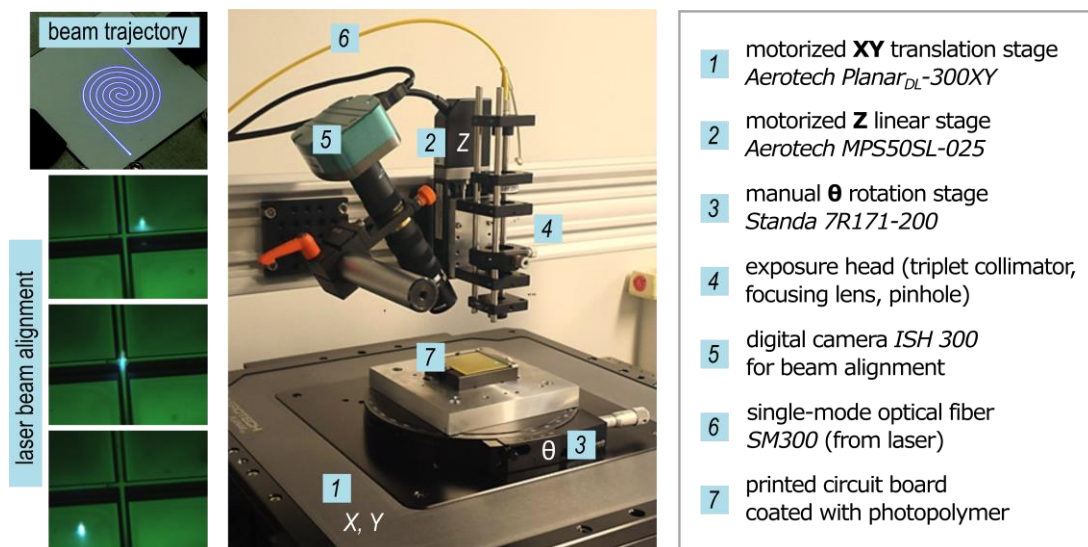


Fig. 3.7: Laser direct writing setup and its components; an example of a programmed beam trajectory and demonstration of a laser beam to a pre-defined microstructure (cross) alignment.

The light from the stable Omicron LuxX 375-20 diode laser with maximal optical power of 20 mW in continuous wave mode emitting at the wavelength of 375 nm is guided to an exposure head by means of a single-mode SM300 fiber with operating wavelengths of 320 – 430 nm (Thorlabs, Inc.) having a FC / APC connector on the laser side and a FC / PC connector on the exposure side. The exposure head is a multi-lens system for collimation, shaping (e.g. by means of an optional pinhole) and direct beam focusing of the laser light onto the photosensitive film. The output of the optical fiber is focused on a TC06FC-405 triplet collimator (Thorlabs, Inc.), which in turn collimates and widens the laser beam. The collimated laser beam is then led to a focusing lens (LBF254, Thorlabs, Inc.). The focusing lens is chosen in terms of focal length (50, 75 or 100 mm) depending on a desired


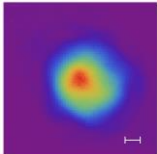
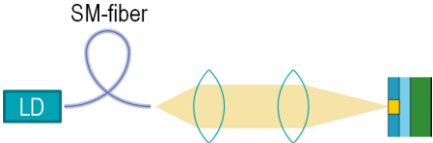
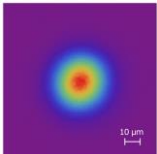

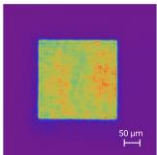
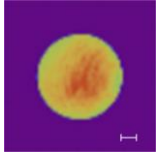
writing distance and a laser spot size (8 – 50 μm). The focusing lens forms a spot of the required diameter onto the substrate surface coated with a photoresist. The substrate is held by a manual rotation stage (Standa 7R171-200), which in turn is fixed on a computer-controlled direct-drive linear stage (Aerotech Planar_{DL} 300 XY). The translation stage follows a CAD-based trajectory. The change of the relative vertical exposure head to substrate surface position is performed by motorized linear z-stage (Aerotech MPS50SL).

The exposure dose absorbed by the resist layer during laser direct writing depends on the set laser power, writing speed, single or multiple exposure, and relative vertical position of the exposure head (focus position). The optimal exposure parameters for fabrication of vertical waveguide profiles can be defined from the analysis of the structure profiles obtained from the series of exposure tests, which could be performed on one substrate. The adjustment of laser beam profiles and the determination of the exact process parameters will be discussed later in this section.

Laser Beam Shaping

The UV-laser beam is shaped by the exposure head (position 4 in Fig. 3.7) and focused on the pre-coated substrate surface. There are three principal concepts for laser beam formation within the exposure head. They are schematically shown and described in Table 3.2.

Table 3.2: Laser beam shaping concepts and application examples.

Approach	Properties and typical applications	Setup scheme	Laser intensity distribution
Direct laser diode light \rightarrow collimator, focusing	<ul style="list-style-type: none"> • High power, higher writing speed • MM WGs / typical laser diameters 18-35 μm ($1/e^2$) 		
Laser diode beam through SM-fiber \rightarrow collimator, focusing	<ul style="list-style-type: none"> • High quality rotationally symmetric Gaussian beam, limited power • SM WGs / focusing down to 8 μm ($1/e^2$) 		
Direct laser diode light \rightarrow collimator, pinhole (square, circular), focusing	<ul style="list-style-type: none"> • Rectangular and circular beam profiles, lower writing speed, long exposure cycle • WGs with different end-faces (flat, curved) 		 square aperture  circular aperture

The most common configuration is writing with a focused Gaussian beam. It is used for structuring of continuous single- and multi-mode waveguides with various trajectories. In this case, two setup variations are possible:

1. Focusing of the light coming directly from the UV-laser diode using exposure head optics. Here, maximum laser power is not limited by the damage threshold of a glass fiber, and thus a higher writing speed can be set resulting in a reduction of exposure time. However, a non-homogeneous and slightly asymmetric laser beam spot is observed;
2. Additional laser beam filtering using a single-mode optical glass fiber SM300. This has the advantage of producing the mode-filtered and rotationally symmetric laser intensity distribution. However, the use of a single-mode fiber and lenses leads to additional light insertion losses, and limits the maximum laser power to 10 mW. Thus, it results in a significant decrease of the maximum writing speed and an extension of the exposure time.

An ideal Gaussian beam implies a Gaussian intensity profile (Fig. 2.8). During the laser direct writing with a Gaussian laser beam, the resist regions receive a different exposure dosage. In order to achieve a more homogeneous intensity distribution within the focused laser beam spot (top-hat like laser profile) [117] and different laser spot shapes, circular and rectangular apertures can be integrated in the optical exposure head. These are used in the third exposure head configuration, see Table 3.2. It is implemented as follows: the UV laser beam, coming straight from the laser output, passes to the collimator, where it is expanded to 1.1 mm in diameter and then reaches the aperture. Here the outer parts of the Gaussian laser beam are cut off and more homogeneous inner part passes through the aperture and is focused on the substrate surface. This configuration is used for fabrication of waveguides with curved and flat end-faces.

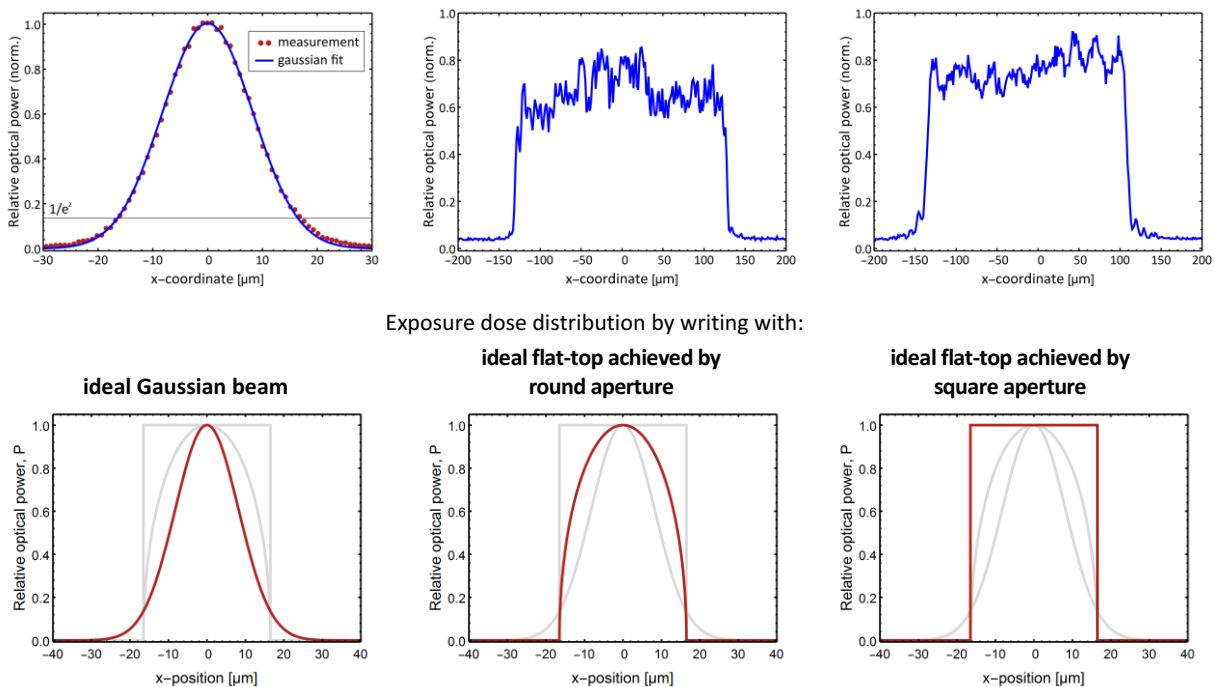


Fig. 3.8: (Left) Normalized Gaussian beam and flat-top profiles achieved by round aperture $\varnothing 250 \mu\text{m}$ (center) and $250 \times 250 \mu\text{m}^2$ square aperture (right), pictures of laser beam power distributions are taken by CMOS camera; (below) comparison of integrated laser power distribution along writing trajectory obtained on the substrate by writing with ideal Gaussian beam, round and square flat-top laser profiles with equal diameter of $33 \mu\text{m}$.

The polymer cross-linking takes place in the regions where the effective threshold exposure dose D_o (i.e. the minimum exposure dose required for complete cross-linking) is exceeded. During the laser direct writing process with a focusing Gaussian beam, the exposure density distribution over the laser spot is linearly dependent on irradiance distribution (laser cross-sectional profile): $dD = I(\rho) \cdot dt$, where $\rho = \sqrt{x^2 + y^2}$ is the polar coordinate [118, 119]. The exposure dose absorbed by a polymer layer during the laser direct writing process can be estimated by integration of a laser beam profile over the writing trajectory. Fig. 3.8 shows a comparison of the resulting power distribution on the substrate surface by writing with a Gaussian beam and with circular flat-top laser profiles. Ideally, steep flat-top like profiles can be obtained after integration with a square laser spot (rectangular aperture) or by having a rotationally symmetric flat-top profile with a dent in center. The implementation of the laser beam profile with a dent is not a trivial task and requires a complex optical system.

The flat-top profile delivers better exposure beam quality in terms of edge steepness and uniformity of intensity distribution within the laser spot. The exposure dose fluctuations within the exposed photopolymer area can lead to refractive index inhomogeneities in the structured waveguide core (see section 3.4.3), increased sidewall's roughness, and tilted sidewalls. The integration of an aperture for beam shaping in turn causes drastic drop in light power, which consequently reduces the writing speed and therefore extends the exposure cycle up to 10 times (up to 1 h for one substrate $50 \times 50 \text{ mm}^2$). However, it enables the fabrication of homogeneous polymer waveguides with smooth and nearly vertical sidewalls (slope less than 2°); discontinuous waveguides with different end-face geometries (flat and curved) could be fabricated.

Laser Beam Parameter Calculation

The laser beam, diameter and intensity distribution should be constantly monitored and analyzed. For this purpose, a modified Omnivision OV5647 CMOS sensor with removed Bayer color filter is attached to a Raspberry Pi computer and used as a beam profiler^a. However, its pixel pitch of $1.4 \text{ }\mu\text{m}$ is not sufficient for precise direct measurement of the beam's waist diameter that is expected to be a few micrometers.

To overcome this limitation, pictures of the laser beam power distribution are taken in many planes perpendicular to the vertical optical axis z around the minimum beam waist and subsequently analyzed numerically. According to ISO 11146-2: 2015 [76], the laser beam radius w in each plane is defined using a Gaussian fit as the position where the intensity I drops to $1/e^2$ times the maximum value I_0 . Based on an analytical expression for beam radius given in equation (2.21), the fitted function takes the form (see Fig. 3.9):

$$w(z) = 4.02 \sqrt{1 + \left(\frac{z-23.08}{0.14}\right)^2} \quad (3.2)$$

Therefore, the beam waist radius is found to be $w_0 = 4.02 \text{ }\mu\text{m}$. The Rayleigh length and depth-of-focus (equation 2.23) are determined to be $z_R = 140 \text{ }\mu\text{m}$ and $b = 280 \text{ }\mu\text{m}$. In this fit, z corresponds to the exposure head position along vertical axis where $z = 0$ defines its home position. Therefore,

^a Beam profiler with the modified chip and the Python readout script are provided by Dr. rer. nat. H. Hartwig.

the optimal exposure head position is $z_{\text{opt}} = 23.08$ mm with tolerances of ± 140 μm for motorized z -axis.

As the exposure beam is filtered by an UV single-mode fiber, a nearly diffraction-limited spot size below 1 μm is achievable by only minor modifications of the exposure head or utilization of lensed glass fibers. However, according to the beam parameter product invariant given in equation (2.25), a narrower focusing will result in shorter depth-of-focus. The tightened tolerances in z -position are difficult to meet due to substrate non-planarity and thickness deviations in spin-coated polymer layers. The typical tolerance of substrate and polymer thicknesses is ± 50 μm . With these z -tolerances and using equation (3.2), the variation in estimated laser spot radius is 4.02 ± 0.25 μm .

The accuracy of the XY-translation stage is 0.1 μm and the laser beam diameter is approximately 8 μm . These parameters of the laser direct writing setup enable UV-structuring of polymer-based single-mode waveguides (see section 3.4.5).

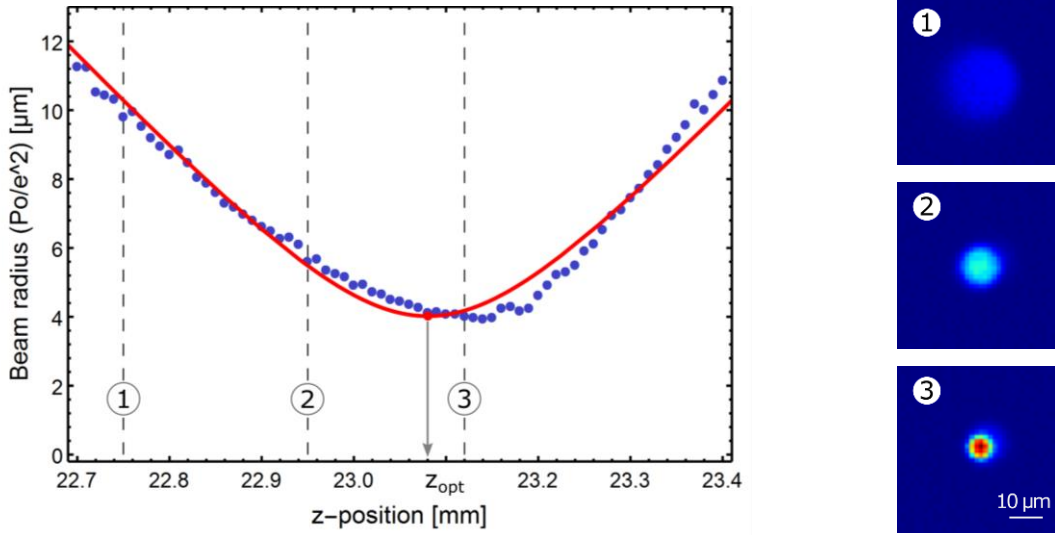


Fig. 3.9: (Left) The laser beam radius measured using Raspberry Pi CMOS chip for beam profiling (blue points) and an analytical fit for Gaussian beam (red line); (right) pictures of laser beam power distribution (P_o) taken by CMOS chip at different standoff distances to the substrate (at constant exposure settings).

Threshold Model for Structure Dimensions and Exposure Series

The quality and dimensions of polymer optical structures obtained by laser direct writing are determined by the exposure dose D [mJ/cm^2], which is controlled by the writing speed of the UV laser, the optical laser power and the laser intensity profile, laser spot diameter, and standoff distance to the substrate (vertical z -coordinate).

Prediction of laser written waveguide core sizes for rotational symmetric laser beam spots (see Fig. 3.10, left) is based on an analytical model reported earlier [119, 120], where the Gaussian beam irradiance profile is given by:

$$I(\rho, z) = \frac{2P}{\pi w^2(z)} \exp\left[-\frac{2\rho^2}{w^2(z)}\right], \quad (3.3)$$

where P is the laser power, $w(z)$ is the beam radius along the vertical position z , x and y are the distances from the spot center along the horizontal axes, and $\rho = \sqrt{x^2 + y^2}$ is the polar coordinate.

In case of fixed vertical position ($z = \text{const}$) and writing direction x with a writing velocity defined as $v = dx/dt$, the exposure dose D at each x is given by:

$$dD = I(\rho) dt \rightarrow D(y) = \int_{-\infty}^{+\infty} I(\rho) dt = \sqrt{\frac{2}{\pi}} \frac{P}{vw} \exp\left[-\frac{2y^2}{w^2}\right] \quad (3.4)$$

For $D(y_0) = D_0$ (threshold dose), the equation (3.4) returns the line width b and the writing velocity v of:

$$b = 2y_0 = w \left[2 \ln \left(\sqrt{\frac{2}{\pi}} \frac{P}{D_0 w v} \right) \right]^{1/2} \quad (3.5)$$

$$v = \sqrt{\frac{2}{\pi}} \frac{P}{D_0 w} \exp\left[-\frac{b^2}{2w^2}\right] \quad (3.6)$$

The required exposure dose recommended by manufacturers lies in a relatively broad range of values, e.g. 200 – 400 mJ/cm² for SU-8 [102] and 350 – 500 mJ/cm² for EpoCore 50 [85]. Therefore, aforementioned formulas can provide only preliminary assumptions. To determine optimal writing parameters, exposure series are performed with various positions of exposure head (z) and writing velocity while the laser output power is hold constant. A significant advantage of laser direct writing approach over mask-based alternative is that tests with various exposure settings can be performed the same substrate.

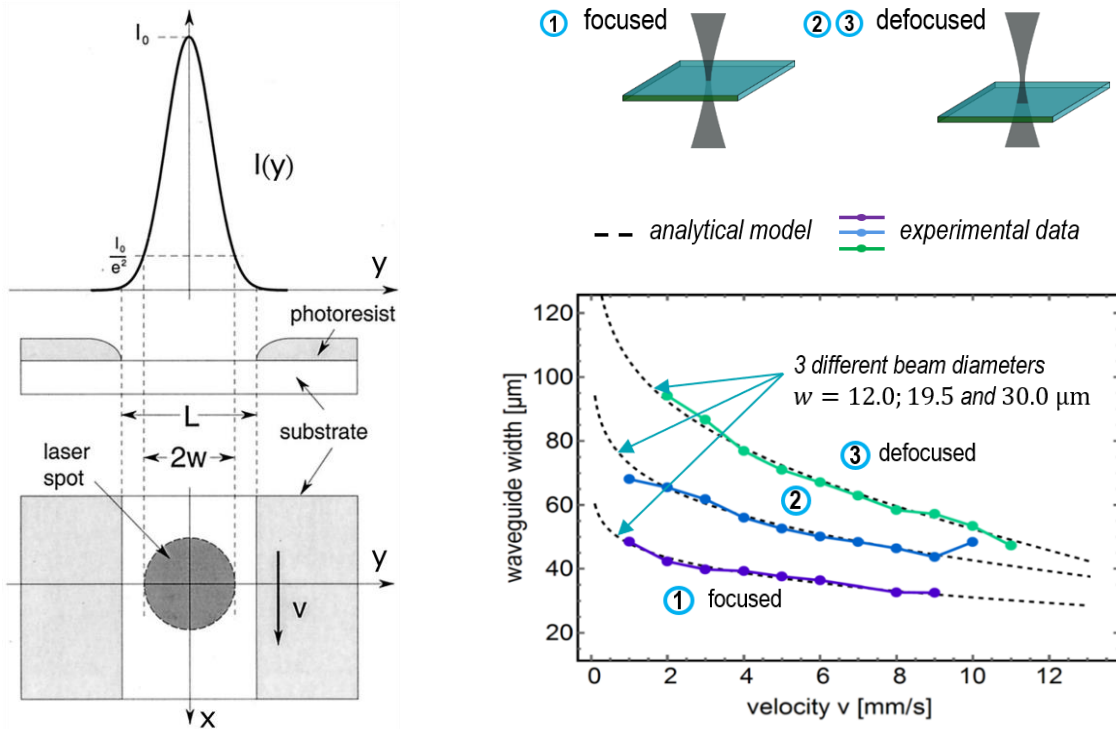


Fig. 3.10: (Left) Schematic of the structure written with a Gaussian beam laser profile [119]; (right) the achieved waveguide's widths for laser power $P = 2.1$ mW as a function of writing velocity and spot diameter (focused or defocused $w = 12.0; 19.5$ and 30.0 μm). The prediction from the analytical model (dashed lines) agrees well with experimental data (colored lines).

The results based on (3.5) and (3.6) reproduce the experimental data very well for independently determined w , D_0 and P (see Fig. 3.10, right for SU-8 waveguides). The threshold exposure dose

$D_0 = 260 \text{ mJ/cm}^2$ provides the best correspondence between calculated and measured values^a. A strong dependence on beam diameter, i.e. on the standoff distance to the substrate (z), and on the writing speed is observed. The deviation from the optimal focus position increases the diameter of the writing beam spot and it is possible to get wider waveguides, if the received exposure dose is sufficient for entire layer polymerization ($D \geq D_0$). Contrariwise, the increase of writing speed results in narrower waveguide structures (see Fig. 3.11). A very high writing speed ($v > 12 \text{ mm/s}$) results in insufficient exposure dose ($D < D_0$) and, therefore, leads to incomplete layer polymerization. All polymer regions, where the threshold value is not exceeded, will be washed away in the developer.

Fig. 3.11 represents rectangular cross sections and a top view of a waveguide array fabricated within one exemplary exposure series of varying writing speed in $\Delta v = 1 \text{ mm/s}$ steps, while the z -position and laser intensity remain constant.

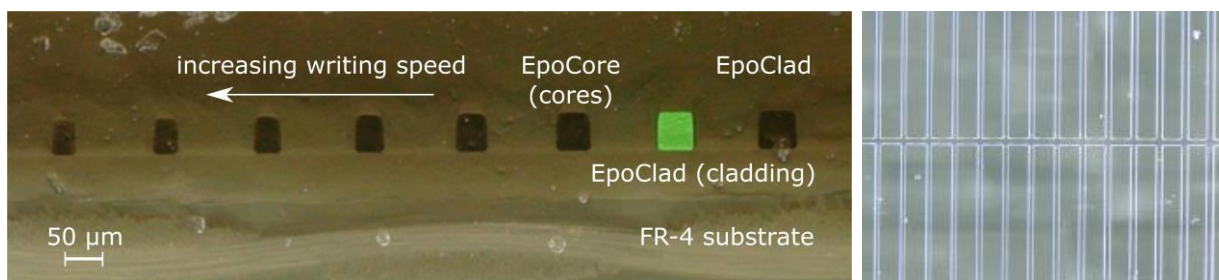


Fig. 3.11: An optical microscope image of array of waveguides with varying writing speed ($\Delta v = 1 \text{ mm/s}$) steps fabricated within one exposure series resulting in differences in waveguide's widths: (left) cross sections; (right) top view of the waveguide array.

Program Code Design for Laser Direct Writing

Layouts of optical circuits are created with the help of computer-aided design (CAD) software, e.g. in AutoCAD. The designed patterns in DXF/DWG vector format are converted by means of Aerotech's CADFusion software into the Aerobasic motion code format compatible with Aerotech actuators and translation stages. Minor changes are made manually to control the laser (to turn it on and to switch it off with coordinate's reference). The existing coordinates are supplemented with movement parameters, such as homing positions, velocity, and acceleration profiling.

Y-splitters (1:2) have two arms with curved paths defined by a cosine function with continuously changing radius for minimization of propagation losses due to the mode-mismatch and radiation [121]. They are fabricated by writing one half connected to a straight line, and subsequently the second half as it is shown in Fig. 3.12 (left).

^a The waveguide's width measurements are performed by M.Sc. Nils Thomas in frame of his master thesis and the fitting parameters (threshold exposure dose) of the analytical model are found by Dr. rer. nat. H. Hartwig.

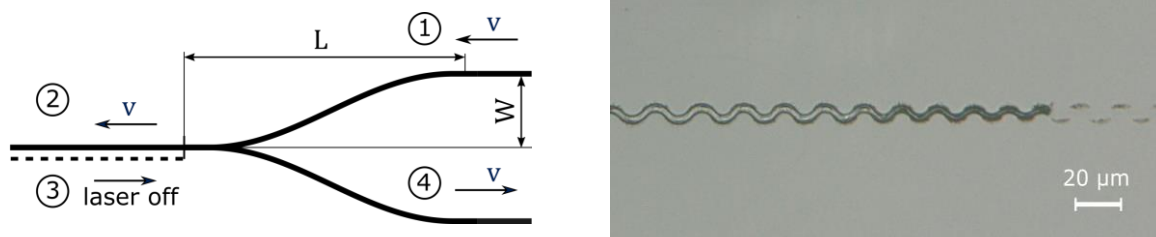


Fig. 3.12: (Left) Schematics of a Y-splitter profiling sequence generated by two cosine functions; (right) exposure result at not sufficient profiling velocity leading to a bump vibration.

The writing sequence is divided into 4 steps: 1 – one arm, cosine function following the half-period of a cosine function in form $f(x) = W/2 \cos(\pi x/L)$, where W is the width of the bent section and L is its length; 2 – straight region; 3 – straight region, movement in the opposite direction (laser off); 4 – second arm, cosine function. Incorrect writing settings (velocity profiling, de/acceleration rates) can lead to vibration during the writing process and thus undesired deviations in the written structures. Fig. 3.12 (right) demonstrates the defect caused by improperly specified velocity profile during step 2 to 3 transition when an overly fast 180°-turn causes the bump vibration.

3.4.3 Post Exposure Bake Process

Since photopolymer properties (thermal stress, thickness, refractive index, sidewall roughness) are very sensitive to process profiles and temperature, tempering processes, such as soft-and post exposure bake (PEB), besides the exposure dose, play an important role in the formation of homogeneous, smooth, and crack-less core profiles with steep side walls ($> 88^\circ$ inclination) [122].

PEB (step 3 in the process chain shown in Fig. 3.1) is required for chemically amplified negative tone resist, such as SU-8 and EpoCore/EpoClad, and provides the heat needed for a photoacid diffusion and amplification. PEB is performed at a temperature slightly above the glass transition temperature T_g of a photopolymer, which intensifies the rearrangement of the overexposed and underexposed resist molecules. However, over-baking will cause polymerization and slows down or even stops the photoresist development [118, 123]. Table 3.3 presents the temperature regimes for different photoresists layers. To inhibit the diffusion of photoacid generator, the temperature must be increased slowly with the recommended heating rate being $4^\circ\text{C}/\text{min}$.

In order to prevent crack formation and delamination (see Fig. 3.13) due to intrinsic thermal stresses caused by differences in coefficients of thermal expansion of polymer and substrate and by the cross-linking process, it is important to control not only the heating ($4^\circ\text{C}/\text{min}$) but also the cooling rates ($2^\circ\text{C}/\text{min}$). In order to reduce the internal stresses in the polymer layer, the coated substrate should be left on the hotplate for relaxation after each tempering step (softbake, PEB). The relaxation duration depends on resist thickness and maximal tempering temperature and can last from 30 min to 60 min.

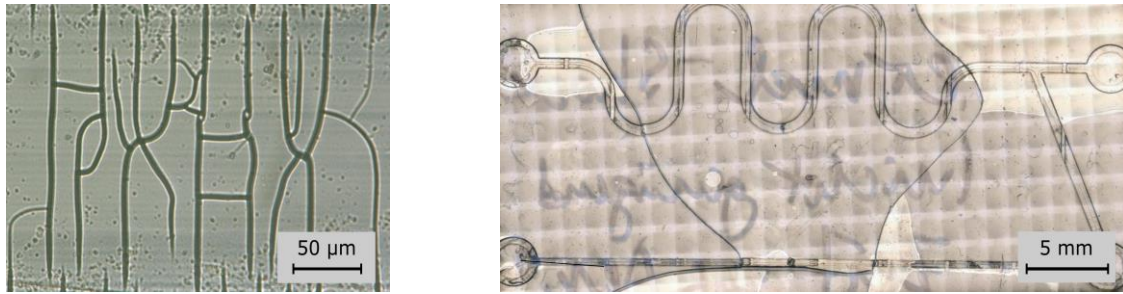


Fig. 3.13: Micro- and macrocracks in an EpoCore 50 layer due to too fast cooling during the PEB.

The dependence of the refractive index of epoxy-based photoresists on the process temperature (PEB), on the exposure dosage and on the temperature and exposure-driven intrinsic stress for SU-8 is shown in Fig. 3.14 [94]. These graphs clearly show that the process temperature should be carefully controlled in order to get reproducible results.

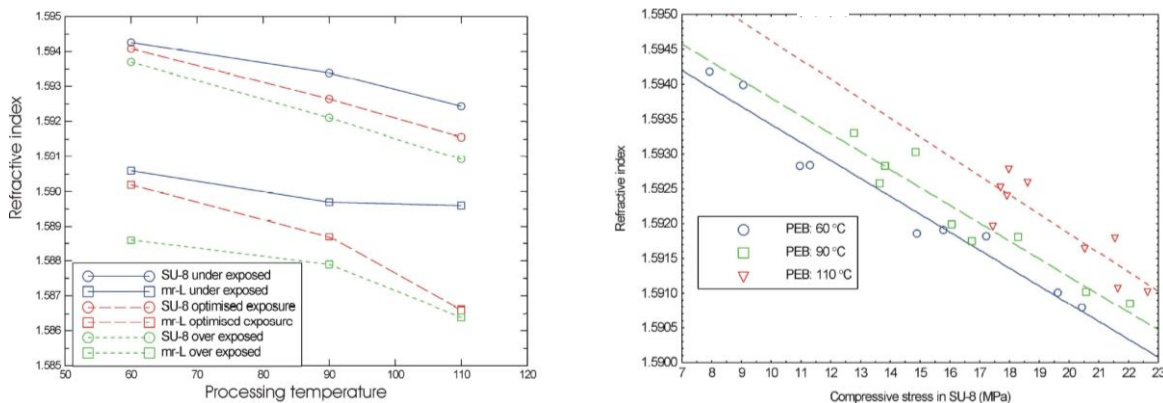


Fig. 3.14: (Left) Influence of the PEB temperature and exposure dose and (right) of the thermal stress in polymer film on refractive index of epoxy resin (SU-8) [94].

For calculations and waveguide design, the data from scientific reports of Microresist Technology GmbH is used; namely, the refractive indices of exposed EpoCore/EpoClad at a wavelength of 850 nm are $n_{\text{EpoCore}}/n_{\text{EpoClad}} = 1.5834/1.5708$ and $1.5766/1.5644$ at 1310 nm [53].

Inhomogeneities within a Core

The visually noticeable “double-core” effect (the waveguide core exhibits areas with presumably different refractive indices, Fig. 3.15, left) occurs in laser written waveguide cores after PEB with settings recommended in the supplier’s processing guide. It is worth mentioning that the “double core” effect does not appear if the waveguides are structured by flood exposure through a foil mask. This effect was also observed on pictures of several scientific publications related to laser direct writing [29, 117, 124–126], but, to the author’s knowledge, has not been described so far. Since the refractive index of the exposed epoxy resin depends on the exposure dose, it is assumed that the refractive index variations within laser written cores are caused by an inhomogeneous intensity distribution during the exposure with a Gaussian beam: the central part of the structures is overexposed, while at the edge region the exposure dose is only reaching its threshold value. In combination with insufficient thermal diffusion during too short PEB ramps, it may lead to refractive

index inhomogeneities within a laser written core. However, it remains a hypothesis and should be investigated thoroughly in future work by measuring the refractive index distribution.

This initially unfavorable effect could be used for structuring of Bragg gratings and core-within-cladding waveguides by two-step (laser direct writing and flood exposure) exposure-induced refractive index index modification [127]. However, the "double core" effect should be avoided for sensor applications, especially for measurements using absorption of evanescent fields, because it prevents interaction between fluid and light on fluid-core interface.

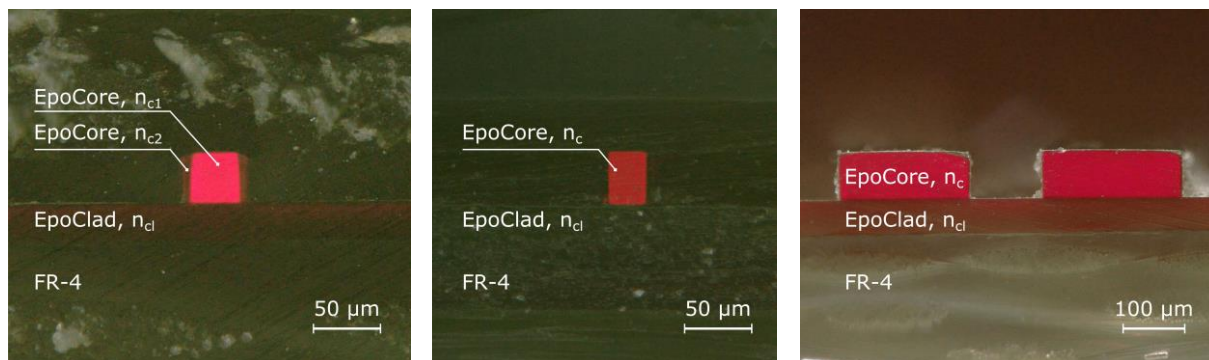


Fig. 3.15: The PEB process setting's influence on refractive index distribution within the waveguide core: (left) exposure with a Gaussian beam, PEB according to supplier's processing guide, presence of "double core" effect; (center) exposure with a Gaussian beam, optimized PEB process, less pronounced/no "double core" effect; (right) exposure with a top-hat like laser beam profile achieved using $\varnothing 200 \mu\text{m}$ aperture, no "double core" effect.

In order to prevent the formation of these inhomogeneities within a core, the parameters of two-ramp PEB process stated in the supplier's processing guide are modified. Extended duration of both process stages leads to significantly better results considering the refractive index inhomogeneity and also to minimization of stress gradients formed in polymer film while exposure and cross-linking. The optimized PEB settings for involved photopolymers are listed in Table 3.3, e.g. for EpoCore 50: The first ramp at $T_1 = 50^\circ\text{C}$ for 10 min (originally 5 min) and the second ramp at $T_2 = 85^\circ\text{C}$ for 20 min (originally 7 min). On the left and central microscopic pictures of Fig. 3.15 the cross-sections of two straight waveguides exposed with a Gaussian beam, tempered by different PEB process, settings can be compared. The qualitative improvement in terms of presumable refractive index homogeneity within the core is observed: inhomogeneities are less pronounced or not visually recognizable in case of PEB with optimized parameters.

As a consequence, reducing intensity gradients within the laser beam spot, e.g. by using apertures, significantly improves refractive index homogeneity. Fig. 3.15 (right) shows the homogeneous cross-section of a straight waveguide fabricated with a laser profile obtained by a circular pinhole with a diameter of $200 \mu\text{m}$. The best results could be achieved by exposure with a top-hat like laser profile (see section Laser Beam Shaping).

3.4.4 Development

Epoxy-based photopolymers are negative tone photoresists, i.e. the unexposed regions are washed away from the substrate surface by a wet chemical development process. The development of EpoCore/EpoClad and SU-8 polymers is performed in the same mr-Dev 600 solution (Microresist Technology GmbH). This technological step was adopted from recommendations and optimized only

for layer thicknesses not specified in the datasheet. Table 3.3 details the development duration, along with other technological process parameters.

3.4.5 Towards Single-Mode Waveguides

Single-mode waveguides are essential for many photonic sensor applications. The possibility of fabrication of single-mode waveguides using available equipment is studied in this section. For this purpose, the 3 – 5 μm thick layer of EpoCore 5 solution is spin-coated (see section 3.3.1) on a FR-4 substrate that is planarized with an EpoClad 50 cladding layer. The exposure is performed by a Gaussian beam with diameter of 8 μm . As a result, optical waveguides with cross-section of $3.5 \times 6 \mu\text{m}^2$ are structured. The single or few-mode light propagation in these waveguides is discussed in section 4.4.

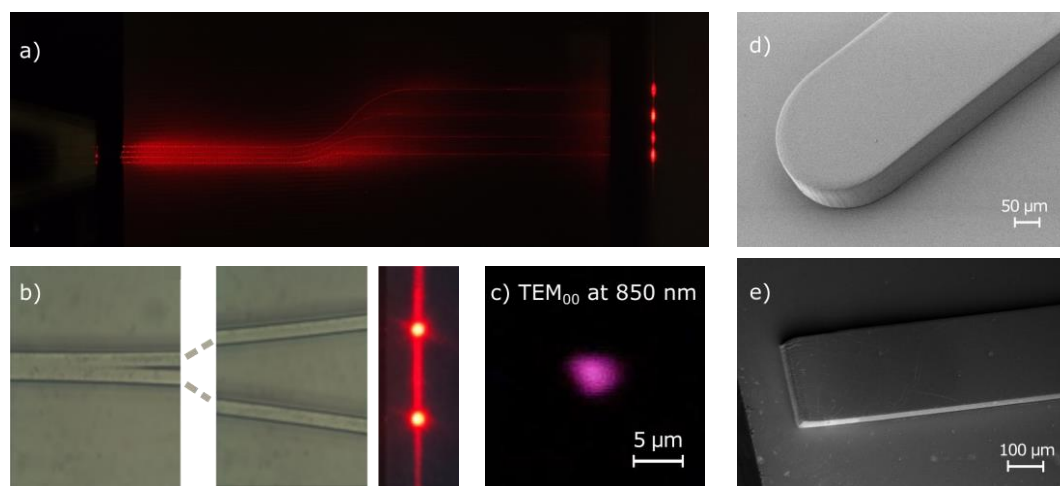


Fig. 3.16: Geometrical variety of structures fabricated by laser direct writing approach: a) S-shaped waveguides (picture performed by multiple exposure, taken by Dr. rer. nat. H. Hartwig), b) Y-splitters, c) single-mode waveguides and multi-mode discontinuous waveguides with d) curved and e) flat end-faces (SEM pictures).

In summary, the custom-designed laser direct writing setup completely built in-house enables fast and precise UV-structuring of optical microstructures. Fig. 3.16 demonstrates the variety of fabricated optical structures, e.g. straight, S-shaped, and bent waveguides or Y-splitters, single-mode and multi-mode waveguides with different end-face geometries (curved or flat-ended) and free space propagation region. The optical and mechanical characterization of the fabricated optical guiding structures is detailed in chapter 4.

Table 3.3: Overview of optimized technological process settings for EpoClad/EpoCore in different thicknesses

*self-mixed thin EpoCore; flood exposure with the light intensity of 4.7 mW/cm^2 , v_l – line writing speed, v_{ef} – writing velocity of waveguide’s end-faces.

Material / thickness	Spin Coating	Softbake	Exposure	Post Exposure Bake	Development
EpoClad 15	500 rpm for 15 s 5200 rpm for 60 s	5 min at 50°C 12 min at 120°C relaxation 30 min on a hotplate	Flood exposure: 60 s performed in two steps with 3 min pause between	3 min at 50°C (rate 4°C/min) 5 min at 120°C (rate 4°C/min) relaxation 30 min on a hotplate	5 min, mr-Dev 600 1 min, IPA rinse with DI water
EpoClad 50 on FR-4	500 rpm for 15 s 1700 rpm for 60 s	8 min at 50°C 22 min at 120°C relaxation 40 min on a hotplate	Flood exposure: 90 s performed in two steps with 3 min pause between	3 min at 50°C (rate 4°C/min) 6.5 min at 120°C (rate 4°C/min) relaxation 40 min on a hotplate	7 min, mr-Dev 600 2 min, IPA rinse with DI water
EpoClad 50 with a copper layer (e.g. meander)	500 rpm for 15 s 1700 rpm for 60 s	10 min at 50°C 22 min at 120°C relaxation 40 min on a hotplate	Flood exposure: 90 s performed in two steps with 3 min pause between	10 min at 50°C (rate 2°C/min) 3 min at 120°C (rate 2°C/min) relaxation 40 min on a hotplate	7 min, mr-Dev 600 2 min, IPA rinse with DI water
EpoClad 100	500 rpm for 15 s 900 rpm for 60 s	25 min at 50°C 70 min at 120°C relaxation 60 min on a hotplate	Flood exposure: 150 s performed in two steps with 3 min pause between	2 min at 50°C (rate 4°C/min) 16 min at 120°C (rate 2°C/min) relaxation 60 min on a hotplate	10 min, mr-Dev 600 2 min, IPA rinse with DI water
EpoCore 3*	500 rpm for 15 s 3300 rpm for 40 s	3 min at 65°C 7 min at 95°C relaxation 30 min on a hotplate	LDW with a Gaussian beam: laser spot $\varnothing 8 \mu\text{m}$, $P = 0.75 \text{ mW}$, $v_l = 6 \text{ mm/s}$	4 min at 50°C (rate 4°C/min) 9 min at 85°C (rate 4°C/min) relaxation 30 min on a hotplate	4 min, mr-Dev 600 1 min, IPA rinse with DI water
EpoCore 5*	500 rpm for 15 s 2800 rpm for 40 s	7 min at 50°C 12 min at 90°C relaxation 40 min on a hotplate	LDW with a Gaussian beam: laser spot $\varnothing 33 \mu\text{m}$, $P = 2.2 \text{ mW}$, $v_l = 2.5 \text{ mm/s}$ LDW with an aperture: laser spot $\varnothing 250 \mu\text{m}$, $P = 220 \mu\text{W}$, $v_l = 40 \mu\text{m/s}$, $v_{ef} = 10 \mu\text{m/s}$	10 min at 50°C (rate 4°C/min) 20 min at 85°C (rate 4°C/min) relaxation 40 min on a hotplate	7 min, mr-Dev 600 2 min, IPA rinse with DI water

3.5 Post-Processing

In order to prepare an optofluidic platform with integrated waveguides for optical and fluidic coupling several post-processing steps, such as grinding and polishing of the waveguide end-faces, sealing of the fabricated fluidic channels and connections of fluidic tubes, should be performed. These steps are described in detail in the following sections.

3.5.1 Polishing of the End-Faces

The light coupling efficiency of an optical fiber and a waveguide correlates with their end-face surface roughness [128, 129]. For a conventional optical glass fiber, the end-face is created by a fiber cleaver, which deliberately breaks the fiber and thus forms a smooth fiber surface perpendicular to the fiber's axis. To minimize the coupling losses, the waveguide end-face should also have a high optical surface quality. Therefore, a polishing process of the waveguide's end-face is essential [130].

The end-face finishing is performed on a rotating turntable with attached abrasive paper or polishing cloth (see Fig. 3.17). During the grinding and polishing processes, the grinding rate and the surface quality are defined by time t , applied pressure p , rotation speed n , substrate orthogonality, and grain size of the abrasive paper [131].

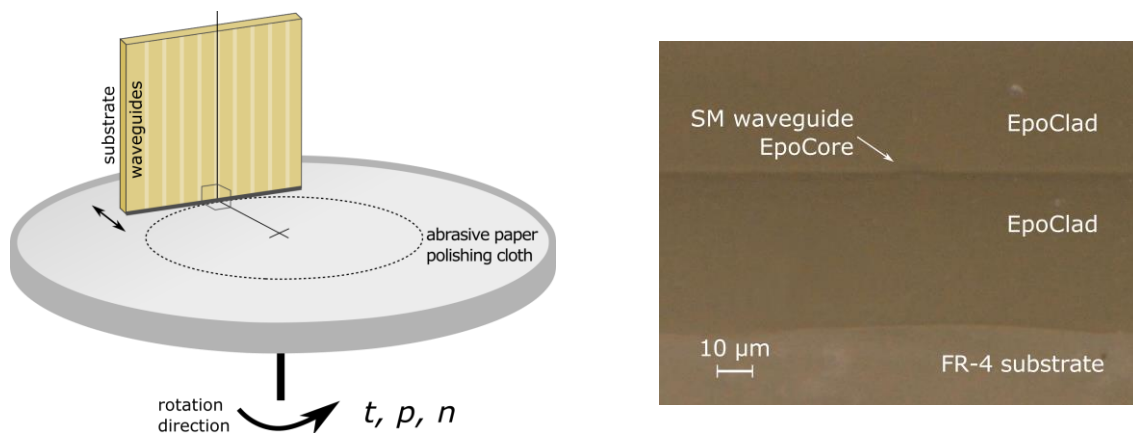


Fig. 3.17: (Left) The polishing of the waveguide end-faces: the board is placed perpendicularly to the rotating grinding wheel; grain size, rotation speed n , time t are controlled and pressure p is applied manually; (right) polishing result of a single-mode waveguide end-face with optical surface quality $Ra = 45 \pm 4.1$ nm.

The grinding is performed on a preparation system TegraPol-15 (Struers GmbH) consisting of four steps. The vertically held substrate is grinded subsequently with abrasive papers P600, P1200, P2500, and P4000. Water serves as a lubricant to avoid unwanted polymer heating during grinding and polishing and to rinse the grinded polymer residues from the working surface. Between each grinding and polishing step, a specimen should be rinsed thoroughly with water in order to avoid contamination with abrasive and polymer residues and thus to achieve a better polishing result. In case of waveguides on FR-4 substrate, the optimal processing conditions for each step are listed in Table 3.4. The pressure is currently being applied manually.

Good adhesion of processed photopolymer layers to each other and to the substrate is mandatory for prevention of structures delamination and stripping during abrasive grinding or polishing at high

rotation speed [132]. Fig. 3.18 demonstrates the digital microscope pictures of this defects on FR-4 (left) and glass (right) substrates.

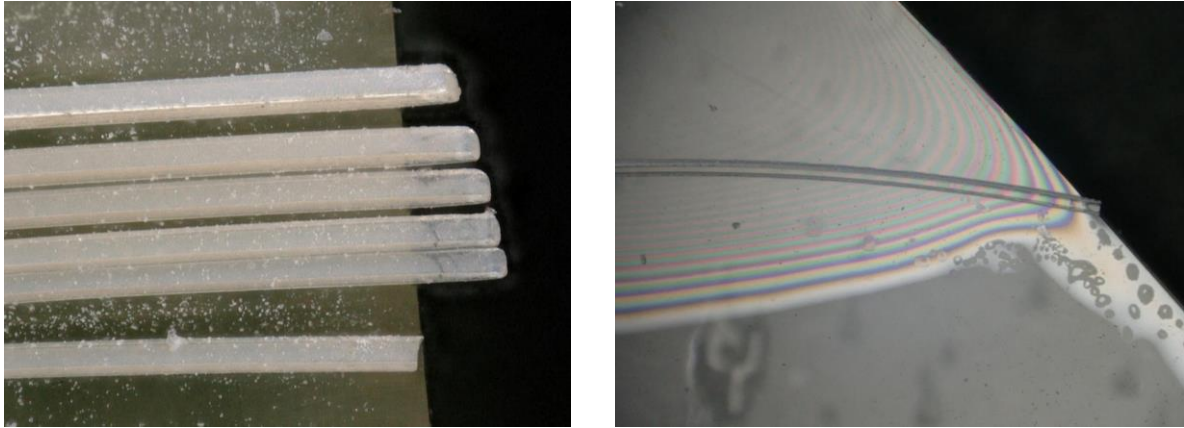


Fig. 3.18: (Left) Stripping of polymer structures due to insufficient adhesion of waveguide cores to lower cladding layer; (right) Delamination of lower cladding layer during grinding process due to insufficient polymer to substrate adhesion.

The final polishing sequence is performed in three steps using a polishing film set designed for glass fiber polishing (Polish Film from Fiber Instruments Sales Inc.). The films with grit size of $5\ \mu\text{m}$ (SiC) / $1\ \mu\text{m}$ (SiC) / $0.03\ \mu\text{m}$ (Al_2O_3) are used subsequently without any lubricants. The substrate is manually moved over the film following the trajectory imitating number "8". The substrate end-face is then rinsed with water, dried with fiber optic wipes and qualitatively inspected under the optical microscope after each step. If necessary, the step is repeated. Finally, the surface roughness is assessed by a laser scanning microscope (Keyence VK-X200). The repeatedly achieved surface quality has the arithmetical mean roughness of $R_a \approx 45\ \text{nm}$ and the mean roughness depth of $R_z \approx 172\ \text{nm}$.

Table 3.4: Grinding and polishing process parameters for finishing the waveguide's end-faces on FR-4 substrate.

Abrasive paper type	Grain size	Rotation speed / time	Lubricant, comments
Grinding / P600 (SiC)	$26\ \mu\text{m}$	300 rpm / to the desired position	water, rinse with water
Grinding / P1200 (SiC)	$15\ \mu\text{m}$	250 rpm / 5 min	water, rinse with water
Grinding / P2500 (SiC)	$8\ \mu\text{m}$	200 rpm / 5 min	water, rinse with water
Grinding / P4000 (SiC)	$5\ \mu\text{m}$	200 rpm / 5 min	water, rinse with water
Polishing / glass fiber polish film (SiC), purple	$5\ \mu\text{m}$	move the substrate imitating the number "8" / 5 min	no lubricant, rinse with water, dry with a wipe
Polishing / glass fiber polish film (SiC), gray	$1\ \mu\text{m}$	move the substrate imitating the number "8" / 5 min	no lubricant, rinse with water, dry with a wipe
Polishing / glass fiber polish film (Al_2O_3), white	$0.03\ \mu\text{m}$	move the substrate imitating the number "8" / 5 min	no lubricant, rinse with water, dry with a wipe

The end-face of a waveguide can be also prepared for further optical coupling by milling or cutting with a diamond dicing saw [129]. Milling allows local and inboard treatment. In this project, the experiments of inboard local polishing of waveguide end-faces are not performed.

3.5.2 Board Level Integration: Light Coupling Concepts

Board level light coupling remains one of the major difficulties in fabrication of EOCB and optofluidic devices. In the literature, a variety of concepts of active and passive optical coupling implementations are reported [83, 133–135].

Several approaches of optical coupling are evaluated in this project. For the aligned coupling of optical waveguides on EOCB to surface mounted LEDs, an aperture in a pre-aligned thin metal plate is used. This concept is described in detail in section 5.1.2. Fig. 3.19 (left) demonstrates irreversible gluing of buried glass fibers. Here, a trench is structured by means of mask-based lithography in the lower and in the upper cladding layers; a conventional glass fiber is positioned in this trench, adjusted to a buried polymer waveguide and then fixed by UV-curable NOA 81 (Norland Products Inc.) optical adhesive (curing settings 50 s, 4.7 mW/cm²). This temporary solution is bulky and inflexible but it enables stable light coupling and is found to be suitable for laboratory testing.

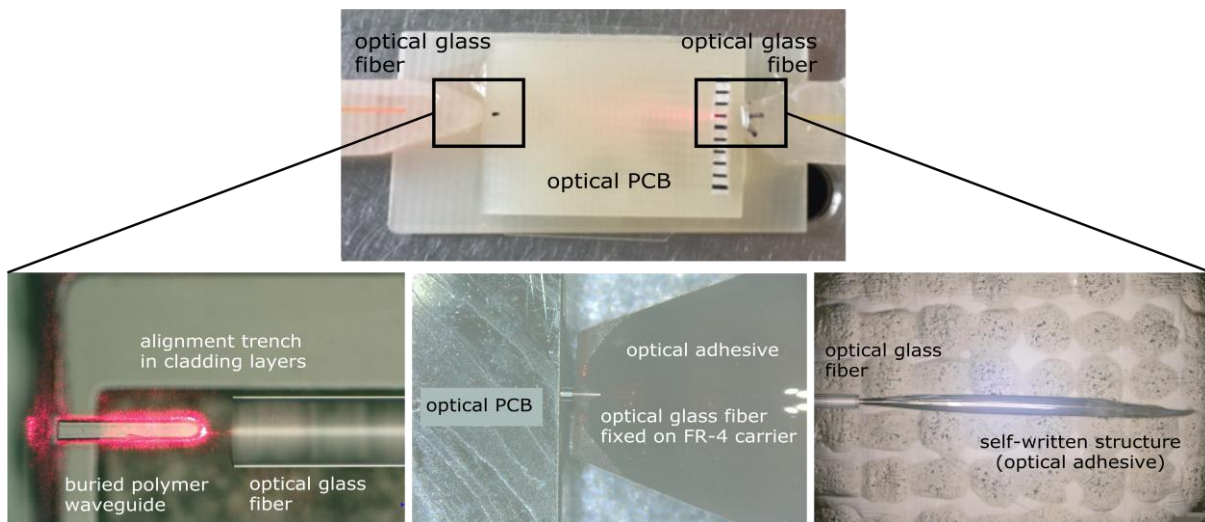


Fig. 3.19: Board level substrate to glass fiber irreversible coupling concepts using an optical adhesive: (left) glass fiber to buried waveguide alignment in a trench in lower and upper cladding layers; (center) butt-coupling with an optical fiber pre-fixed on a FR-4 carrier; (right) self-written structure out of photosensitive polymer (SU-8).

The irreversible butt-coupling can be implemented using an additional FR-4 carrier (Fig. 3.19, center). The glass fiber is fixed on the carrier by NOA 81. Then this carrier is fixed on a 3-axis flexure stage (MicroBlock™ MBT616D/M, Thorlabs, Inc.) in order to adjust the fiber tip position with respect to the polished waveguide end-face. After the optimal position is found, both ends are glued together by optical adhesive.

Self-written waveguides are another interesting option [136, 137]. The optical glass fiber tip and the waveguide end-face positions are aligned with a small gap in between. The gap is filled with an optical adhesive. The optical fiber is connected to the Omicron LuxX 375-20 UV diode laser. Activating the laser for 60 s at a power of 2.1 mW cross-links the optical adhesive directly in front of the fiber end-face. Then the flood exposure with UV-light (50 s, 4.7 mW/cm²) fixes the fiber tip to

the waveguide end-face. Fig. 3.19 (right) demonstrates the self-written structure made of SU-8 photosensitive resist in front of a glass fiber tip on FR-4 substrate surface.

In this project, both reversible and irreversible butt-coupling of conventional glass fibers are used as standard light coupling approaches for optical waveguide testing and for EOCB-demonstrator evaluation. In case of reversible butt-coupling, the index matching gel is applied between the waveguide and glass fiber end-faces for compensation of the surface roughness and for gradual refractive index adjustment [56].

A thorough analysis of the aforementioned approaches in terms of coupling losses and mechanical and environmental reliability is not performed within this work. Optical coupling is an important and extensively broad topic. However, it is beyond the scope of this project and hence should be investigated independently in future work. An overview of existing coupling methods is presented in the outlook section of this thesis (see chapter 6.2.2).

3.5.3 Optofluidic Device Packaging – Fluidic Connection

The sealing of microfluidic channels could be achieved by attaching a cover layer and applying pressure or different bonding techniques, such as adhesion, lamination, thermal [138] and chemical bonding [50]. The dry resist has the possibility to bridge over gaps (overhangs up to 10 mm can be easily laminated) and can be applied for sealing of microfluidic channels. This technique overcomes the limitations associated with full-wafer bonding and enables fast and cost-effective sealing with higher yield.

In this project, the sealing of fluidic channels is performed by lamination of 62.5 μm thick solder mask (Dynamask KM, Morton) [139]. It is a dry film negative tone photoresist and can be patterned photolithographically. The laminated layer is applied in a fast and easy way but is not very durable and firm as compared to glued or bonded thin glass plate. The maximal pressure the structure can withstand should be determined in future work.

RLM 419P laminator (Walter Lemmen GmbH) is used in this work for sealing of microchannels. The adjustable process parameters are the laminator roll's temperature, the roll velocity v and the roll pressure p on the board. The resist temperature T_{resist} and its viscosity should be optimized to achieve good adhesion to substrate surface without leakage and microchannels obstruction. The following settings provide reliable sealing: $T_{\text{resist}} = 35\text{ }^\circ\text{C}$, $v = 2\text{ m/s}$, $p = 0\text{ bar}$ (see Fig. 3.20 (left)). After lamination, the board is kept in a dark and cool place for approximately 8 h. The flood exposure is done by exposure unit rapid 3000 (Welisch Elektronik GmbH) for 1 min at 4.7 mW/cm². The development of the exposed solder mask layer is performed in sodium carbonate (Na₂CO₃) for 5 min at a temperature of 30 $^\circ\text{C}$ followed by subsequent rinsing with deionized water. According to the datasheet from [139], the chemical resistivity of the solder mask can be improved by further tempering step performed in the EED-53 oven from WTB binder GmbH at $T = 150\text{ }^\circ\text{C}$ for 60 min.

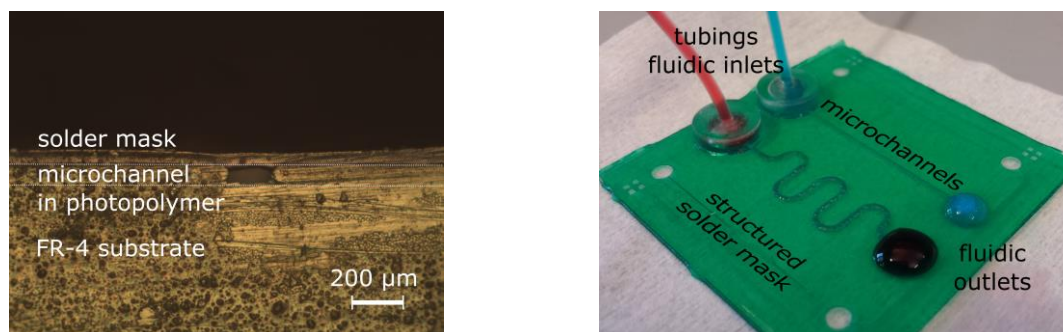


Fig. 3.20: (Left) A microscopic picture of a 200 μm wide microchannel sealed with a solder mask; (right) an optofluidic platform on a glass substrate with 200 μm wide microchannels sealed with solder mask and glued connector and tubings.

Inlet and outlet holes are photolithographically structured in the sealing layer. Custom-made PMMA tubing holders are placed above the in/outlet and glued to the solder mask surface using an UV-curable adhesive Proformic Pen Midget (VIKO UG). The tubings are then inserted into openings and the fluidic device is sealed hermetically. This can now be connected to an external fluidic system, e.g. to a syringe pump. Fig. 3.20 (right) demonstrates the sealed microchannels on a glass substrate.

4 Characterization of Optical Waveguide Components

In chapter 3, the fabrication process of polymer-based waveguides and fluidic platform is described. It included a combination of laser direct writing and mask-based lithography. Epoxy resin based photopolymers, such as SU-8 / EpoCore, EpoClad, are used to fabricate the waveguides and fluidic platform. Along with technology improvement, it is important to characterize the fabricated microstructures. In this chapter, the influence of technological process parameters on the structured optical waveguides, such as end-face geometries, sidewall roughness, spectral light transmittance, and optical losses, is studied. The guiding and focusing properties of waveguides with curved and flat end-faces are characterized and compared.

4.1 Optical Characterization of Polymer Waveguides^a

The optical losses in a waveguide linked to an optical system can be divided into length-dependent propagation losses, coupling losses, and geometry-induced bending losses. In order to achieve better sensor sensitivity and performance, the dominant optical losses in guiding structures should be determined. They can be mitigated by layout optimization, e.g. by implementation of larger radii of curvature, change of refractive index contrast, for instance, air-exposed waveguides [70, 72], or by length reduction of light guiding paths.

This section details the optical characterization in terms of optical losses and spectral transmission of multi-mode waveguides with typical cross-sectional dimensions of $50 \times 50 \mu\text{m}^2$. The waveguides are made of EpoCore/EpoClad material combination on FR-4 substrates.

4.1.1 Propagation and Coupling Losses Analysis

The absorption in material (absorption losses), scattering at waveguides sidewalls (scattering losses) and mode mismatch cause the length-dependent optical propagation losses V_{pL} , expressed in [dB/cm]. They can be determined by a destructive cutback technique. In this method, a straight waveguide is cut-off centimeter-by-centimeter and polished. The insertion loss V_{iL} expressed in [dB] is a combination of all the losses that occur in the waveguide when coupled in an optical link, i.e. coupling and propagation losses. It is measured for different waveguide lengths. In case the launch and end-face conditions (the surface quality and measuring environment) are consistent and assuming that coupling losses are constant for each measurement, the propagation loss can be estimated as a coefficient of linear regression model that fits the measured insertion loss data [141].

In Fig. 4.1, a schematic of the laboratory setup for propagation loss measurements is shown. The optical power measurements are performed at a wavelength of $\lambda = 850 \text{ nm}$ using a fiber-coupled laser diode FOSS-21-3S-5/125-850-S-1 (OZ Optics Ltd.) as a light source and power meter ML93B with

^a The experiments to determine propagation losses, spectral transmission are performed by Dr. rer. nat. Haldor Hartwig and to determine bending losses by B.Sc. Henning Bathel in frame of his Bachelor thesis [140].

measuring head MA95A (Anritsu Corp.) as a detector unit. The optical coupling is performed using two 3-axis flexure stages MicroBlock™ MBT616D/M (Thorlabs, Inc.) with a tilt module by butt-coupling of single-mode glass fiber SMF-28 with core diameter $8.2\ \mu\text{m}$ at the input side and M43L05 multi-mode glass fiber with core diameter $105\ \mu\text{m}$ at the output side. In order to achieve better numerical aperture fit of the launch fibers and the waveguide core under test, and to reduce Fresnel reflections on refractive index discontinuities, an index matching gel is applied [56]. A Dino-Lite Premier microscope is used to control horizontal fiber-to-waveguide end-face relative position.

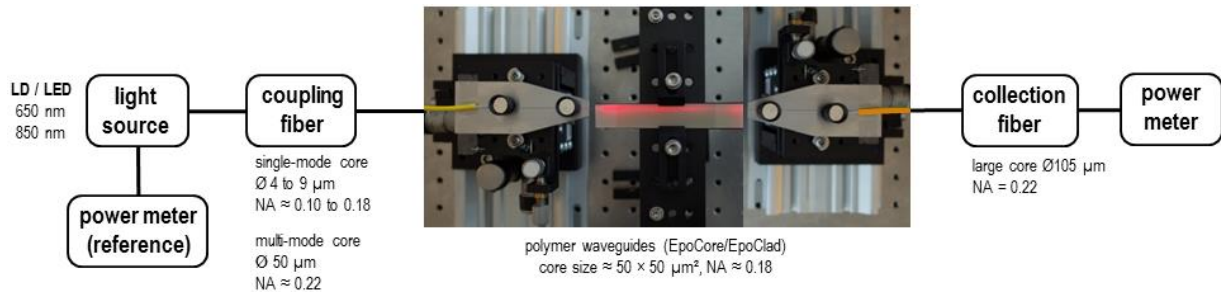


Fig. 4.1: Insertion loss measurement setup consisting of external light source, photodiode, launch glass fibers, digital microscope for monitoring of fiber-to-waveguide position and two 3-axis flexure stages.

The insertion losses of straight $50 \times 50\ \mu\text{m}^2$ waveguides made of EpoCore (core) and EpoClad (cladding) are evaluated according to the procedure described above. The insertion losses are measured for ten straight waveguides at three different lengths, whereas the coupling losses are assumed constant. The intersection of the linear fit and the vertical axis defines the constant coupling loss and the slope of the linear fit specifies the propagation loss coefficient of this waveguide configuration. Fig. 4.2 (left) exemplifies the results of two measurements.

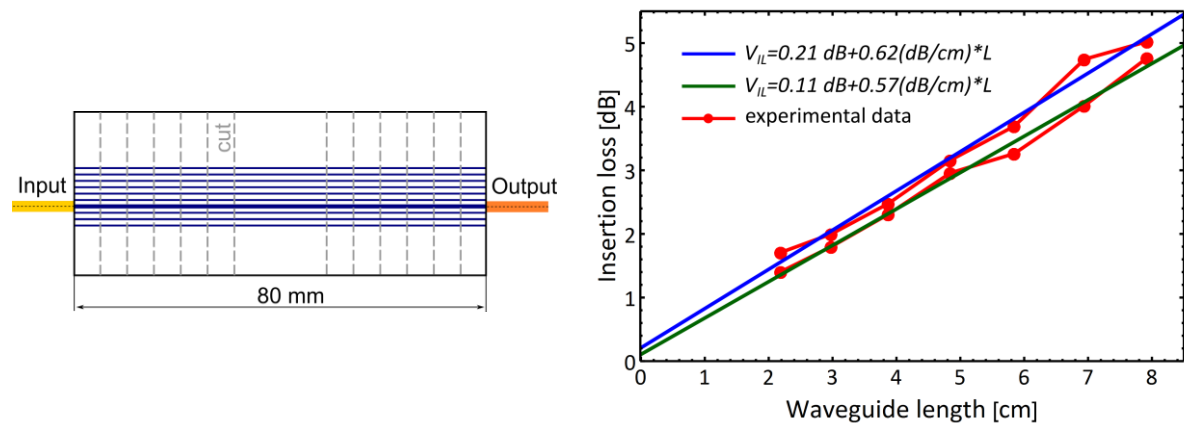


Fig. 4.2: (Left) Layout of EOCB for determination of insertion losses, which are a combination of propagation and coupling losses, in ten straight multi-mode EpoCore waveguides with cross-sectional dimension of $50 \times 50\ \mu\text{m}^2$; (right) results of experimental determination of insertion losses V_{IL} exemplified by two measurements.

In $50 \times 50\ \mu\text{m}^2$ multi-mode EpoCore waveguide cores, the average propagation loss for $\lambda = 850\ \text{nm}$ is estimated to be $V_{PL} = 0.59 \pm 0.05\ \text{dB/cm}$. The measured average coupling loss is $V_{CL} = 0.17\ \text{dB}$. Since the coupling loss depends on the quality of the end-faces polishing, NA , and dimensional match between waveguide and launch fiber, this value will be used for further calculations while keeping these parameters constant.

This experimentally obtained propagation loss is slightly higher than the value of 0.2 dB/cm specified for EpoCore at $\lambda = 850$ nm by photoresist manufacturer (Microresist Technology GmbH) [53]. This discrepancy is because, in this work, the propagation losses are measured in rectangular laser-written waveguides, while the value given by manufacturer is for unstructured planar waveguides. The laser-written waveguides exhibit an additional optical loss due to the scattering at the waveguide sidewalls. However, the obtained result is in line with propagation losses of 0.53 dB/cm reported by other research groups for EpoCore/EpoClad multi-mode waveguides structured mask-based [97].

4.1.2 Spectral Light Absorption in Epoxy-based Polymer Waveguides

Many optical sensing approaches, for instance, spectroscopic fluid analysis, require a good transmission over a wide range of wavelengths, e.g. for dissolved organic matter, especially, in ultraviolet (UV) and visible (Vis) light spectrum. Therefore, the optical light transmission of photoresists used for fabrication of waveguide's cores should be investigated.

According to the datasheets of SU-8 and EpoCore [85, 102], these photoresists should be highly transparent in the Vis to near-infrared (NIR) spectrum. The optical properties of these photopolymers are given as transmittance (%) Fig. 4.3 (left). Therefore, the determination of optical loss from this graph is difficult due to its linear representation. The absorbance curves are requested from Microresist Technology GmbH (see Appendix) and converted into transmission losses expressed in dB/cm by neglecting the reflection losses:

$$T = \frac{10}{d} \log_{10}(1 - A), \text{ where } T + A \approx 1, \quad (4.1)$$

where T is transmittance, A is absorbance, and d is the thickness of the polymer layer. Fig. 4.3 shows the transmittance [%] reported in datasheet and transmission losses [dB/cm], converted from absorption data provided by Microresist Technology GmbH for a 665 μm thick unexposed/exposed EpoCore layer.

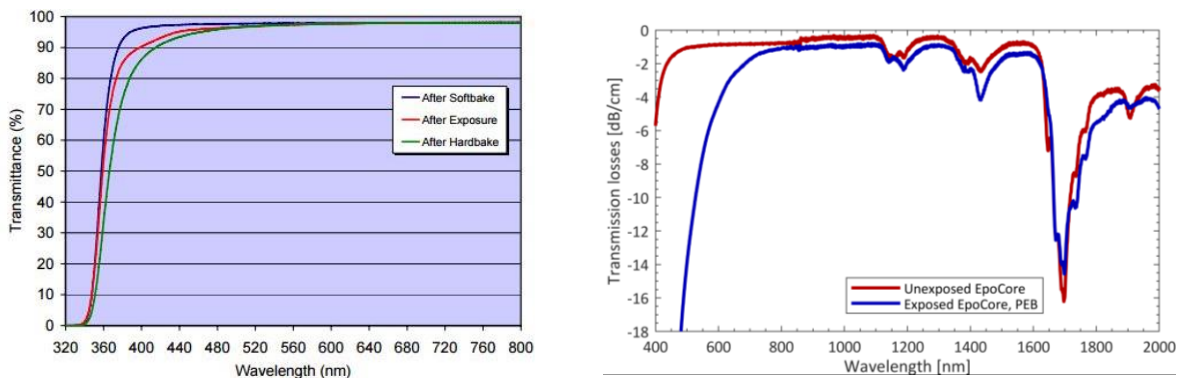


Fig. 4.3: (Left) Optical transmittance of SU-8 2000, datasheet [102]; (right) transmission losses in dB/cm calculated from the absorption curves received from Microresist Technology GmbH for a 665 μm thick EpoCore layer.

The preliminary light transmission measurements for fabricated $50 \times 50 \mu\text{m}^2$ waveguides made of SU-8 and EpoCore in our laboratory show low transmittance in yellow and green light ranges. Several factors, such as the process parameters, sidewall roughness, and intrinsic absorption in the polymer,

have a major influence on optical losses. Sufficient light transmittance in Vis - NIR light range is important for optical fluid sensing and needs to be investigated thoroughly.

To prevent the formation of refractive index inhomogeneity within the core of epoxy-resin waveguides, i.e. "double core" effect discussed in section 3.4.3, the modified PEB process at higher temperatures and longer ramps is introduced in the technological process chain. It is known from other research studies that the light transmission degrades with higher exposure dose and longer PEB process at higher temperatures [94].

The light scattering on the sidewalls of optical structures is another loss source. The EpoCore waveguides fabricated on FR-4 substrates reveal a sidewall roughness of $R_a = 226 \pm 25$ nm (see section 4.2 for roughness analysis). If the size of the sidewall's inhomogeneities falls into the same order of magnitude as the wavelength of the guided light, the scattering at the sidewall's inhomogeneities could be partly described by Mie-scattering, which is a scattering on particles with diameters approximately equal to the wavelength of the incident radiation. Therefore, it can be assumed that the propagation of light with longer wavelengths is less influenced by sidewall roughness resulting in lower propagation losses.

To evaluate the dependence of transmission in epoxy-based polymers on process parameters, sidewall roughness, and material itself, a series of experiments on four substrates, specified in Table 4.1, with polymer combination of EpoClad as lower- and upper-cladding and SU-8 or EpoCore as core materials, are performed. In these experiments, the PEB parameters are varying while the pre-process parameters, such as softbake, exposure dose, UV laser beam profile (Gaussian beam), and spot size, are kept constant.

Table 4.1: Specification of substrates and process parameters for evaluation of optical transmittance of epoxy-based rectangular and planar waveguides.

Nr.	Waveguide type	Core dimensions height/ width	Core Material	Exposure	Post Exposure Bake (PEB)	Goal of the experiment
1	rectangular	50 μ m / 50 μ m	EpoCore	laser direct writing	standard (data sheet): 5 min at 50°C, 12 min at 85°C	influence of process parameters (PEB) and material EpoCore vs. SU-8
2	rectangular	50 μ m / 50 μ m	EpoCore	laser direct writing	increased time: 10 min at 50°C, 20 min at 85°C	influence of process parameters (PEB) and material EpoCore vs. SU-8
3	rectangular	50 μ m / 50 μ m	SU-8	laser direct writing	increased temperature: 5 min at 65°C, 12 min at 95°C	influence of process parameters (PEB) and material SU-8 vs. EpoCore
4	planar	50 μ m / infinite	SU-8	flood exposure unstructured	standard (data sheet): 1 min at 65°C, 5 min at 95°C	influence of sidewall roughness

Transmission measurements are performed by means of the setup used for determination of propagation losses, see Fig. 4.1. Light coupling is performed by butt-coupling of a single-mode glass fiber ($\emptyset 9$ μ m core) at the input side and multi-mode FT300 fiber ($\emptyset 300$ μ m core) at the output. The light sources are a broadband tungsten lamp SLS201L with spectral range of 360 – 2600 nm (Thorlabs, Inc.) and LEDs with wavelengths 500, 590, 625, and 850 nm. A spectrometer USB2000 (Ocean Optics Corp.) and a power meter ML93B with measuring head MA95A (Anritsu Corp.) serve as detector units

for the measurements with tungsten lamp and LEDs, correspondingly. The power detects records the output power in dBm^a and the spectrometer records spectral signal in *counts* (value range 0 – 4000). A spectrum of the tungsten lamp (at fixed exposure time) or actual output power of the LEDs in dBm are recorded as a reference for calculation of optical losses in dB or dB/cm. To prevent the fluctuations of output spectral characteristics, the LEDs are operated under current with a constant value.

The input and output spectra of spectrometer can be compared, knowing that the signal from the spectrometer (*counts*) is proportional to power and exposure time. Thus, the calculation of the optical transmission loss V_{TL} is performed as follows:

$$V_{TL} = 10 \log_{10} \left(\frac{\text{counts}_{in}}{\text{counts}_{out}} \right) \quad (4.2)$$

The experimental results for substrates 1-4 are shown in Fig. 4.4. The generally observed trend for all epoxy-based waveguides is that a significantly higher optical loss occurs for wavelengths $\lambda < 600$ nm, i.e. the propagation losses for orange light ($\lambda = 590$ nm) are higher than for red ($\lambda = 625$ nm) and infrared ($\lambda = 850$ nm) light, see Fig. 4.4 (left).

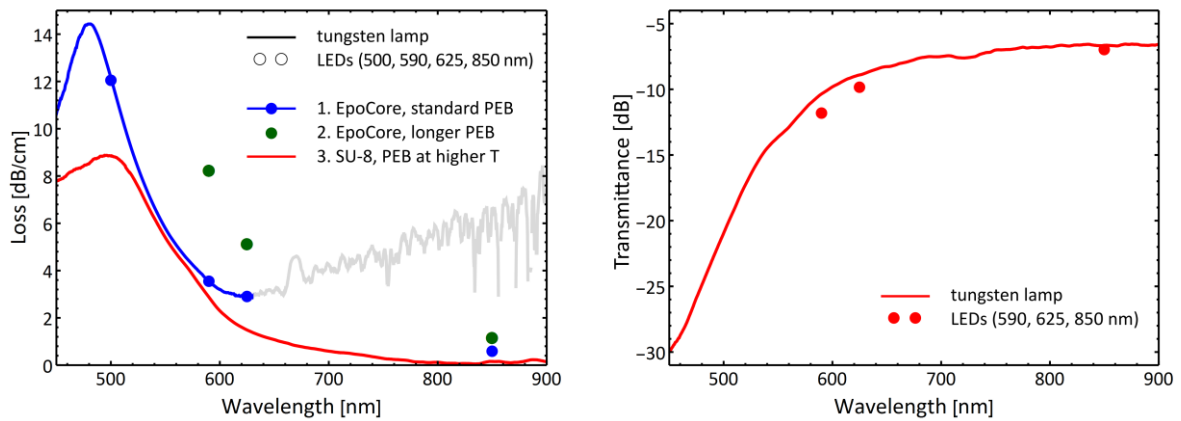


Fig. 4.4: (Left) Propagation losses measured in polymer waveguides using tungsten lamp (continuous lines) and LEDs with wavelength of 500, 590, 625, 850 nm (points): EpoCore $50 \times 50 \mu\text{m}^2$ waveguide with PEB according to datasheet, substrate 1 (blue), the noisy region is given in gray; EpoCore $50 \times 50 \mu\text{m}^2$ waveguide with longer PEB, substrate 2 (green); SU-8 $50 \times 50 \mu\text{m}^2$ waveguide with PEB at higher temperature, substrate 3 (red). (Right) Optical transmittance in exposed SU-8 planar waveguide, substrate 4.

In SU-8 and EpoCore photopolymers, different solvents are used to keep them liquid at room temperature, while the epoxy-based components have the same chemical composition. Thus, if both materials are processed identically, the optical losses should be comparable. However, SU-8 waveguides (substrate 3) show smaller propagation losses than EpoCore (substrate 1) having propagation losses of approximately 2.74 dB/cm at $\lambda = 590$ nm, 1.57 dB/cm at $\lambda = 625$ nm, and 0.30 dB/cm at $\lambda = 850$ nm, see Fig. 4.4 (left, red versus blue).

Furthermore, a strong influence of the PEB process parameters on transmission is observed. The light transmission in EpoCore is degraded by longer PEB process with a difference in propagation losses of

^a Decibel Milliwatt (dBm) is the power level in decibels referred to 1mW, i.e. $P [\text{dBm}] = 10 \log_{10} \frac{P[\text{mW}]}{1 \text{ mW}}$

approximately 4.70 dB/cm at $\lambda = 590$ nm, 2.20 dB/cm at $\lambda = 625$ nm and 0.59 dB/cm at $\lambda = 850$ nm comparing to waveguides with PEB performed according to datasheet (Fig. 4.4 (left) substrate 1 versus 2).

The influence of sidewall roughness is evaluated on a planar SU-8 waveguide (substrate 4), i.e. exposed unstructured 50 μm thick SU-8 layer. The measured losses can be interpreted as the sum of wavelength-dependent material loss and (nearly) wavelength-independent geometrical loss due to permitted light divergence. The results are given in Fig. 4.4 (right) and confirm a significant deterioration in transmittance and strong internal absorption for wavelengths $\lambda < 600$ nm.

During the fabrication process, it is important to compare the obtained optical losses with values reported by a manufacturer for evaluation of process parameters and quality of fabricated optical structures. The propagation losses experimentally determined at IGS^a for multi-mode waveguides accompanied by sidewall roughness-induced scattering losses are comparable to the values derived from transmittance data for unstructured EpoCore layer provided by Microresist Technology GmbH (see Table 4.2). Therefore, it can be concluded that optical losses in fabricated polymer waveguides are predominantly caused by internal absorption in the polymer itself and the sidewall roughness has less impact on transmission of Vis light. No significant improvement of EpoCore transmittance in the UV-Vis spectral range can thus be achieved by optimization of exposure, softbake and development parameters. Longer PEB process performed at higher temperatures leads to significant deterioration in transmittance but is essential for elimination of inhomogeneities within the core ("double core" effect).

Table 4.2: Sampling from the converted transmittance data (Fig. 4.3, left) and measured propagation losses (substrates 1, 2) in EpoCore for the most critical wavelengths.

Wavelength	Microresist Technology GmbH exposed planar waveguide PEB according to datasheet	IGS, University of Rostock 50 × 50 μm^2 waveguide PEB according to datasheet	IGS, University of Rostock 50 × 50 μm^2 waveguide longer PEB
500 nm	13.90 dB/cm	12.05 dB/cm	-
590 nm	4.80 dB/cm	3.55 dB/cm	8.25 dB/cm
625 nm	2.67 dB/cm	2.90 dB/cm	5.15 dB/cm
850 nm	1.07 dB/cm	0.59 dB/cm	1.18 dB/cm

Due to the insufficient polymer transmittance in UV and Vis light ranges, the use of these photoresists is limited for applications in environmental analysis such as detection of dissolved organic matter, Vis-spectroscopy, and fluorescence. This issue of epoxy-based resins makes sensing applications possible only in NIR range. Another issue can be the transmission degradation over time, strongly pronounced in SU-8, while EpoCore/EpoClad material combination appears to be more stable [133, 142].

4.1.3 Geometry-Induced Losses: Propagation in 90° Waveguide Bends

For downscaling of the footprint and maximizing optical interconnect density, the integrated waveguides on EOCBs are often bent. This leads to additional bend-induced optical losses in bent

^a IGS stands for Institute of Electronic Appliances and Circuits (germ. Institut für Gerätesysteme und Schaltungstechnik)

waveguide regions. The bend-induced loss mechanism is described in section 2.3. It depends on refractive index contrast of core and cladding materials, waveguide dimensions, and allowed modes [143]. This bending loss becomes significant beyond a critical radius of curvature. For determination of this critical radius, the bending losses in multi-mode waveguides with radii of curvature varying from 1 – 14 mm are evaluated. The used EOCB layout is shown in Fig. 4.5 (left). The waveguides have cross-sectional dimensions of approximately $50 \times 50 \mu\text{m}^2$. Similar to the propagation losses measurement, the measurements of bend-induced losses are performed at $\lambda = 850 \text{ nm}$ using a fiber-coupled laser diode FOSS-21-3S-5/125-850-S-1 as a light source and a power meter ML93B with measuring head MA95A as detection unit. The coupling fibers are butt-coupled to the polished end-faces of the waveguides with the use of index matching gel [56]. The experimental setup is illustrated in Fig. 4.1.

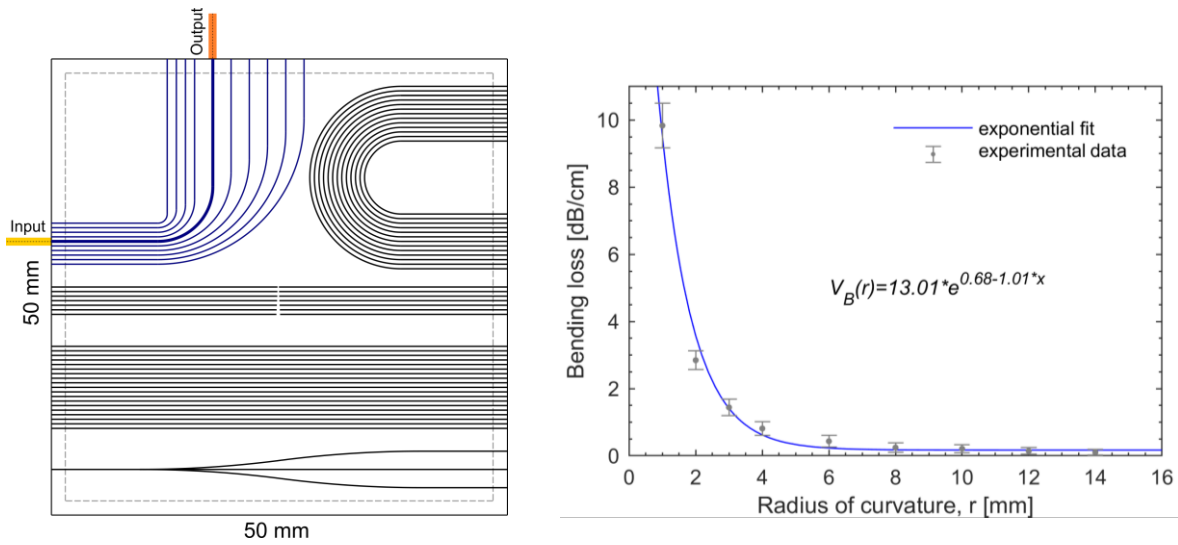


Fig. 4.5: (Left) EOCB layout for determination of propagation losses in 90° waveguide bends (marked blue) with diverse radii of curvature varying from 1 to 14 mm; (right) experimentally obtained dependence of bending losses V_B on the radius of curvature r .

In Fig. 4.5 (right) the measured bending losses V_B per centimeter length in waveguide bends depending on their radius of curvature r are shown. The coupling and propagation losses have already been subtracted from the measured values. For these calculations, the coupling and length-dependent propagation losses are assumed to have a value estimated in section 4.1.1, namely $V_{CL} = 0.17 \text{ dB}$ and $V_{PL} = 0.59 \text{ dB/cm}$. In 90° EpoCore waveguide bends, this dependence has an exponential form [144], which is expressed as:

$$V_B(r) = 13.01 e^{0.68 - 1.01 r} \text{ [dB/cm]} \quad (4.3)$$

The bending losses become significant from the critical radius of approximately $r = 6 \text{ mm}$. These experimental observations could be used in further design improvement of splitters and bent waveguides for minimization of optical losses. In order to neglect the additional bending losses, the waveguides of the later sensor should have radii of curvature larger than 6 mm. According to the considerations presented by Bamiedakis et al. [143], the waveguide shaped as raised cosine function with gradual variation in the radius exhibits less bend-induced losses in comparison with arcs of fixed radius. Therefore, raised cosine functions with the minimal radius of curvature larger than 6 mm are

used in designing Y-splitters in EOCB-based demonstrators presented in this thesis: Fresnel-refractometer (see section 5.3) and Mach-Zehnder interferometer (see section 5.4).

4.2 Sidewall Roughness Analysis

The surface morphology of waveguides plays an important role in light propagation losses due to the attenuation induced by light scattering at waveguide's surface inhomogeneities [145]. In order to keep the propagation losses within acceptable limits, the sidewall roughness of a light guiding structure is recommended to be below a tenth of the propagating wavelength [146], e.g. for propagating light with a wavelength of 850 nm the mean roughness should be $R_a < 85$ nm. For polymer waveguides patterned by laser direct writing, the roughness of vertical sidewalls is a limiting factor because the surface quality of horizontal waveguide planes is determined by the spin-coating process resulting in extremely small roughness within sub-nanometer range. Therefore, the sidewall roughness of fabricated optical waveguides should be evaluated.

Sidewall roughness of polymer-based waveguides is highly dependent on the substrate material, fabrication technique, and process parameters. The sidewall roughness of fabricated waveguides is first investigated qualitatively by means of a scanning electron microscope (SEM) Supra 25 (Carl Zeiss AG). A quantitative statement about the roughness on this basis is however impractical.

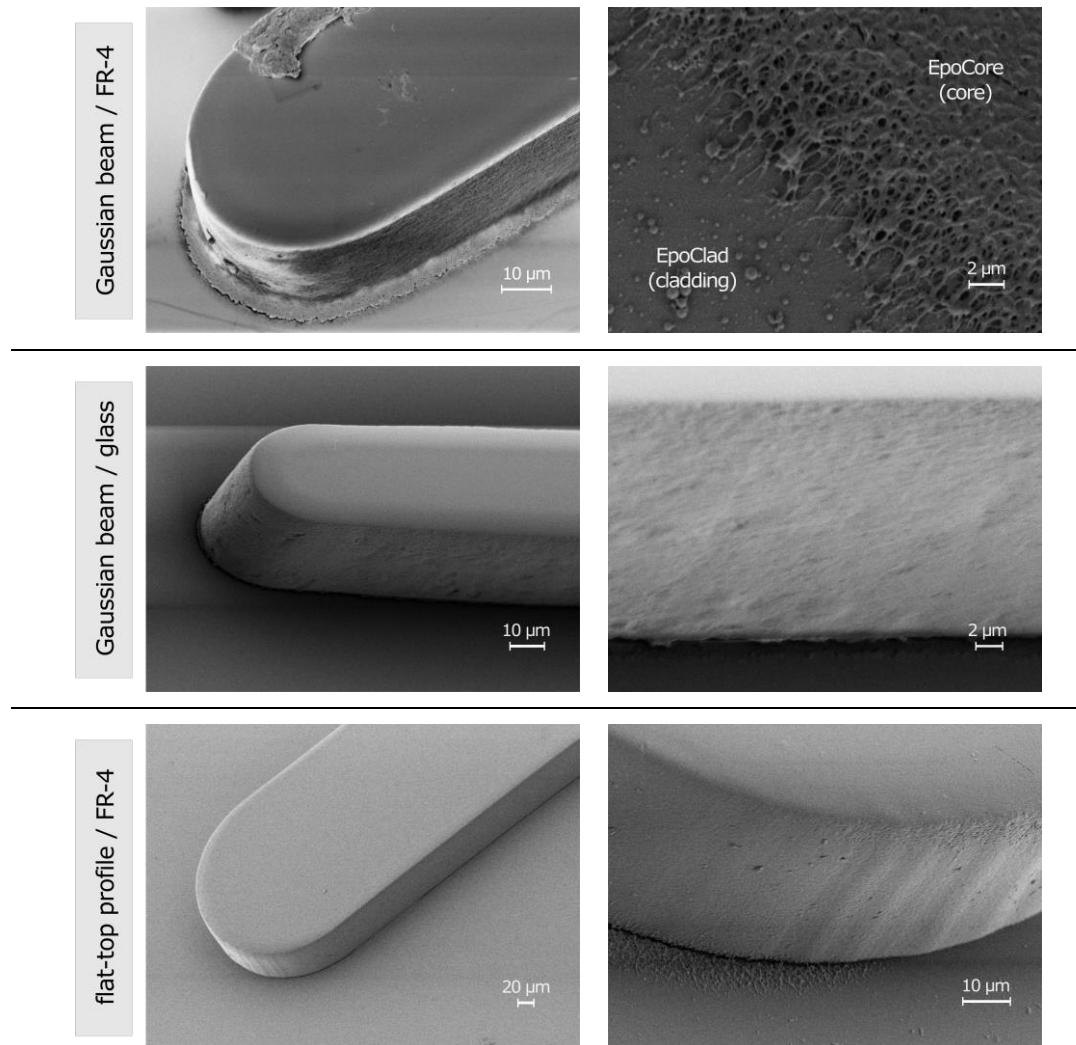
In Table 4.3, the SEM-pictures (top view and magnified sidewall's morphology) of waveguides with curved end-faces structured on different substrates are shown. The waveguides are fabricated using a Gaussian and a top-hat laser beam profiles. The images demonstrate qualitatively the substrate material and process parameter influence on the sidewall's roughness.

For investigation of substrate material influence, the waveguides fabricated with a Gaussian beam on FR-4 and borosilicate glass substrate are compared. During the exposure step by laser direct writing, the focused UV-light penetrates into photosensitive polymer layer and gets partly absorbed by it. The remaining part propagates further to the substrate surface where it gets scattered, absorbed and further transmitted. The FR-4 material is basically a glass-reinforced epoxy laminate and therefore scatters the incident light diffusely. Here, the additional uncontrollable diffuse exposure on the interface between core and lower cladding is taking place. It leads to higher scattering-induced roughness of these waveguides. In case of transparent and homogeneous poly(methyl methacrylate), PMMA (PLEXIGLAS®) and borosilicate glass substrates, the light undergoes specular reflection only at the polymer-substrate interface and inside the substrate. It does not cause additional non-periodic inhomogeneities on waveguide's sidewalls and thus steep and smooth waveguide sidewalls can be structured.

Besides the substrate material, the exposure process parameters, such as writing speed and laser intensity profile, have a huge impact on the sidewall roughness. Porous sidewalls can be observed on waveguides fabricated on FR-4 substrates with a Gaussian beam. It is assumed that the porosity originates from improper exposure parameters, namely very slow writing speed, and additional diffuse light scattering at the FR-4 surface. The waveguides written with the top-hat laser intensity profile (achieved by a circular aperture $\varnothing 200 \mu\text{m}$) show steep and smooth sidewalls even on FR-4 substrates.

No significant influence of process parameters such as PEB temperature and development time on sidewall roughness is observed.

Table 4.3: SEM pictures of curved waveguide end-faces and their sidewalls. The waveguides are fabricated using a Gaussian beam and a flat-top profile on borosilicate glass and FR-4 substrates.



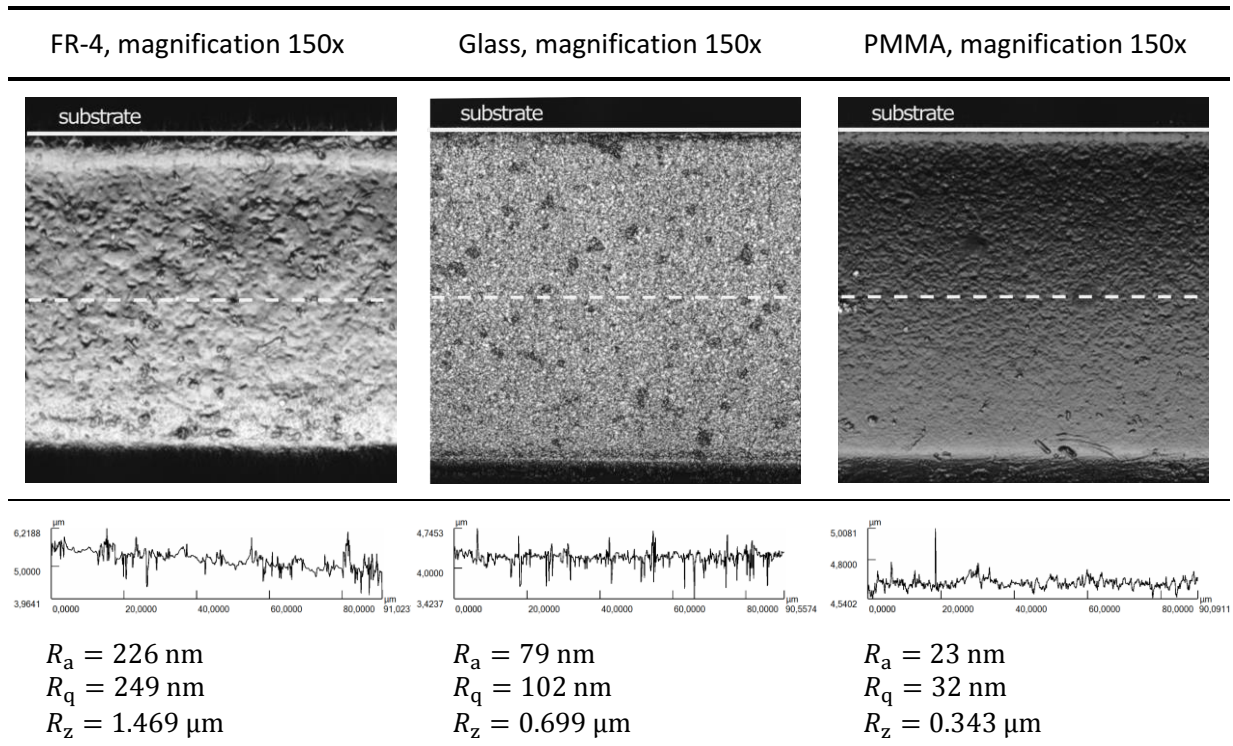
The laser scanning microscope (LSM), Keyence VK-X200^a, is involved for quantitative definition of sidewall roughness. The LSM measurement is based on confocal construction principle. The scanning of the probe in vertical direction allows the reconstruction of three-dimensional pictures by use of focused monochromatic light ($\lambda = 408 \text{ nm}$) and spatial aperture, which blocks the light reflected from out-of-focus substrate planes. During LSM analysis, the surface under test should be placed close to the objective lens: depending on the magnification factor, the gap should be multiple hundreds of micrometers. The specimen for sidewall's roughness analysis should be thus prepared in the way that the substrate material is removed by grinding until only 50 – 100 μm of material remain towards the optical waveguides. The substrate is then held upright and perpendicular to the focused laser beam.

Table 4.4 gives the LSM results of EpoCore waveguide on FR-4, borosilicate glass, and PMMA substrates. In our experiments, the roughness measurements of EpoCore waveguides fabricated on

^a LSM is a part of the laboratory equipment of the Department of Internal Combustion Engines and Piston Machines, University of Rostock

FR-4 substrate yielded the mean roughness $R_a = 226 \pm 25$ nm, the root mean square roughness $R_q = 249 \pm 31$ nm and the mean roughness depth $R_z = 1.469 \pm 0.367$ μm . Transparent glass and PMMA with non-diffuse scattering on the substrate surface provide significantly smoother sidewalls compared to FR-4 substrates: $R_a = 79 \pm 7$ nm for glass and $R_a = 39 \pm 4$ nm for PMMA. These values are in line or slightly higher than results of other research groups [48, 75] reporting the sidewall roughness of $R_a = 46 - 74$ nm of polymer-based waveguides measured using atomic force microscopy (AFM). The roughness of conventional glass fibers is significantly smaller and falls within sub-nanometer range, which results in significantly lower scattering at sidewalls and thus lowers scattering-induced losses.

Table 4.4: Laser intensities distribution and roughness profiles of the waveguide sidewalls observed using the LSM, Keyence VK-X200. All roughness values are measured on the middle of a structure (dashed line).



Glass is a chemically inert and temperature resistant material. Waveguides structured on glass substrates have smooth sidewalls. These are important features for its use in optofluidic devices. However, it is difficult to machine and, moreover, the epoxy-based resins show poor adhesion to glass substrates. Therefore, the use of glass as a substrate material is only possible to a limited extent. PMMA is chemically unstable (to alcohols such as ethanol and IPA) and thermally unstable (heat deflection temperature HDT = 103 $^{\circ}\text{C}$, glass transition temperature $T_g = 117$ $^{\circ}\text{C}$) [147]. Temperatures up to 120 $^{\circ}\text{C}$ are required for PEB of EpoClad and EpoCore. This fact makes PMMA unsuitable for its use as a substrate material. In addition to being a standard material for PCB-fabrication, FR-4 is an inexpensive, robust and easy to machine material. Polymer waveguides on FR-4 show higher surface roughness, comparing to glass and PMMA, however this substrate material represents a good compromise between polymer adhesion, chemical and thermal stability and feasibility for further post-processing steps, such as cutting and polishing of waveguide's end-faces. Based on these facts, FR-4 is chosen as the main substrate material for fabrication of polymer-based optofluidic devices in this project.

4.3 Impact of End-Face's Geometry on Light Focusing and Transmission in Discontinuous Waveguides

In case of through-beam sensors, the light source and detector are aligned directly opposite each other, by means of glass fibers, or discontinuous waveguides, as it is implemented in demonstrator for absorption-based measurements (see section 5.1). Each glass fiber or waveguide has a pre-defined field of view with an effective beam area (see Fig. 4.6). The effective beam area is a part of the cone of the light that propagates between the end-faces and can be guided by fiber or waveguide to the detector [68]. This parameter should be considered during an optical system design.

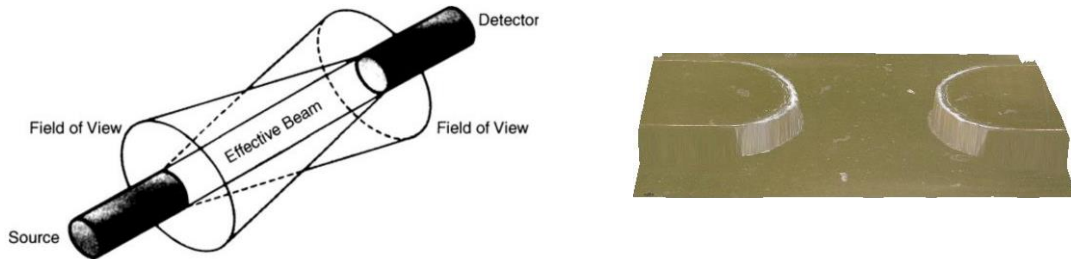


Fig. 4.6: (Left) Effective beam area of two fiber facing each other [68]; (right) 3D visualization of a discontinuous waveguide with two curved end-faces facing each other, radius of end-face curvature $r = 125 \mu\text{m}$.

The end-face geometry is an important characteristic of discontinuous waveguides. It should be considered for the improvement of light focusing, in order to increase transmitted light power in the sensing region between two waveguide end-faces. Optical waveguides with various end-faces can be fabricated by laser direct writing with an aperture masking the focused laser beam. The end-face shape and size are controlled by the programmable writing trajectory, diameter and intensity distribution of the exposure laser beam, and the aperture shape. By varying these parameters, so-called curved waveguides with rounded end-faces and flat-ended waveguides can be obtained (see Fig. 4.7).

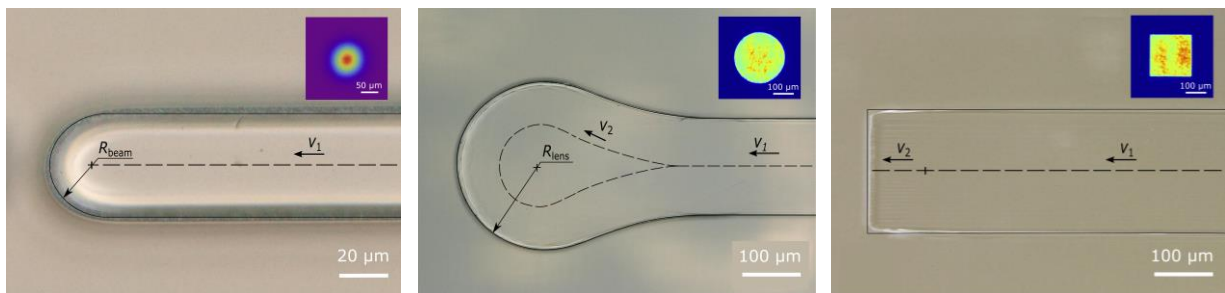


Fig. 4.7: Fabricated waveguides with curved ($r = 25 \mu\text{m}$ and $r = 224 \mu\text{m}$) and flat end-faces, corresponding exposure laser profiles are shown as insets. Structures presented on central and right pictures are fabricated using circular and rectangular apertures, while the waveguide on the left picture is exposed with a focused Gaussian laser beam $\varnothing 33 \mu\text{m}$.

The influence of an end-face shape and a gap on the light coupling efficiency between two end-faces of a discontinuous waveguide is analyzed for curved and flat end-faces in air and water. The spatial distribution of the light emitted from different polymer waveguide surfaces is characterized using a beam profiler based on a CMOS sensor Omnivision OV5647. From the obtained images, width and height of the light spot are derived using a two-dimensional Gaussian cross section fit. Fig. 4.8 presents the measured light intensity distribution and graphs with light spot width behind

waveguides with flat and curved end-faces with the radius of curvature $r = 62.5 \mu\text{m}$ [148]. Similar formation of emission cones behind a lensed multi-mode fiber is presented along with a numerical description based on ray tracing and light source modeling by Bescherer et al [149]. Waveguides with curved end-faces act as a cylindrical collecting lenses focusing light in one dimension at the curved surface. In contrast, waveguides with flat end-faces do not change the light propagation front and could be considered as rectangular flat emitting surfaces.

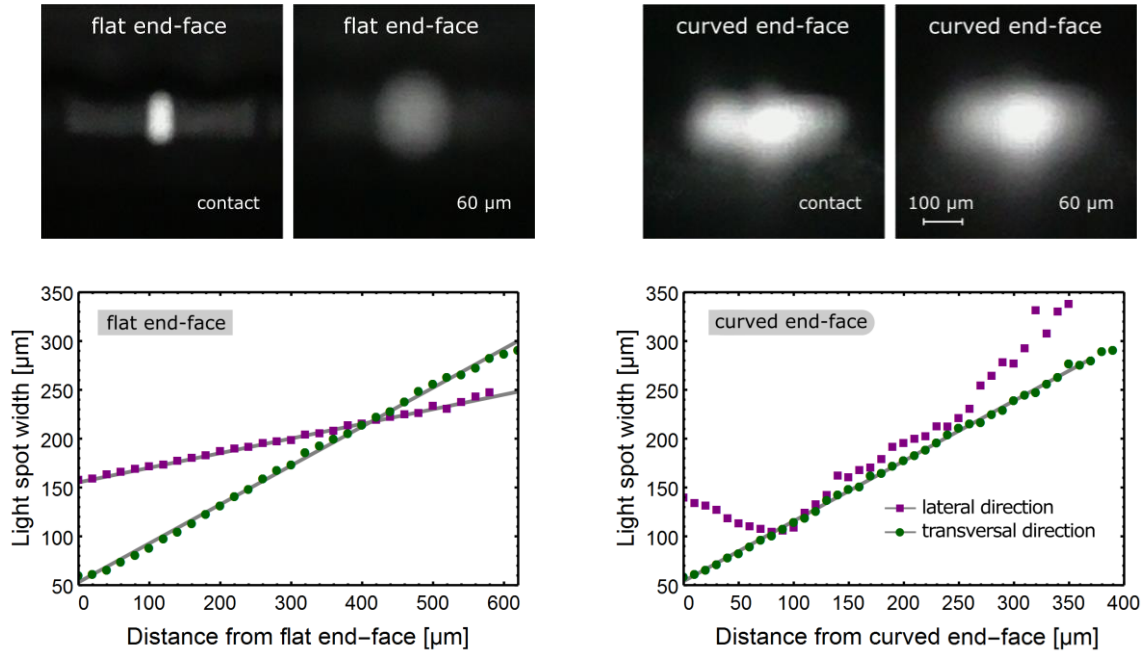


Fig. 4.8: Near-field images of flat-ended (left) and curved (right) polymer waveguide end-faces obtained by a CMOS chip in contact with the end-face and at the distance of $60 \mu\text{m}$. Graphs below: (left) no focussing in both transversal (green circles) and lateral (purple squares) directions for waveguides with flat end-faces; (right) light leaving a curved waveguide gets focused only in lateral direction while it diverges in the transversal direction.

As a next step, the transmitted power in free propagation region of discontinuous waveguides with flat and curved end-faces is analyzed. For this purpose, a setup consisting of two 3-axis flexure stages MicroBlock™ MBT616D/M (Thorlabs, Inc.) with a tilt module, a motorized linear stage LTS300/M (Thorlabs, Inc.), and a 3D printed box with two openings fulfilling a function of a fluidic cuvette for measurement of transmitted power in different fluids (air, water) for various gaps is assembled (see Fig. 4.9). In order to maintain the focus position of the CMOS camera during the gap change, the flexure stage with the second substrate and the CMOS camera are fixed on the motorized linear stage.

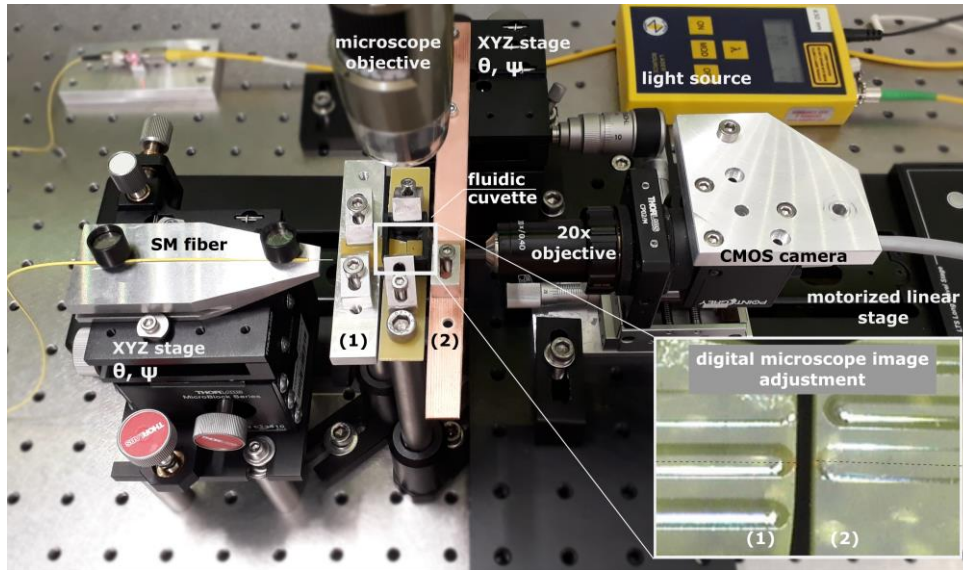


Fig. 4.9: Experimental setup for alignment of the waveguide end-faces on two separate boards (1) and (2) with a various gap between them.

In fluidic cuvette, two equal waveguides with curved ($r = 125 \mu\text{m}$) or flat end-faces (width $250 \mu\text{m}$) are positioned facing each other with an air gap in between. Light from a laser diode with a central wavelength of $\lambda = 850 \text{ nm}$ is coupled by a single-mode optical fiber SM800-5.6-125 to the waveguide on the first substrate (1), which position is fixed. The transmitted power is measured after the waveguide on the second substrate (2), while the gap between the waveguide end-faces is changed stepwise in the range of $100 - 900 \mu\text{m}$ using the motorized linear stage. The transmitted power is determined in arbitrary units by integration of the intensity distribution, obtained from CMOS camera pictures, over the waveguide core cross section area. The procedure is repeated with a water-filled cuvette. The data obtained from multiple measurements for waveguides with curved and flat end-faces in air and water is shown in Fig. 4.10 [148].

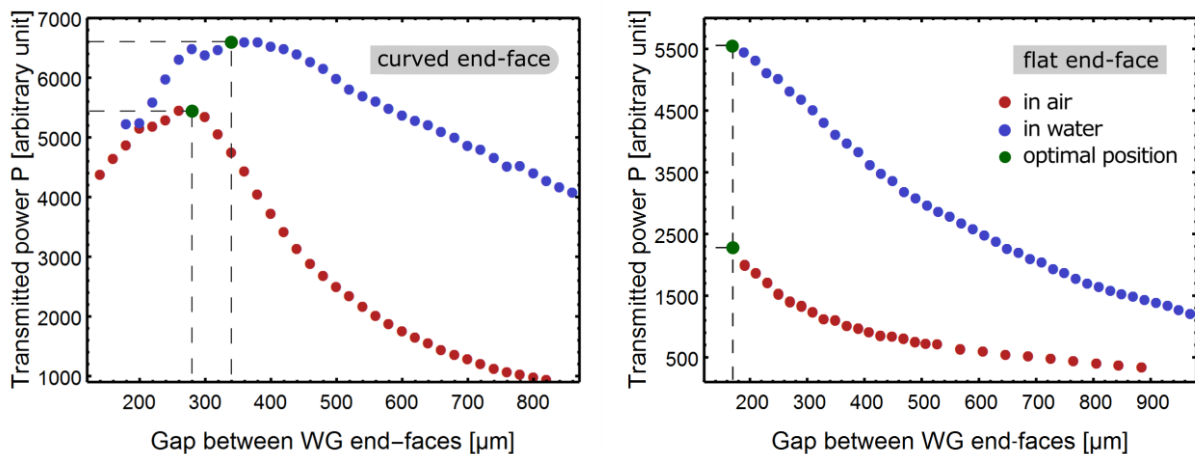


Fig. 4.10: Experimental determination of transmitted optical power P in air (red dots) and water (blue dots) for waveguides with curved (left) and flat (right) end-faces as a function of the gap between them; gaps with optimum coupling positions are marked as dark green dots.

The waveguides with curved and flat end-faces behave differently in mediums with different refractive indices, such as air and water. It can be observed that the tested curved waveguides

possess a coupling optimum at nonzero gap. In air, the maximum of transmitted optical power occurs at a gap of 280 μm . This value increases to approximately 340 – 360 μm in water. In contrast, flat-end waveguides require butt-coupling for optimal signal transfer in both air and water. Introduction of a gap leads to gradual decrease in the coupling efficiency. At the same time, curved waveguides show a better coupling efficiency compared to flat-end waveguides at the same gap width [148]. For both end-face geometries, an increase of transmitted light power in water is observed. This can be explained by reduction of refractive index contrast, and thus decrease of the divergence angle and Fresnel losses. Despite the same cross sectional dimensions of the tested waveguides with flat and curved end-faces, a strict quantitative comparison is complicated. This is due to the difficulties in holding constant launch conditions while carrying out the manual alignment of the waveguide's end-faces to each other in five degrees of freedom (coordinate axes xyz , pitch θ , and yaw Ψ) for each substrate (see Fig. 4.9).

The optical structure with curved end-face in horizontal plane can be considered as a converging lens. In Fig. 4.11, a schematic representation of light refraction on a spherically curved surface with a radius of curvature r is shown.

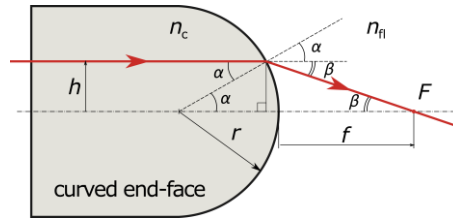


Fig. 4.11: Scheme of the light beam refraction on a curved waveguide end-face.

The calculation of focal length f of such structure with refractive index n_c placed in a fluid with refractive index n_{fl} can be calculated using Snell's law with paraxial approximation. Considering two right-angled triangles and their leg h , the following applies to beams close to the axis:

$$r \sin \alpha = h = f \tan \beta \rightarrow r \alpha \approx f \beta \rightarrow \beta = \frac{r \alpha}{f} \quad (4.4)$$

From the Snell's law of refraction (2.4) the following equality holds approximately:

$$n_c \sin \alpha = n_{fl} \sin(\alpha + \beta) \rightarrow n_c \alpha \approx n_{fl}(\alpha + \beta) \quad (4.5)$$

Considering (4.4) and (4.5), it can be shown that the focal length linearly depends on the radius of curvature and can be estimated as:

$$f = \frac{r n_{fl}}{n_c - n_{fl}} \quad (4.6)$$

Radii of the end-face curvature are equal to laser beam radius or can be additionally increased by more complex writing trajectories (see Fig. 4.7 (center) dashed line). Thus, the desired focal length can be achieved. Exemplary calculations of focal length for typical radii of curvature and surrounding media are listed in Table 4.5.

Table 4.5: Examples of calculation of focal length for curved EpoCore waveguides with different radii of curvature in air and water at 850 nm (refractive index of core $n_c = 1.587$).

Radius of curvature		$r = 25 \mu\text{m}$	$r = 125 \mu\text{m}$
Medium	n_n [150]	f [μm]	f [μm]
air	1.0002	42	213
water	1.3290	128	643

Due to the fact that spherical lens aberration, non-parallelism of the incident light beam, sidewall roughness, and other optical aberrations are neglected in the approximated calculation (4.6), the estimated focal lengths should be considered as a starting point for waveguide layout optimization. The more accurate values could be determined, e.g. using a ray tracing software. Ray tracing simulation results for an EpoCore ($n_c = 1.587$) waveguide with curved end-face and radius of curvature of $125 \mu\text{m}$ in air obtained by the open-access program "OpticalRayTracer" [151] are shown in Fig. 4.12 providing the value of focal length in air of approximately $230 \mu\text{m}$. This program has a significant limitation that only front waveguide surfaces can be made refractive and simulations are only possible in air.

For gaps $< f$, most of the refracted light can be collected by the second waveguide; however, the rays are not parallel to the optical axis. The condition of total internal reflection is not valid for all of them and thus they can leave the core later. For gap values ranging $280 \leq \text{gap} \leq 350 \mu\text{m}$, the refracted beams are mostly parallel to the optical axis; they can be accepted and guided by the second waveguide. This gap range is considered as optimal, which agrees well with experimentally obtained result of $280 \mu\text{m}$. The distance of $426 \mu\text{m}$ corresponds to doubled focal length of $213 \mu\text{m}$ calculated from (4.6). For this gap, the rays collected by the second waveguide are mostly parallel to the optical axis. However, such big distance leads to the loss of strongly refracted rays and thus to additional coupling losses.

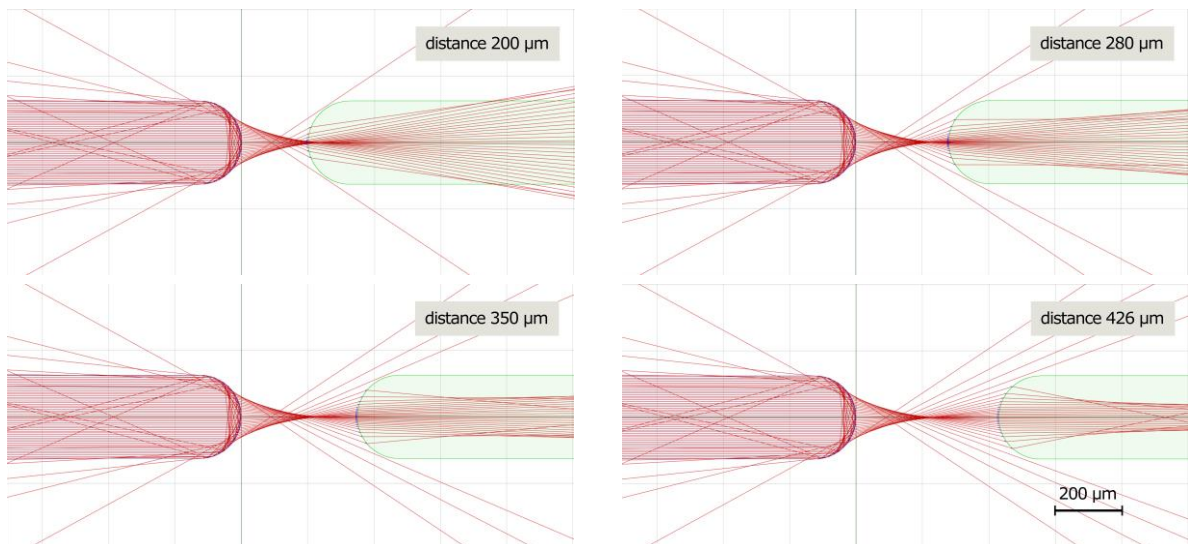


Fig. 4.12: Ray tracing results for curved waveguides with radius of curvature of $r = 125 \mu\text{m}$ and various gaps between end-faces of 200, 280, 350 and $426 \mu\text{m}$, from left to right respectively.

In addition to determining focal length, an interesting observation can be mentioned from the ray tracing simulation results. The large amount of incident rays is reflected back because of the total internal reflection occurring on the boundary surface. This mechanism is highly dependent on the refractive index of the surrounding medium and could be exploited for refractive index measurements and monitoring of fluids as was demonstrated by Nath et al. in [152]. One of the demonstrators considered in this project, a Fresnel-refractometer, utilizes this physical phenomenon (see section 5.2).

The geometry of waveguide end-face can be selected depending on desired detection mechanism of optofluidic sensor. Both end-face geometries find applications in through-beam sensors for absorption measurements. The waveguides with flat end-face are less sensitive to refractive index changes. The coupling efficiency of discontinuous waveguides with curved end-faces can be adjusted for the different gap width by variation of their radius of curvature as discussed by Sergeeva et al. [148]. Thus, they could be successfully used in measurements of refractive index and in through-beam sensors.

4.4 Mode Behavior in Fabricated Single-Mode Waveguides

The single-mode waveguides are essential for proper operation of interferometric sensors and optical modulators considered in section 5.4. By optimized laser direct writing approach, optical structures made of EpoCore with cross-sectional dimensions of approximately $3.5 \times 6 \mu\text{m}^2$ are fabricated on FR-4 substrate (see section 3.4.5). As it was already calculated in section 2.1.5 using the equation (2.15), the EpoCore waveguide with EpoClad as cladding operates in the pure single-mode regime for cross-sectional dimensions of $2.52 \leq a_{\text{SM}}(850 \text{ nm}) < 3.57 \mu\text{m}$ at $\lambda = 850 \text{ nm}$ and $3.88 \leq a_{\text{SM}}(1310 \text{ nm}) < 5.51 \mu\text{m}$ at $\lambda = 1310 \text{ nm}$. The minimal dimensions of the fabricated rectangular waveguide core are slightly larger than calculated values for single-mode operation in NIR range. This section studies the mode behavior of these few-mode waveguides.

In general, the number of guided modes decreases with increasing light wavelength, see equation (2.12). According to an open source 2D multilayer mode solver from the University of Twente [57], a $3.5 \times 6 \mu\text{m}^2$ EpoCore waveguide can guide up to four TEM modes at a wavelength of 850 nm, namely TEM_{00} , TEM_{01} , TEM_{10} , TEM_{02} (see Fig. 2.3 in section 2.1.5). At a wavelength of 650 nm the number of supported modes increases up to seven: the TEM_{11} , TEM_{03} , and TEM_{12} can be additionally supported by the waveguide.

For a $3.5 \times 6 \mu\text{m}^2$ rectangular waveguide, the open source mode solver [57] predicts only one guided fundamental mode TEM_{00} at wavelengths above $1.408 \mu\text{m}$. With significant increase of the operational light wavelength even the fundamental mode disappears - no modes are supported by the waveguide (cutoff wavelength). According to the equation (2.14) for the rectangular waveguide, the operation only below the cutoff wavelength of $\lambda_c = 2.02 \mu\text{m}$ is possible.

Digital microscope images in Fig. 4.13 show different light modes propagating in the fabricated $3.5 \times 6 \mu\text{m}^2$ EpoCore waveguide at wavelengths of 650 nm and 850 nm. The waveguide end-faces are polished according to the process description given in section 3.5.1. The light coupling is performed by butt-coupling of cleaved single-mode optical fibers SM800-5.6-125 (850 nm) and SM600 (650 nm) (Thorlabs, Inc.) with application of index-matching gel. Fiber-coupled laser diodes

FOSS-21-3S-5/125-850-S-1 (central wavelength of 850 nm) and FOSS-21-3S-4/125-650-S-1 (central wavelength of 650 nm) (OZ Optics Ltd.) serve as light sources.

Depending on the coupling conditions, namely on the lateral position and angle between the waveguide end-face and the coupling fiber, and on the wavelength of light source, one can observe either pure TEM modes or a superposition of several modes. At a wavelength of 650 nm, the lowest and highest observed modes are TEM_{11} and TEM_{03} and at $\lambda = 850$ nm the lowest and highest observed modes are the TEM_{00} and TEM_{02} .



Fig. 4.13: Digital microscope pictures of the $3.5 \times 6 \mu\text{m}^2$ waveguide operating in few mode regime. From left to right: polished waveguide core end-face without light, TEM_{11} and TEM_{12} at the wavelength of 650 nm; TEM_{00} and TEM_{01} at $\lambda = 850$ nm.

These preliminary results demonstrate the possibility of fabrication of photonic light guiding structures showing few-mode behavior on EOCB. These guiding structures build a fundamental base for a EOCB-based Mach-Zehnder interferometer presented in section 5.4.

5 Optofluidic Platforms and Lab-on-a-Board Demonstrators

Sensing fluid parameters is important in many industries, such as food, environment, chemical, and biotechnology. In understanding and monitoring the regulation mechanisms in fragile aquatic ecosystems, many parameters related to water characteristics are of enormous importance. These include e.g. distribution of turbidity, refractive index, dissolved organic matter, sulfide-, oxygen-, nitrate-, CO₂-concentration, pH-value, and temperature in different sea layers [153, 154]. While a direct measurement is sometimes cumbersome, these parameters can be determined indirectly by measuring optical properties, such as absorption, fluorescence, luminescence, color, among others. Due to the large scale presence of waterbodies, space- and airborne sensors for remote measurement in combination with telemetry using small portable sensors for *in situ* analysis are required. These will enable comprehensive monitoring of spatial and temporal distribution of water quality indicators [154–156].

The technological process chain mentioned in previous chapters is used to fabricate photopolymer-based multilayer optofluidic platforms. Here, the optical waveguides with different end-face geometries are synergistically combined with microfluidic channels or open cuvettes. They build the basis for versatile analytical lab-on-a-board systems able to meet requirements of small footprint and weight.

Plenty of compact optical fluid sensing approaches exploiting wide range of physical phenomena are reported in academia and industry, e.g. [7, 9, 157, 158]. The light parameters, such as amplitude, wavelength, polarization state, and phase, can be monitored. In all optofluidic detection mechanisms, light interacts with a fluid and optionally objects inside the sensing area. The degree of the light-fluid interaction defines the output sensing results [9, 159]. Many advanced sensing applications are implemented using single-mode waveguides utilizing the principles of interferometry [160] and plasmonics [161], or as complex optical structures, such as resonators and gratings [7, 162]. In case of selective and labeled detection of a specific analyte, it requires functionalization [6]. These methods require complex process chains and strict fabrication tolerances.

As already described in chapter 1, four optofluidic demonstrators are chosen for technological evaluation and EOCB-integration. They encompass detection of the most important physical and chemical fluid properties, such as refractive index, spectral transmission, and turbidity. Due to their simplicity, robustness, and reliability, the well-established fiber-based optical sensing approaches are adopted for compact EOCB-based implementation. This chapter introduces their design, working principles and sensing performance. The EOCB-based implementation of demonstrators forms the second part of this chapter.

5.1 Absorption-based Sensor Unit on EOCBs

Water turbidity is one of the most important water quality indicators. It can be caused by suspended solids, air bubbles, dissolved organic, and inorganic matter. The concentration and properties of

dissolved organic matter is measured using absorption spectroscopy either in ultraviolet-visible spectral band ($\lambda = 220 - 720$ nm) or using fluorescence [156]. Existing devices for *in situ* estimation of water quality parameters are robust and highly sensitive. Nevertheless, they are mostly either bulky, expensive or outdated [154, 156]. The most common parameter for specification of waterbody transparency remains the Secchi disk depth [163]. This method was established in 1865 by Pietro Angelo Secchi and is based on light attenuation. Here, a disk with black and white pattern is mounted on a rope and submerged in water until the pattern is invisible. The length of the rope below the surface represents the Secchi disk depth. Besides this outdated method, state-of-the-art research is performed on remote sensing of water transparency using air- or spaceborne as well as by *in situ* telemetric sensing with fiber-optic spectrometers, e.g. [154, 163].

Prompted by the necessity of lightweight and compact water analysis sensors with small instrumentation footprint, an EOCB-based implementation of water sensing platform is suggested. The chosen configuration with two discontinuous waveguides is schematically illustrated in Fig. 5.1. The light guided by a waveguide propagates through the interaction region in a cuvette filled with an analyte and gets scattered or absorbed according to Lambert-Beer's absorption law [164]. On the opposite side it is collected by a second waveguide and guided to the detector. The decay in power of the collected light measured at one or more distinct wavelengths allows one to derive information about the fluid's wavelength-specific absorption and thus about its turbidity. This configuration with free-space light propagation could also be used for fluorescence analysis and absorption spectroscopy in clinical chemistry, e.g. for serum, urine, and saliva tests [66].

The insufficient transmittance in ultraviolet-visible (UV-Vis) light spectrum of the epoxy-based photopolymers (for a detailed description on spectral transmittance in epoxy-based polymers see subchapter 4.1.2) used for fabrication of EOCBs can be overcome by working in the infrared wavelength range. A short measuring distance, resulting in downscaling of the footprint, is an important advantage of absorption- or scattering-based measurement method. However, the arrangement with free-space light propagation is associated with additional calculations and experimental work regarding optimization of the gap and shape of the waveguide's end-faces for better light coupling.

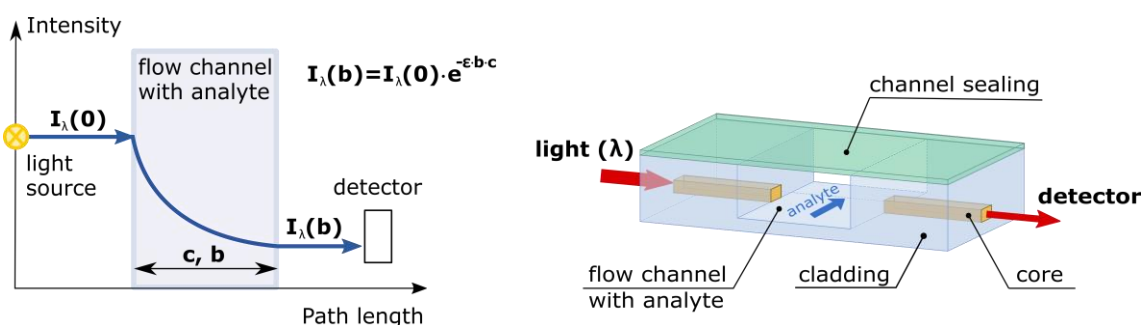


Fig. 5.1: (Left) The graphical representation of Lambert-Beer's law: attenuation of transmitted light intensity depending on fluid concentration. Equation parameters: I - light intensity, b - transmission length, ϵ - molar absorption coefficient, c - analyte concentration; (right) schematic drawing of integrated optical waveguides in a free-space light propagation based optofluidic device.

For the lab-on-a-board implementation, an electric printed circuit board (PCB) and an optical board are mechanically connected to each other. The PCB carries all electronic components, including light sources, and photodiodes, while the optical sensor board incorporates optical polymer waveguides and

microfluidic structures, such as cuvettes or channels. As both use the same substrate material (FR-4), they could be fabricated on a single multilayer board to reduce the complexity and the footprint. However, in order to replace the optical board in a quick and easy way after its failure due to deterioration, wear or damage in the real working conditions, the electronic and optical functions are separated on two boards as shown in Fig. 5.2 [148].

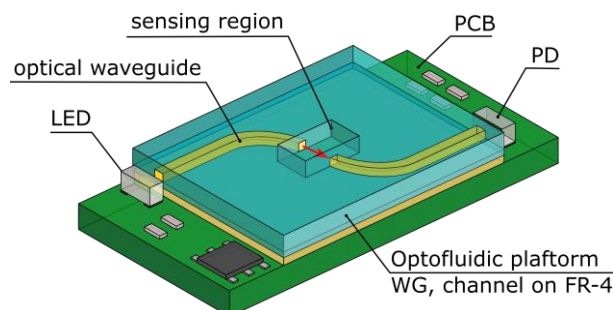


Fig. 5.2: Schematic representation of EOCB-based optofluidic sensing platform.

The fabricated optofluidic board, presented later in this chapter (see Fig. 5.7), has two sensing areas and a footprint of $45 \times 45 \text{ mm}^2$, which can be potentially reduced down to $6 \times 20 \text{ mm}^2$. For implementation of the optofluidic platform, straight discontinuous waveguides made of EpoCore/EpoClad material combination are chosen. The integrated waveguides have cross-sectional dimensions of $50 \times 250 \mu\text{m}^2$ and curved end-faces with a radius of curvature of $r = 225 \mu\text{m}$, see Fig. 5.3. Such big radii of curvature of the waveguide's end-faces are used for increasing the optimal gap, which defines the length of the absorption path, and thus for improvement of the sensor performance. The waveguides are adjusted to each other with a gap of $470 \mu\text{m}$, which has been calculated following considerations given in subchapter 4.3, for a better light coupling within the sensing region.



Fig. 5.3: (Left) Discontinuous waveguide with curved end-faces with a radius of curvature of $225 \mu\text{m}$; (right) propagation of light with a wavelength of 650 nm through a light-fluid interaction region in a microcuvette. The microscopic pictures are obtained using a digital microscope Keyence VHX-5000.

The waveguides are integrated into 1 mm wide microchannels, sealed by a dry photoresist laminate, or into $3 \times 2 \text{ mm}^2$ non-sealed fluidic cuvettes (open fluidics) structured in the upper cladding layer. Working with open fluidics has an advantage of avoiding the cleaning issues which otherwise arise for narrow microchannels (width $< 100 \mu\text{m}$). Furthermore, no syringe pump is required for liquid delivery resulting in a reduction of the device footprint and volume of test fluid. The open fluidic configuration enables uninterrupted immersed measurements of water parameters and is chosen for our laboratory tests. The testing of the sensor unit's performance and its EOCB-implementation are discussed in the following sections.

5.1.1 Optical Board for a Miniaturized Turbidity Measurement Setup: Laboratory Tests

The fabricated optofluidic board is initially validated in a laboratory environment using external, non-integrated measurement equipment. Figure 5.4 illustrates the setup for laboratory testing consisting of: **(1)** syringe pump (KD Scientific 210) with syringes filled with the sample fluid; **(2)** fluidic connection tubes; **(3)** fabricated all-polymer optofluidic platform (for configuration see section 5.1) butt-coupled by cleaved glass fibers to a light source and a detector using two 3-axis flexure stages MicroBlock™ MBT616D/M (Thorlabs, Inc.). The sensing platform is placed on a $40 \times 40 \text{ mm}^2$ Peltier element TEC1-127060 controlled by a TEC-1091 controller (Meerstetter Engineering GmbH) for temperature stabilization; **(4)** fiber-coupled narrowband laser diodes FOSS-21-3S-4/125-650(850)-S-1 (OZ optics Ltd.) with central wavelengths of 650 nm and 850 nm, respectively, or stabilized broadband tungsten lamp SLS201L (Thorlabs, Inc.) with a spectral range of 360 – 2600 nm serve as light sources; **(5)** sufficiently sensitive detection unit for monitoring the output signal fluctuations. Depending on the light source, it is a photodiode in combination with a highly sensitive 34461A multimeter (Keysight Technologies, for narrowband light source) or USB 2000 spectrometer (Ocean Optics Corp., for broadband light source) covering a spectral range of 174.6 – 890.0 nm.

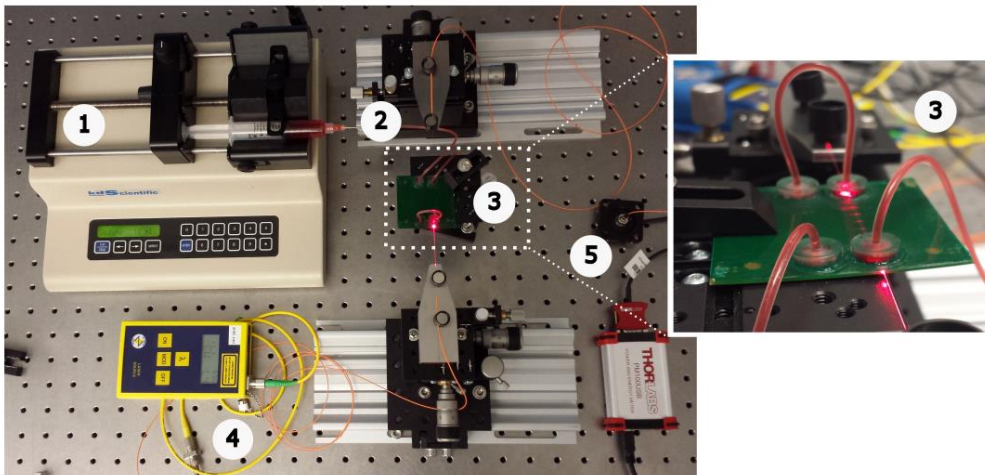


Fig. 5.4: Experimental setup for monochromatic absorption-based fluid analysis: (1) syringe pump for continuous fluid delivery, (2) connection tubes, (3) all-polymer optofluidic board, (4) light source, and (5) detector unit.

A mixture of cow milk with a fat content of 3.9 % and water serves as a test fluid in the demonstration setup for turbidity and concentration measurements. Due to the fact that the main milk components, such as water, fat, and protein, have no absorption lines within the used spectral interval, the purely scattering-based milk concentration determination can be performed using this optical setup.

The spectrometer in combination with broadband tungsten lamp is used in the detector setup. For each measurement, the output signal is measured in the arbitrary unit *counts* in range of 0 – 4000 and is recorded versus wavelength while the exposure time of the spectrometer is held constant. Here, the *counts* value refers to the radiative power per unit surface area, wavelength interval and exposure time. Input and output values for full spectral range are summed up and then compared to each other, knowing that the signal from the spectrometer is proportional to power and exposure time. The calculated data is plotted for different milk concentrations c , see Fig. 5.5. The signal by deionized (DI)

water is taken as a reference power (P_0). The fitted calibration function represents the exponential dependence of relative transmitted light intensity on concentration of milk in DI-water.

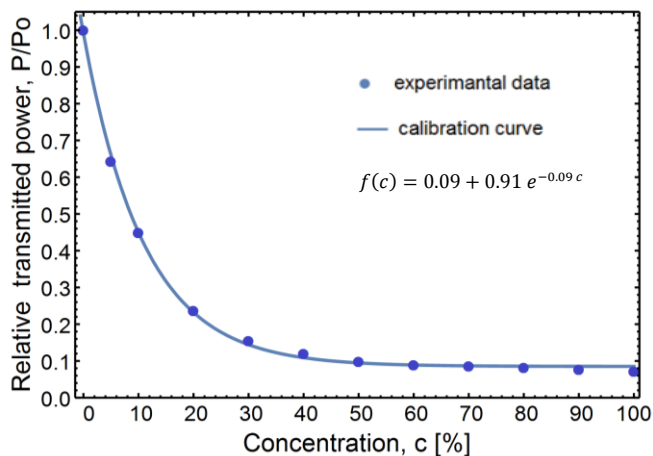


Fig. 5.5: Exponential decay of relative transmitted light power (P/P_0) versus concentration (c) of 3.9% milk in DI-water. Measurement results are normalized to the power signal (P_0) obtained by DI-water in the microchannel. Calibration curve takes the form: $f(c) = 0.09 + 0.91 e^{-0.09c}$.

These primary measurements confirm that this optofluidic demonstrator is suitable for concentration measurements in fluids. Turbidity may be then derived from concentration values. The current setup with a broadband light source provides a detection threshold of 6 % of milk concentration. An improved detection limit could be obtained by using a narrowband stabilized light source (laser or LED) in combination with amplified photodiodes and improved measurement scheme, including relative measurement using a reference path or involving lock-in amplifiers.

5.1.2 Absorption-based Demonstrator on EOCBs: Assembly and Performance^a

This section is dedicated to the implementation of the miniaturized EOCB absorption-based demonstrator. Here, surface-mounted light emitting diodes (LEDs) KPTD-1608LVSECK-J3-PF (Kingbright) [166] serve as light sources covering several wavelengths. The same LEDs are used as photodiodes (PD) inversely connected to a current-to-voltage transimpedance amplification circuit and are used as detection units providing a light intensity dependent voltage signal.

Despite advantages of LEDs, such as low-cost, availability in diverse wavelengths, and simple external circuitry, they have a wide emission angle (typically 120°). This limits their application in optical sensing and telecommunication, where targeted light irradiation of the waveguide's core is essential. Selective core illumination could enable the introduction of straight and shorter waveguides into the optofluidic platform. Towards the targeted core illumination, a concept for optical coupling of miniature surface-mounted LEDs to polymer-based optical waveguides on EOCB with laser-cut circular apertures is proposed.

In particular, a LED-module consists of a carrier-board holding one or more inversely-mounted LEDs and a metal sheet with an aperture mounted between LED's emission surface and the waveguide end-

^a Material of this section is based on the co-supervised master project of M.Sc. Jendrik Schmidt [165].

face. A proposed concept is schematically illustrated in Fig. 5.6 a). The 100 μm thick brass or steel foils with laser-cut circular alignment and aperture holes with diameters from 30 μm to 100 μm are used. Laser cutting is done in-house or by external companies fabricating metal-based solder masks. Beside the aperture for light, the metal foils have additional holes for alignment to the carrier-board with soldered LEDs by means of alignment pins. The use of apertures with a smaller diameter allows an increased brightness contrast between core and cladding at the waveguide's output by preventing the light penetration into the cladding. The aperture pitch in the metal foil can be precisely matched to the waveguide pitch with deviations of only a few micrometers. This significantly relaxes requirements to individual LED mounting. Since no refractive micro-optical components are required, the presented concept is simple and robust [167]. However, the measurements of the transmitted optical power show that the total LED power is reduced by about 30 dB by the aperture [165].

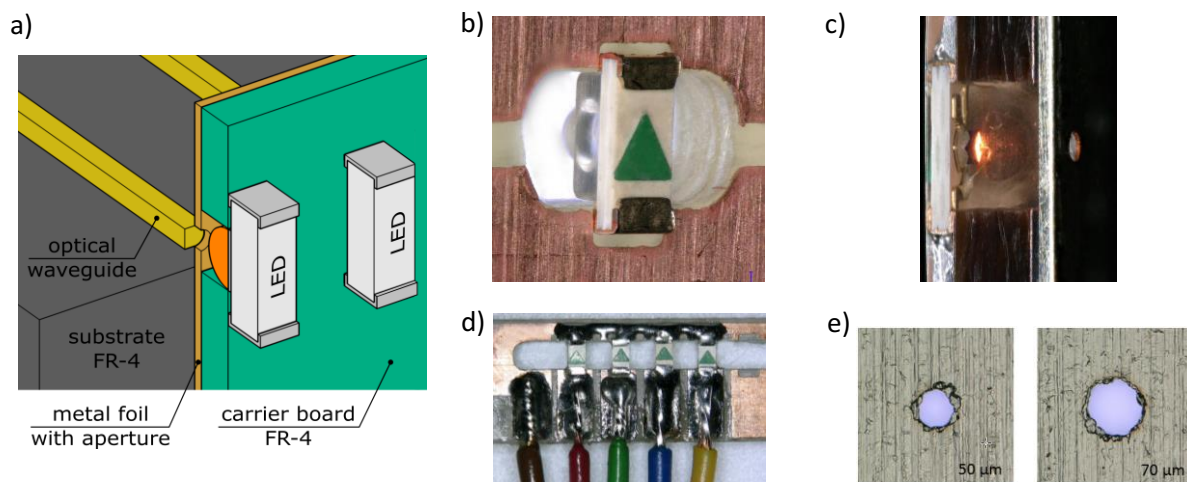


Fig. 5.6: a) Schematic drawing of multiple LED modules coupled to a waveguide array; b) reverse mounted LED in a milled opening of the carrier board with solder pads; c) cross section of an emitting, soldered and glued LED-module aligned to the $\text{\O}50\ \mu\text{m}$ circular aperture in a steel foil; d) LED array with colors red, green, blue, yellow; e) microscope images of laser-cut apertures with diameters of 50 and 70 μm in a 100 μm thick steel foil (production by external company).

Electrical connections to the LEDs are established through solder pads on the carrier board and the EOCB. The module components are mounted and then placed perpendicular to the EOCB in front of the waveguide's end-faces where it is glued by UV-irradiation of optical adhesive NOA 81 (Norland Products, Inc.). Figure 5.7 a), c) represent the alignment of an LED-module to an optical sensor board. Alignment of LED-module to optical board is at the development stage. The manual adjustment and fixing by gluing is a temporary solution. 90° turns are introduced in order to prevent the detection of residual light propagating outside the waveguide core. These measures result in an improved signal-to-noise ratio, lower detection threshold, and a more compact sensor implementation.

The performance of the EOCB-based demonstrator is tested on green food dye (Dr. Oetker) mixed in DI-water. The dye concentration in DI-water is gradually varied in steps of 10 %, see Fig. 5.7 e). 10 μL droplets are sequentially applied into the cuvette between the waveguide end-faces using an Eppendorf pipette, see Fig. 5.7 d). Between measurements, the sensing region is rinsed with water, carefully wiped with a cloth and dried with compressed air. The reference is set to 3.9 V for DI-water in sensing region. Due to high losses from the circular aperture filter and relatively high propagation losses in the polymer waveguides, the maximum possible operational current of 30 mA should be set

for the LED resulting in a radiant power behind the aperture of $19 \mu\text{W}$. The required signal amplification gain is $250 \cdot 10^6$, which allows to detect a minimum power of 74 pW [165]. The length of polymer waveguides is reduced to $15 - 20 \text{ mm}$ in order to increase the output signal level lowered by length-dependent propagation losses.

The entire measurement series are performed in a darkened room at wavelength of 625 nm . Each of the prepared water-dye solutions is measured three times in intervals of 10 s . Measurement errors can be caused by the changes in ambient light, mechanical instabilities, or changes in concentration due to contamination.

In Fig. 5.7 b), the measured photodiode output voltage is plotted for different concentrations of green food dye in DI-water. The fitted function represents the exponential decay of the obtained signal (relative transmitted optical power) with increasing dye concentration. The detection threshold is estimated to be approximately 3 % of food dye concentration in DI-water.

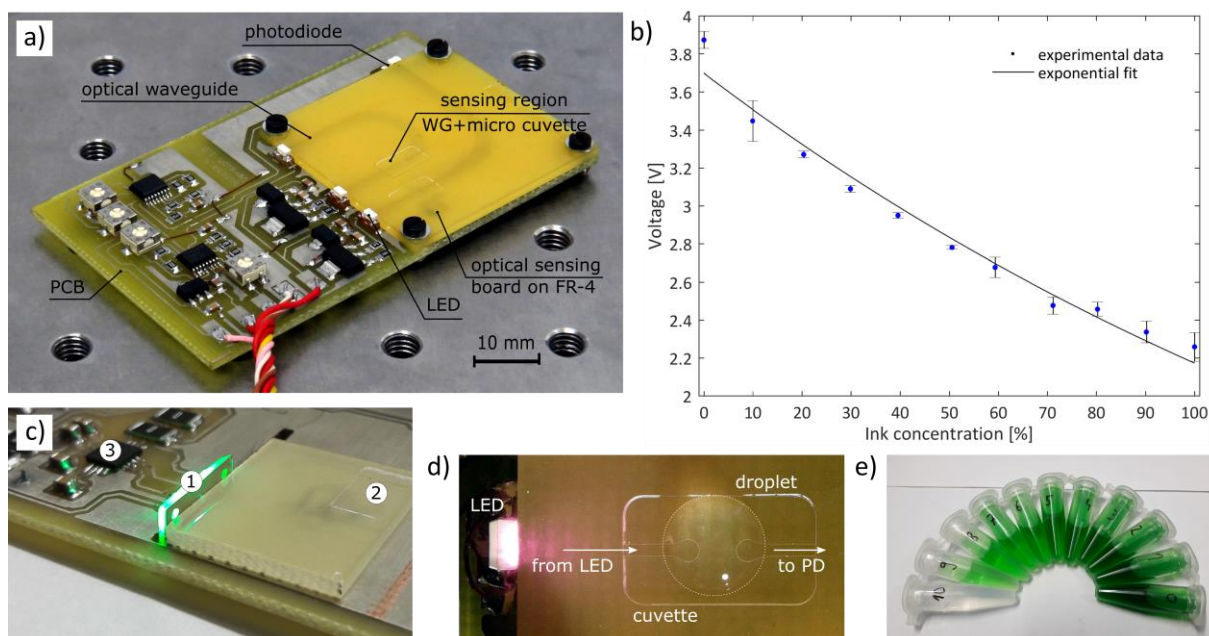


Fig. 5.7: Pre-assembled optofluidic sensor on EOCB: a), d) a micro-cuvette is integrated into the optical layer formed by 90° and U-turn waveguides with curved end-faces [148]; b) results of absorption measurement in a green food dye-water mixture using the EOCB-demonstrator; c) the LED module (1) is manually aligned to the optical sensor board (2) and connected to the driver electronics (3) on its backside; e) green food dye-water mixture samples with different concentrations.

This experiment confirms that the absorption measurements by the proposed EOCB-based optofluidic platform are feasible. This device has a small footprint and is thus suitable for telemetry applications. By further improvement of the optical layout and use of other wavelengths, which show less propagation losses in polymer waveguides (e.g. at $\lambda = 850 \text{ nm}$), the amplification gain can be reduced by one or two orders of magnitude, which at the same time will significantly enhance the quality of the measured signal. Also, the implementation of more advanced detection schemes using modulated light sources, so-called lock-in amplification, would be a next logical step. A combination of arrayed waveguides and rectangular aperture filters may lead to a better adjustment of the size and the location of the LED's emission area to the array of optical waveguides and thus enhance the output signal. This concept is schematically shown in Fig. 5.8 and can be tested in further experiments. Here,

instead of the pre-packaged LEDs, the integration of micro-LEDs or bare LED chips into the optofluidic platform will be pursued.

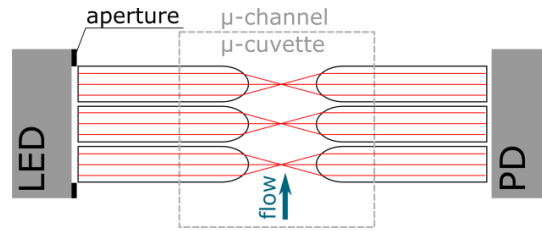


Fig. 5.8: Possibility for signal improvement by means of parallelization of optical paths.

5.2 Evanescent Field-based Sensor Unit on EOCBs

A measurement principle that is similar to attenuated total reflection (ATR) spectroscopy is implemented as a polymer-based optofluidic demonstrator. Attenuated total reflection spectroscopy is widely used in clinical diagnostics for IR measurements and is the preferred method for highly absorbing materials, where the use of conventional transmission measurements is problematic [168, 169]. In attenuated total reflection, light is guided through an optical element acting as a waveguide, whose cladding is formed by the sample fluid. While most of the light field energy is located in the optical element, a small portion (known as the *evanescent field*) extends into the fluid and hence is attenuated at wavelengths corresponding to its absorption spectrum [66]. By analyzing the spectrum of transmitted light, information about the fluid composition can be obtained. This method is a special case of evanescent wave spectroscopy. On an EOCB, it could be implemented in a way similar to the one schematically shown in Fig. 5.9. A cladding-less waveguide is placed along a microchannel filled with the sample fluid.

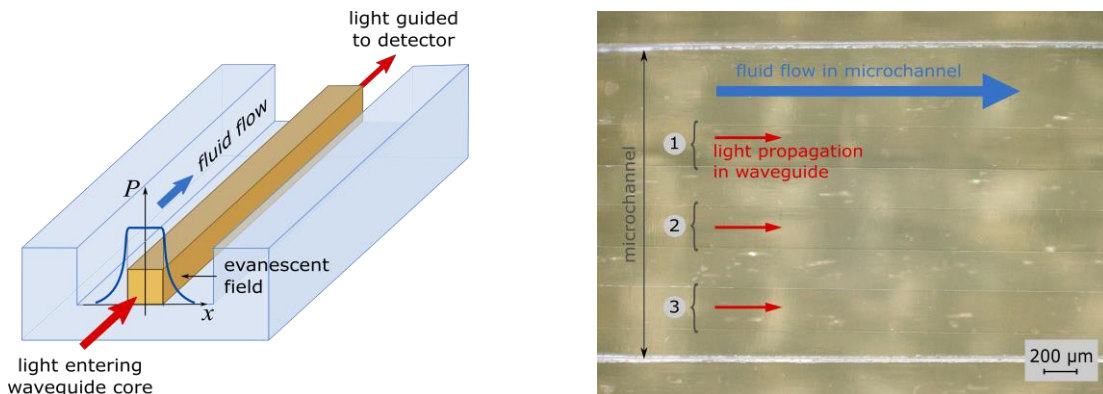


Fig. 5.9: (Left) Scheme illustrating fluid-light interaction in a microchannel and formation of an evanescent field; (right) microscopic top view of three polymer waveguides placed along a microchannel.

The penetration depth d_p of the evanescent field is defined as the distance from the interface at which the electric field amplitude falls to $1/e$ of its maximum value (refer section 2.2) and is described by equation (2.17). For example, for an EpoCore waveguide ($n_{\text{core}} = 1.587$) and water as a surrounding fluid ($n_{\text{water}} = 1.329$), the penetration depth at a wavelength of $\lambda = 850$ nm is $d_p = 250$ nm. The shorter is the wavelength, the smaller is the depth of penetration and thus the signal attenuation.

In Fig. 5.10, a fabricated optofluidic demonstrator schematically connected to an external measurement equipment is demonstrated. The setup consists of a stabilized broadband light source SLS201L (Thorlabs, Inc.) emitting in a wide wavelength range of 360 – 2600 nm, a syringe pump KD Scientific 210, and a Peltier element TEC1-127060 with controller TEC-1091 (Meerstetter Engineering GmbH) for temperature stabilization of the sensor platform. A fiber-coupled spectrometer USB 2000 (Ocean Optics, Inc.) is used as the detector unit. Its spectral range covers UV to near infrared (NIR) light range of 174.6 – 890.0 nm. The in- and output glass fibers, SMF-28 and M43L05, respectively, are butt-coupled and/or glued to the polished end-face of the polymer waveguides on the optofluidic platform.

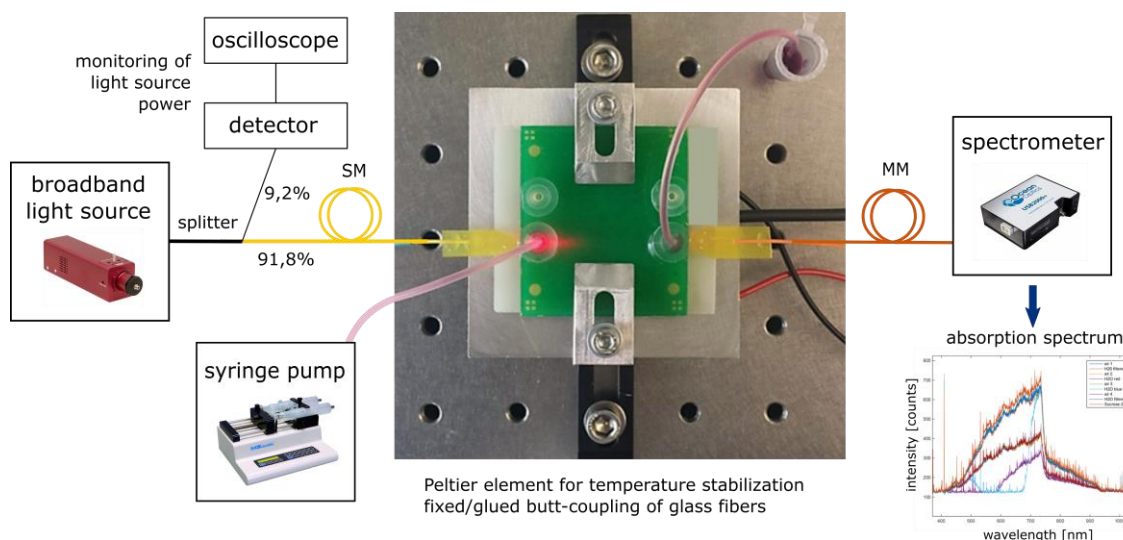


Fig. 5.10: Demonstration setup for evanescent field spectroscopy measurements consisting of an EOCB-based optofluidic platform, a syringe pump with fluidic analyte, connecting tubes, a broadband light source, and a spectrometer.

The optofluidic platform with integrated (continuous) waveguides with a cross-sectional dimension of $50 \times 250 \mu\text{m}^2$ is fabricated on FR-4 substrate. EpoCore and EpoClad are used as the waveguide core and cladding materials, respectively. Two waveguide geometries, bent and straight, are considered. Arrays of straight and bent waveguides with radii of curvature varying between 1 – 10 mm are fabricated. Straight waveguides are integrated into 1 mm wide sealed microchannels, while bent waveguides are placed into an open fluidic cuvette formed in the upper cladding layer, see Fig. 5.11 (left). Bent waveguides have the advantage of bigger penetration depth of the evanescent field due to a shift of the mode profile to the outer waveguide's sidewall [170, 171]. This presumably leads to a higher degree of light-fluid interaction. However, bent waveguides possess higher optical losses for the same waveguide length. A finite element method (FEM) simulation^a is carried out with the RF module of COMSOL Multiphysics. Fig. 5.11 (right) represents the fundamental mode TEM_{00} with its evanescent field in straight and bent EpoCore/EpoClad waveguides with radius of 1 and 10 mm and cross-sectional dimensions of $10 \times 10 \mu\text{m}^2$ at a wavelength of 600 nm. The numerical simulations were performed only for the fundamental mode of waveguides with small

^a Optical simulations are performed by M.Sc. Vaibhav Balapuram in relation to his master thesis project at the Institute of Electronic Appliances and Circuits, University of Rostock [172].

cross-sectional dimension to reduce computational complexity. However, the same trend of deeper penetration depth also applies for higher order modes and larger waveguide cores.

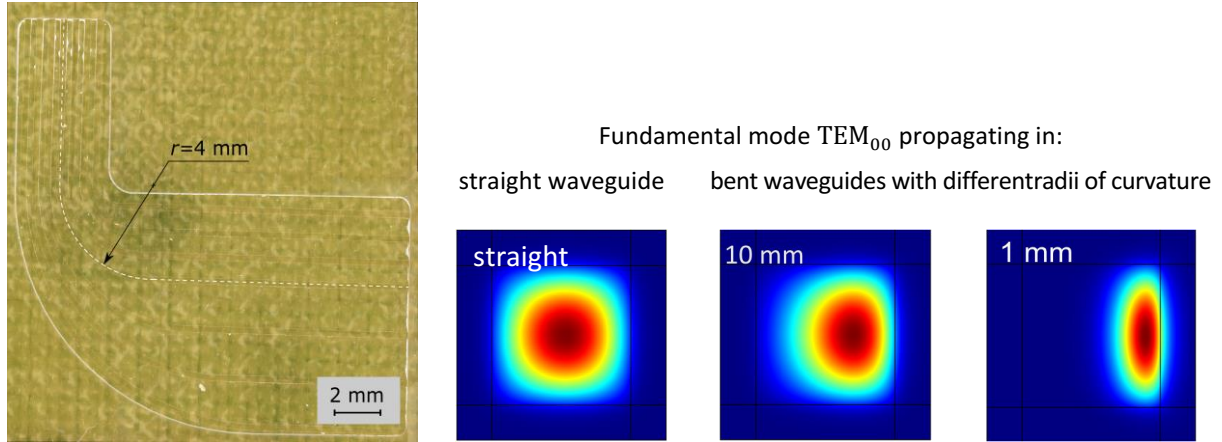


Fig. 5.11: (Left) Array of bent cladding-less waveguides with radii of curvature $r = 1 - 10$ mm on FR-4 substrate; (right) fundamental modes and evanescent field estimated by FEM simulations with RF module of COMSOL Multiphysics for $10 \times 10 \mu\text{m}^2$ straight (symmetric mode) and two bent waveguides with radii of curvature of $r = 1$ and 10 mm (asymmetric mode).

For each measurement and wavelength in the spectral range 174.6 – 890.0 nm, the spectrometer output signal in *counts* is recorded and electric dark correction is performed. In all measurements, the exposure time of the spectrometer is kept constant at 650 ms. For each sample fluid, ten time-resolved measurements, which are an average of five scans, are performed. In this experiment series, knowing that the signal from the spectrometer is proportional to power and exposure time, the absorbance is calculated for different media surrounding the waveguide core (green, yellow or red water-based food dyes). Absorbance A is defined as the logarithmic ratio of radiation power in a reference medium P_{water} to light power measured after propagation through the sample fluid P_{coloured} [173]:

$$A = \log_{10} \left(\frac{P_{\text{water}}}{P_{\text{coloured}}} \right) \quad (5.1)$$

Figure 5.12 (left, solid lines) shows the spectroscopic absorbance for the measurements conducted with a bent waveguide with a radius of curvature $r = 4$ mm. The length of the bent sensing region is 2.35 cm. This bent waveguide exhibits acceptable calculated bending and propagation losses of approximately 3.29 dB and shows a qualitatively deeper penetration length in comparison with a straight waveguide (compare Fig. 5.11, right). The maximal measured absorbance is about 0.1, which depends on the dissolved dye concentration and length of the absorption path. This dependence should be addressed in future experiments. The signal for red dye shows a peak in the wavelength range 520 – 580 nm, while for green dye a peak at wavelengths of 550 – 660 nm is observed. Yellow dye does not possess any such pronounced peaks in the presented spectral range. Based on these measurements, the color of the dye surrounding the waveguide cladding can be differentiated. The signal detected by the EOCB-based sensor appears to be noisy because its magnitude is close to the detection limit of the spectrometer. While sources of noise (spectrometer, light source, stability of the setup) have been reduced by averaging multiple spectra with long integration time and optimization of number of scans to average, there remains a characteristic structure superimposed to the spectra. The

source of this structure, which is common to all of the measurements, is assumed to originate from the light guiding properties of the waveguides.

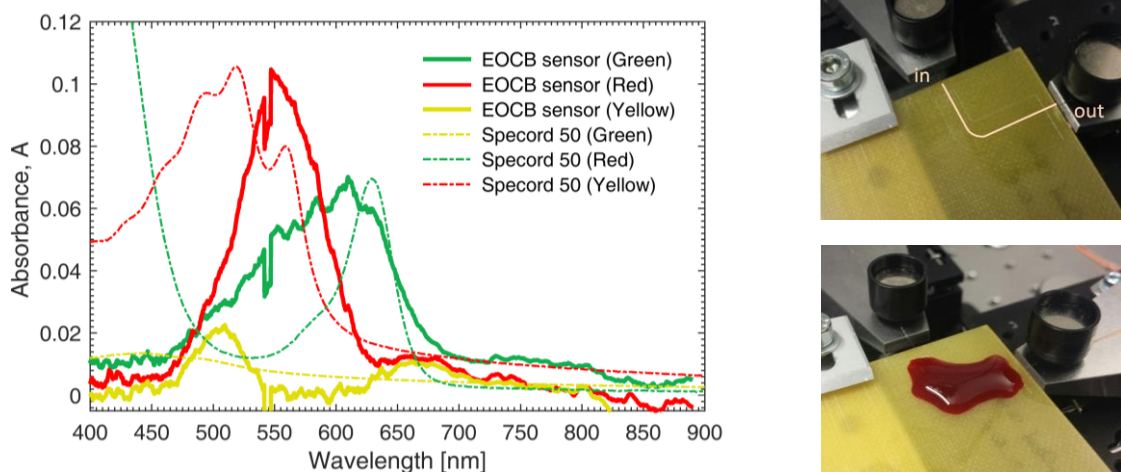


Fig. 5.12: (Left) Spectrally resolved absorbance for green, red, and yellow dyes determined using a bent waveguide with radius of curvature of 4 mm: solid lines represent the results for EOCB-based sensor, dashed lines correspond to transmission spectra obtained with a conventional spectrophotometer Specord 50; (right) photographs of laboratory setup for evanescent field absorption measurements in open cuvette with bent cladding-less waveguides on a FR-4 substrate with two butt-coupled glass fibers.

The measurements are qualitatively confirmed by the transmission measurements performed with a conventional spectrophotometer Specord 50 (Analytik Jena AG) with DI-water as a reference medium. The obtained absorption curves are fitted with the EOCB-based sensor readings by linear coefficients, see Fig. 5.12, left (dashed lines). The transmission measurements reveal strong absorbance at the wavelengths of approximately 450 – 575 nm for red, at 600 – 660 nm for green, and no pronounced absorption for yellow food dyes. The transmission spectra show absorption trends similar to spectra obtained with evanescent field spectroscopy by means of the EOCB-based sensor. However, due to fundamental differences between these sampling techniques, spectral band shifts (known as attenuated total reflection-shift [168]) and changes in relative absorption peak heights occur. The wavelength-dependent penetration depth of the evanescent field defined by equation (2.17) leads to the change in relative peak heights of attenuated total reflection spectra. The anomalous refractive index dispersion in the sample fluid at wavelengths close to its absorption bands leads to violation of the total internal reflection condition and thus to an absolute spectral band shift to longer wavelengths [169]. To allow a direct comparison to material libraries containing transmittance spectra, these factors should be mathematically compensated using an empirical ATR-correction algorithm [168, 173]. For clarity, additional experiments should be conducted with suitable fluids with clearly pronounced and known absorption lines in the Vis-NIR spectral range.

This sensor configuration and setup shown in Fig. 5.9 (left) can also be used for refractometric fluid measurements (see section 5.3 for more information about existing refractometric measurement principles). Here, the condition of total internal reflection and thus the light confinement in the core are influenced by the change in the waveguide's cladding formed by the sample fluid. The change of the fluid in the microchannel causes the variation of light intensity at the sensor output. The measurement performance of this setup is tested for DI water, ethylene glycol, and glycerin. The effects that influence the sensor signal are scattering on rough sidewalls, which depends on the refractive index contrast of core/cladding, and the number of guided modes, which depends on the

effective refractive index of the waveguide, which is a function of the refractive index of the core and the fluidic cladding. The obtained spectrally resolved signals normalized to signal in air ($P_{\text{fluid}}/P_{\text{air}}$) are shown in Fig. 5.13 (left). Figure 5.13 (right) represents the normalized output signals for DI-water, ethylene glycol, and glycerin at $\lambda = 600$ nm in dependence of their refractive index. The dependence of output signal on refractive index is confirmed. Nevertheless, additional experiments should be performed for the device evaluation and calibration and should be addressed in future work.

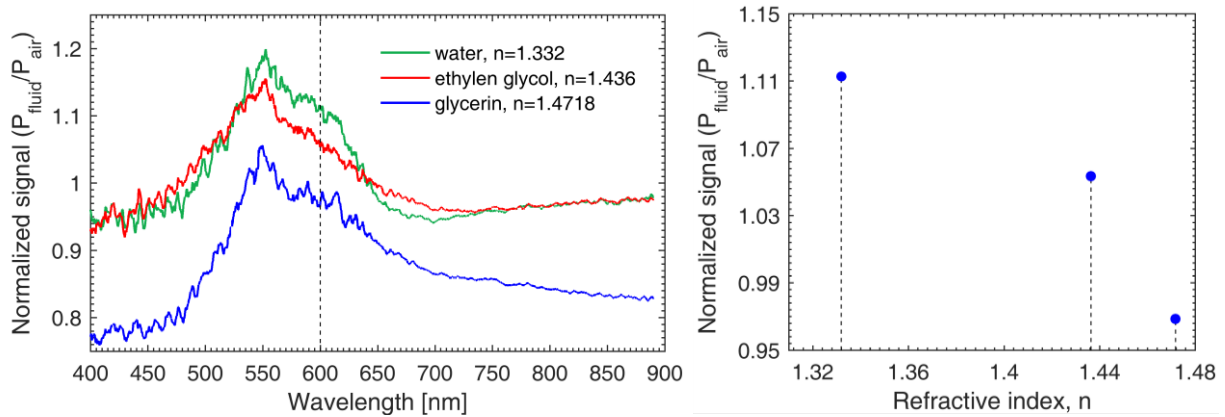


Fig. 5.13: (Left) Spectrally resolved signal for fluids with different refractive indices normalized to transmission light spectrum in air conducted for a bent waveguide with radius of curvature of 4 mm. In the legend, the RIs are given for $\lambda = 600$ nm [150]; (right) Normalized signal at the wavelength of 600 nm depending on refractive index of the fluid surrounding the cladding-less waveguide.

An improved signal-to-noise ratio can be achieved by an increased light-analyte interaction. The degree of light-analyte interaction depends on the length of the integrated waveguide that is in contact with the external medium [158] and on the wavelength-dependent penetration depth. Thus, the use of longer wavelengths, e.g. in the IR light range, together with increasing of sensing region length and bending of the waveguide, leads to enhanced output signal. There is further potential to improve the signal-to-noise ratio by relating the attenuated total reflection-spectrum to the signal from an optical reference path such that fluctuations common to both paths, e.g. light source instabilities or thermal fluctuations, are canceled out. Furthermore, in this sensor configuration (with continuous waveguides), no coupling optics are required in the sensing region, which is constructively beneficial compared to the configuration with discontinuous waveguides with curved waveguide end-faces. This sensing setup requires a stable light source and a sensitive detection unit for its reliable and stable operation. Due to the low signal level, there is no point in implementation of low-cost demonstrator on EOCB without functionalization of the waveguide surface, e.g. surface labeling for desired analyte or fluorescence detection.

An improved method of evanescent field measurements is based on the physical phenomenon of surface plasmon resonance (SPR). Here, the waveguide surface is coated with a several tens of nanometers thick metal layer of gold or/and silver. The metal-coated cladding-less waveguide and the sample fluid are brought in contact. When the electromagnetic field propagates in the waveguide along with the metal surface, the refractive index variation of the medium above the metal film will change the propagation constant of the light, as well as the resonance wavelength, the mode field distribution, and the phase of guided optical waves [161]. These changes can be used for precise refractive index measurement with detection limit in the range of $10^{-5} - 10^{-7}$ refractive index unit (RIU). This label-free and real-time detection principle has the potential to be performed using

metalized integrated multi-mode or single-mode waveguides on EOCBs and LEDs as light sources. Thus, Suzuki et al. reports a cost-effective refractometer with detection limit of $2.3 \cdot 10^{-5}$ performed with a metalized Pyrex glass plate, a polarizer foil, two LEDs with different wavelengths, and a photodiode [174]. Its implementation and evaluation should be pursued in further work. In order to implement the evanescent field-based sensors with signal improvement by surface plasmon resonance completely on EOCB, the bulky fiber-coupled broadband tungsten light source should be replaced with one or more LEDs covering several distinctive wavelengths. Instead of the spectrometer, spectrally narrowband photodiodes with current-to-voltage amplification can be used, as it was done for the transmission-based sensor unit on EOCB presented in section 5.1.

5.3 Fresnel-Refractometer on EOCBs^a

For many biological, chemical, and environmental applications, the measurement of refractive index is of major interest for detecting special liquid compounds [13, 158]. From this property, conclusions about its purity, variations in the chemical composition, and concentration can be made. There are many measuring techniques for refractive index determination. The most advanced ones use microring resonators [175], waveguides with liquid cores [176], microstructured photonic crystal fibers filled with analyte [177, 178], and the phenomenon of surface plasmon resonance [161] in order to increase the light-fluid interaction. The detection limit of existing refractometers, expressed in refractive index units (RIU), lies typically in a range of $10^{-3} - 10^{-7}$ RIU [9, 13, 158].

Nath et al. [152] propose polymer fiber-based Fresnel refractometer. Its sensing principle is based on attenuated Fresnel reflection from the fiber tip-liquid interface caused by change of refractive index of the surrounding medium. The sensing ability of this measuring principle with a minimal detectable refractive index variation of $2 \cdot 10^{-3}$ RIU is confirmed for a polymer fiber with big core diameter of $105 \mu\text{m}$ and curved end-face. This detection principle is selected for implementation in the EOCB-based demonstrator, because it is simple, robust, and has acceptable accuracy. Here, a tip of a waveguide, integrated into a microfluidic channel or cuvette, is brought in contact with sample fluid. The refractive index of the fluid is determined from the value of back-reflected light power.

In case of a curved fiber or waveguide tips, the multiple total internal reflection of some incident rays at the solid-liquid boundary could be observed. Figure 5.14 b) and c) show a microscopic picture and raytracing results for a waveguide with curved end-face ($r = 25 \mu\text{m}$). Some incident rays propagating in the waveguide are getting back-reflected and return to the entry port of the waveguide. When the refractive index of the surrounding liquid increases to a value at which the condition for total internal reflection is no longer satisfied a sharp decrease of overall reflectivity is observed. This phenomena provides an attractive mechanism for the design of backscattering-based Fresnel-refractometers [13].

^a The materials from co-supervised bachelor project of B.Sc. Henning Bathel [140] are partly used in this section.

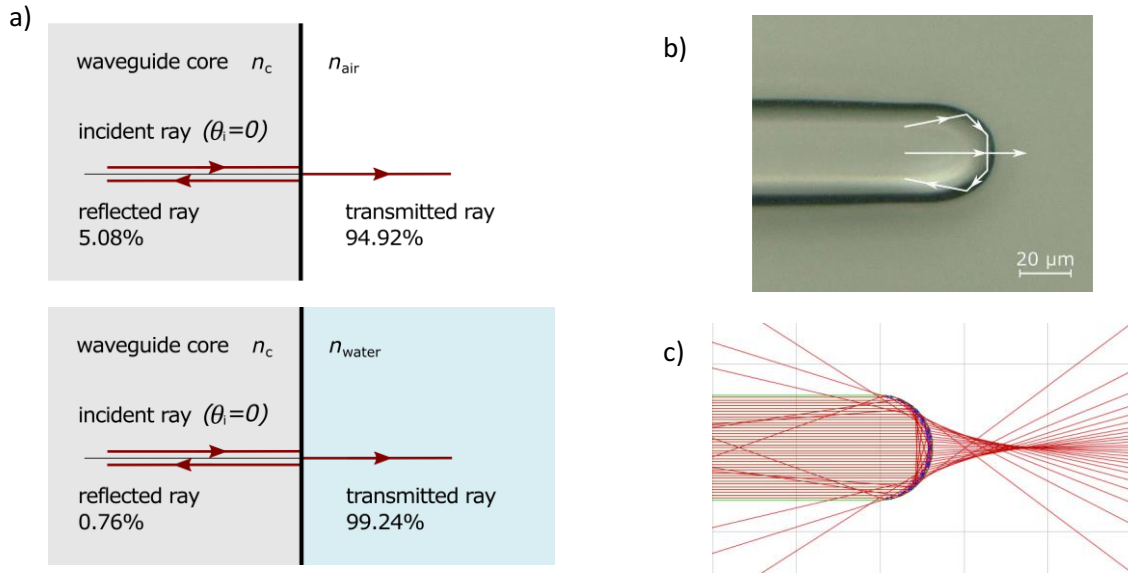


Fig. 5.14: a) Fresnel reflection at the waveguide tip for the case of normal incidence for tip placed in air (above) and in water (below); b) microscopic view of a curved waveguide tip. White arrows schematically demonstrate the back-reflected rays on a curved waveguide end-face; c) ray tracing results for waveguide in air with curved end-face with a radius of curvature of 25 μm .

The fractions of light powers that are reflected and transmitted at the boundary can be calculated according to Fresnel equations (2.8) and correlate with the refractive index of the liquid medium. Fig. 5.14a) illustrates the case of normal light incidence ($\theta_i = 0$) at a waveguide end-face made of EpoCore with refractive index $n_c = 1.5834$ in air and in water. Calculations for other surrounding fluids used for sensor evaluation are given in Table 5.1.

Table 5.1: Ratio of reflected light power in case of normal light incidence at EpoCore waveguide tip with refractive index $n_c = 1.5834$ depending on the refractive index of surrounding medium.

Surrounding medium	Refractive indices at $\lambda = 850 \text{ nm}$ and room temperature [150]	Fraction of reflected power, R [%]	Fraction of reflected power normalized to air, $R_{\text{fluid}}/R_{\text{air}}$
air	1.0002	5.08	1
water	1.3290	0.76	0.15
ethylene glycol	1.4255	0.27	0.05
glycerin	1.4656	0.13	0.02

An in-plane, EOCB-based implementation of this sensing principle seems promising, as it allows refractive index monitoring in addition to turbidity and concentration measurements of simple solutions in one single miniaturized platform. In this way, the non-invasive and label-free optical sensing could be implemented. The fabrication of basic optical elements, such as straight waveguides, Y-splitters, combiners, and curved and flat waveguide end-faces, required for EOCB implementation of this sensor, has been successfully demonstrated previously in this thesis. Therefore, the fabrication of polymer-based refractometer should be within reach.

5.3.1 Fiber-Based Implementation of Fresnel-Refractometer

In this section, a reflection-based refractometry is firstly performed using conventional GIF50C multi-mode glass fibers with cleaved (flat) and curved end-faces, see Fig. 5.15. The assumption behind the use of curved fiber tips is that more light can be totally reflected at the curved interface, as it is shown in Fig. 5.14 c), and thus a higher sensor output signal should be observable.

The curved fiber tip is obtained in a laboratory environment using a fiber fusion splicer BFS-60 (BIT Communications^a) inside which the cleaned and cleaved tip of a stripped multi-mode glass fiber is locally melted by an electric arc. Due to the surface tension of glass, a spherical surface is formed on the fiber tip. During the reflow process, the glass materials of core and cladding probably become blended. Therefore, the exact refractive index of the tip is not known and lies between the refractive index of core n_c and cladding n_{cl} . The radius of the tip's curvature can be approximately adjusted by controlling the fusion current and time. The fiber, with a curved tip with a radius of curvature of $140\ \mu\text{m}$ (Fig. 5.15, right), is used for sensor evaluation experiments.

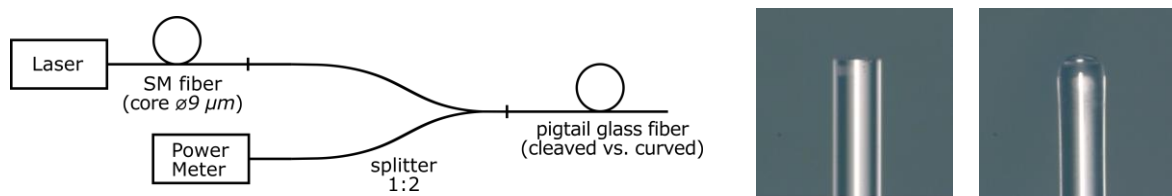


Fig. 5.15: (Left) Optical setup for fiber-based back Fresnel-refractometer testing: light source (laser diode) with ACP/PC single-mode fiber, beam splitter, pigtail fiber tip and power meter; (center) glass fiber tips used in refractometer setup: cleaved multi-mode fiber and (right) curved single-mode fiber with radius of approximately $104\ \mu\text{m}$.

The pigtail flat (cleaved) fibers are plugged into the measurement circuit according to the scheme presented in Fig. 5.15 (left). Testing is performed using an infrared laser diode WWG OLS-15 at wavelengths of $1310/1550\ \text{nm}$. This fiber-coupled laser has an output power of $-7\ \text{dBm}^b / 0.2\ \text{mW}$.

The choice for this light source is determined by availability of components such as pigtailed fibers and 1:2 splitters, designed for the telecomm wavelengths 1310 and $1550\ \text{nm}$. The reflection loss at the fiber-fluid interface is measured by means of a power meter ML93B (Anritsu Corp.) connected to an optical power sensor MA96A (Ge photo diode). The dark-current level (lower measurement limit) of the power sensor at $\lambda = 1310\ \text{nm}$ is $-80\ \text{dBm}$, which corresponds to an absolute power of $10\ \text{pW}$.

The fiber tip is subsequently immersed into sample fluids, performing 15 measurements for each liquid. In order to minimize the uncertainty in measurements, the fiber tip is cleaned in DI-water and in isopropanol (IPA) between all measurements. As sample fluids serve as standard fluids for refractive index analysis: air, water, ethylene glycol, and glycerin with refractive indices of $n = 1.0002, 1.3223, 1.4214,$ and $1.4631,$ respectively (at $\lambda = 1310\ \text{nm}$ and at room temperature) [150].

The ratios of reflected light power in air P_{air} and in the fluid P_{fluid} to the incident light power P_i can be obtained from Fresnel equations (2.6) and (2.8), R_{air} and R_{fluid} , respectively. For a conventional

^a Research group of Prof. Dr. Fedor Mitschke "Nonlinear Optics", Institute of Physics, University of Rostock

^b Decibel Milliwatt (dBm) is the power level in decibels, referred to $1\ \text{mW}$, i.e. $P[\text{dBm}] = 10 \log_{10} \frac{P[\text{mW}]}{1\ \text{mW}}$

multi-mode glass fiber (MMF), a theoretical dependence of the reflected power $P_{\text{fluid_MMF}}$ normalized to the reflected power in air P_{air} on refractive index of the fluid n_{fluid} takes the form:

$$\begin{aligned} \frac{P_{\text{fluid_MMF}}}{P_{\text{air_MMF}}}(n_{\text{fluid}}) &= \frac{P_{\text{fluid_MMF}}}{P_i} \frac{P_i}{P_{\text{air_MMF}}} = \frac{R_{\text{fluid_MMF}}}{R_{\text{air_MMF}}} = \\ &= \left| \frac{n_{\text{fluid}} - n_{\text{glass}}}{n_{\text{fluid}} + n_{\text{glass}}} \right|^2 \bigg/ \left| \frac{n_{\text{air}} - n_{\text{glass}}}{n_{\text{air}} + n_{\text{glass}}} \right|^2 \approx \left| \frac{n_{\text{fluid}} - 1.4468}{n_{\text{fluid}} + 1.4468} \right|^2 / 0.0333, \end{aligned} \quad (5.2)$$

where $n_{\text{glass}} = 1.4468$ [150] is the refractive index of the glass fiber core made of fused silica at $\lambda = 1310$ nm and n_{fluid} is the refractive index of the surrounding fluid at $\lambda = 1310$ nm. The normalized reflected powers and fitted function according to (5.2) obtained for flat and curved fiber tips are graphically presented in Fig. 5.16. The power reflected at the flat fiber-air interface is -31.79 ± 0.02 dBm, giving a measurement range of approximately 48 dB. The detailed experimental results can be found in Table 8.3 and Table 8.4 in the Appendix of this thesis.

For waveguides with flat end-faces, a better agreement with the theoretical value (5.2) predicted by Fresnel-equations is observed. However, an approximately nine times higher normalized output signal is measured with the curved fiber tip for fluids with refractive index of approximately 1.4, while showing a similar dependence trend. Thus, the assumption stated at the beginning of this section about higher signal level for curved fiber tip could be partly confirmed.

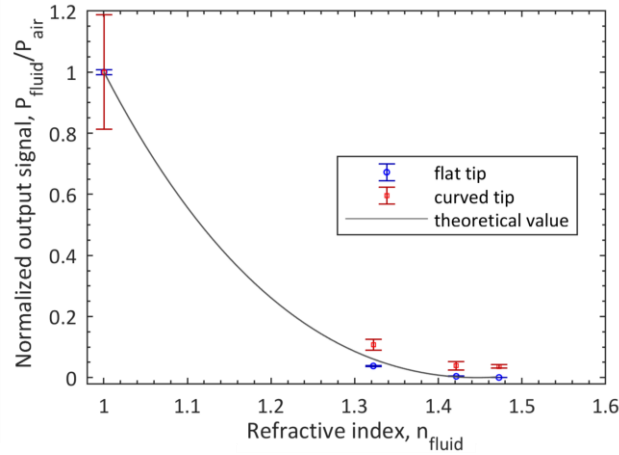


Fig. 5.16: Measured back-reflected power by experiments with different glass fiber types: flat (cleaved) and curved tip; measured powers are normalized to the back-reflected power in air.

5.3.2 Design of EOCB-Based Fresnel-Refractometer

The back-reflection-based refractive index measurement principle approved on glass fibers is implemented as a miniaturized polymer-based platform on EOCB. The evaluation performed at a wavelength of $\lambda = 850$ nm due to known and acceptable optical losses for EpoCore/EpoClad multi-mode waveguides with cross-section of $50 \times 50 \mu\text{m}^2$. The optical layout of this three layer polymer platform is shown in Fig. 5.17. The optical combiners, placed in an open fluidic cuvette, consist of three parts: (1) straight section (length of 3 mm) for stabilization of mode mismatch between coupling glass fiber and polymer waveguide, (2) 2:1 combiner, and (3) another straight section with curved or flat tip (3 mm).

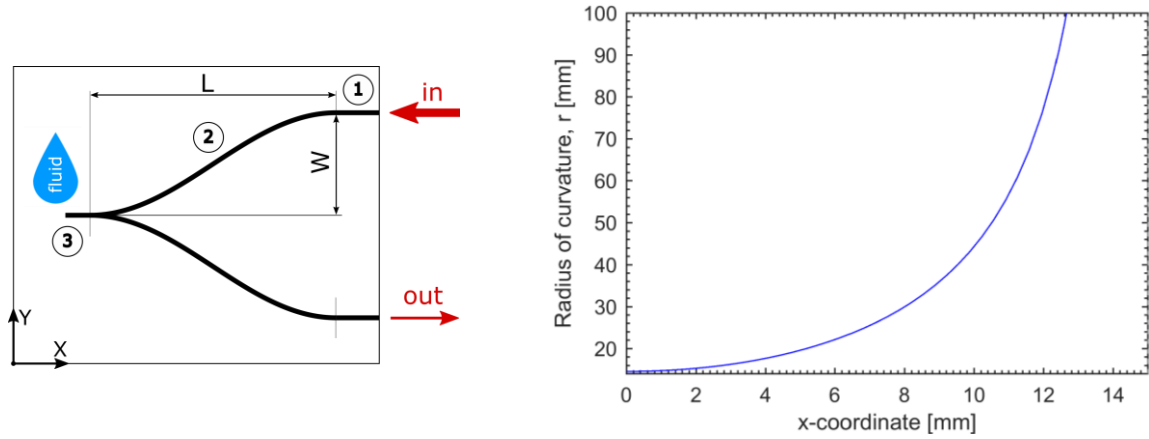


Fig. 5.17: Left) Schematic representation of optical layout of a back-reflection sensor consisting of two straight sections (1), (3) and an optical combiner (2) following the cosine function $f(x) = W/2 \cos(x \pi/L)$; (right) the change of radius of curvature along the cosine function (5.3) in its quarter-period depending on x -coordinate.

For minimization of bending losses in bent regions of the combiner and making the design more compact, the cosine function is preferred over two circular segments with constant curvature. The arms of the combiner follow the half-period of a cosine function $f(x) = W/2 \cos(x \pi/L) = 25/4 \cos(x \pi/30)$ with width W and length L , see Fig. 5.17 (left).

In case of cosine-function, the curvature r changes along the pathway and, for each coordinate x , it can be calculated according to the following rule [179] (see Fig. 5.17, right):

$$r = \frac{[1+(f'(x))^2]^{3/2}}{|f''(x)|} \quad (5.3)$$

The smallest radii of curvature occur at the beginning or end of the cosine section. There they take the value of 14.59 mm, which lies above the critical value of 6 mm (determined in section 4.1.3) under which the bending losses rise sharply. In order to estimate the bending losses in cosine-shaped waveguide sections, an approximation is necessary, because the bending losses are previously determined for circular arcs with constant curvature (see section 4.1.3). The bending losses are calculated using formula (5.3) and the experimentally obtained rule (4.3) by means of numerical integration. The total bending loss incurred in one arm of the cosine combiner V_{BL_arm} is estimated as:

$$V_{BL_arm} \approx -0.69 \text{ dB} \quad (5.4)$$

Due to the fact that there are two symmetric combiners on the input and output side, total bending loss in the combiner V_{BL} is twice the value of the bending loss incurred in one arm, i.e. $V_{BL} = 2 V_{BL_arm} = 2 \cdot (-0.69 \text{ dB}) = -1.38 \text{ dB}$.

From the CAD-file of the optical design, the total length of the guiding structure between the in- and output is estimated to be 8.4 cm, i.e. the length-dependent propagation losses determined in section 4.1.1 for this EpoCore/EpoClad multi-mode waveguide configuration amount to $V_{PL} = 8.4 \text{ cm} \cdot (-0.59 \text{ dB/cm}) = -4.96 \text{ dB}$. In section 4.1.1, the average coupling loss is found to be $V_{CL} = -0.17 \text{ dB}$.

The sensor operation is based on Fresnel reflection, therefore, in addition to the already explained losses, the reflection loss V_{RL} should be considered. According to the calculations of the reflection

coefficient given in Table 5.1, in the case of air as a test medium, only 5.08% of the light power will be back-reflected from the waveguide-fluid boundary, i.e. considering the rule (2.19), $V_{RL} = -12.94$ dB.

The optical waveguide of the sensor forms a 1:2 splitter, i.e. only 50% of the optical power back-reflected from the waveguide end-face is guided to the output of the sensor. Therefore, the optical losses at an ideal 1:2 splitter take the value of $V_{splitter} = -3.01$ dB.

Therefore, the total insertion loss V_{IL} consists of coupling losses, propagation losses, bending losses, reflection losses, and losses at the splitter:

$$V_{IL} = V_{CL} + V_{PL} + V_{BL} + V_{RL} + V_{splitter} \quad (5.5)$$

Assuming this and the considerations above, the theoretically estimated total insertion loss in sensor placed in air as test medium is:

$$V_{IL} = -2 \cdot 0.17 \text{ dB} - 4.96 \text{ dB} - 1.38 \text{ dB} - 12.94 \text{ dB} - 3.01 \text{ dB} \approx -22.63 \text{ dB} \quad (5.6)$$

This value does not include the mode-mismatch losses, splitting loss in taper, and losses due to possible non-symmetry of the splitter's arms and additional impurity in the waveguides. Therefore, the real losses can differ from this estimated value.

5.3.3 Sensor Performance and Influence of Waveguide's Tip Shape

The performance of polymer EOCB-based refractometers with different waveguide end-faces is compared experimentally. Two identical 2:1 optical combiners with curved end-faces are laser-written on the same FR-4 substrate. The curved end-face of the cladding-less sensor tip is caused by the laser spot diameter, while the flat end-face is obtained by the subsequent planar polishing of the fabricated curved tip.

The evaluation setup consisting of a light source, detector unit, fabricated optical board, coupling glass fibers (single-mode SMF-28 at input and multi-mode M43L05 at output), and two 3-axis flexure stages MicroBlock™ MBT616D/M (Thorlabs, Inc.) with a tilt module for glass fiber alignment is shown in Fig. 5.18. A Fabry-Pérot laser diode FOSS-21-3S-5/125-850-S-1 (OZ optics Ltd.) with a central wavelength of $\lambda = 850 \pm 15$ nm [180] serves as a light source. The light power back-reflected at the waveguide-fluid interface is measured by a power meter ML93B (Anritsu Corp.) with a measuring head MA95A (silicon photo diode). The output power of the fiber coupled laser is -0.34 dBm, i.e. 0.926 mW. The dark-current level (lower measurement limit) of the power meter at the wavelength of $\lambda = 850$ nm is -90 dBm, this corresponds to an absolute power of 10 pW.

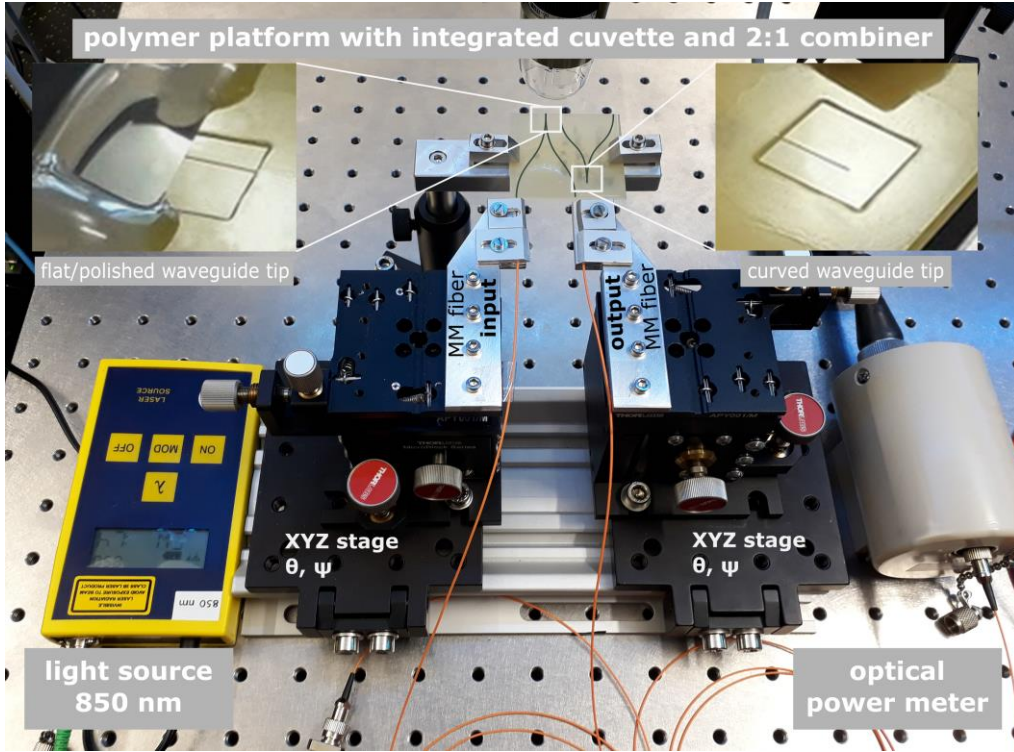


Fig. 5.18: Setup for EOCB-based Fresnel-refractometer evaluation.

As in the case of the fiber-based refractometer, the set of fluids, such as air, water, ethylene glycol and glycerin with RIs of $n = 1.0002, 1.3290, 1.4255,$ and 1.4656 , respectively (at $\lambda = 850$ nm and at room temperature), is employed for evaluation of the EOCB-based refractometer.

For an EpoCore waveguide with refractive index $n_c = 1.5834$, a theoretical dependence of the power reflected at the end-face $P_{\text{fluid_EpoCore}}$ normalized to the reflected power in air P_{air} on refractive index of the fluid n_{fluid} can be obtained from Fresnel equations (2.6), (2.8) and takes the following form:

$$\frac{P_{\text{fluid_EpoCore}}}{P_{\text{air_EpoCore}}}(n_{\text{fluid}}) = \frac{R_{\text{fluid_EpoCore}}}{R_{\text{air_EpoCore}}} = \frac{|n_{\text{fluid}} - n_c|^2}{|n_{\text{fluid}} + n_c|^2} \bigg/ \frac{|n_{\text{air}} - n_c|^2}{|n_{\text{air}} + n_c|^2} \approx \frac{|n_{\text{fluid}} - 1.5834|^2}{|n_{\text{fluid}} + 1.5834|^2} / 0.051, \quad (5.7)$$

The measurement in air using the waveguide with a curved end-face gives a value of -48.2 ± 0.15 dBm. This means that the range available for the measurement is limited to 41.8 dB.

Figure 5.19 gives the readings of the EOCB-based sensor with integrated polymer waveguides with flat and curved end-faces. From the measured values, it becomes clear that for fluids with $n > 1.4$, the sensitivity of the sensor decreases sharply, while the predicted output signal magnitude lies within the signal fluctuation range. Thus, the sensor unit in its current implementation is not suitable for measurements of substances with $n > 1.4$.

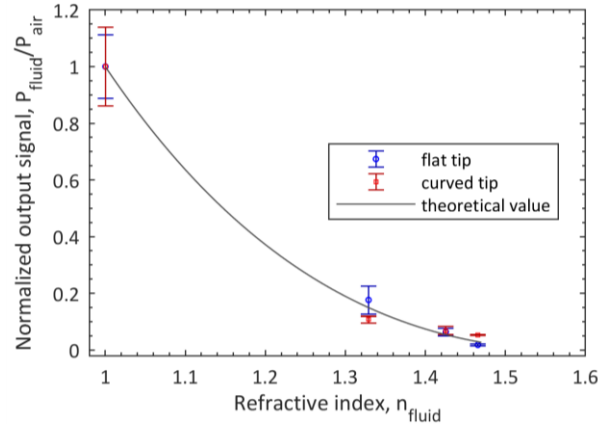


Fig. 5.19: Readings of polymer-based sensor with integrated waveguides with curved and flat end-face. Reflected powers measured in fluids P_{fluid} are normalized to the reflected power P_{air} obtained in air.

These experiments confirm the performance capability of the fabricated EOCB-based Fresnel-refractometer for measurements of RIs in a range of $1 \leq n < 1.4$ with the smallest measurable variation of $\Delta n \approx 1.6 \cdot 10^{-2}$ RIU. For waveguides with flat end-faces, a better agreement with the theoretical value (5.7), as predicted by Fresnel-equations, is observed. For both end-face configurations, the comparable normalized output signals are measured. However, measurements with waveguides with flat end-face show a time-dependent fluctuation of the output signal. It remains unclear, what causes this signal instability. It might be either changes in the optofluidic platform, such as diffusion of the fluids into polymer structures and temperature fluctuations due to evaporation, or changes in measurement equipment caused by fluctuations in the power-controlled laser due to back-reflected light, or a combination of both. Therefore, this sensor performance strongly depends on the equipment used, namely resolution of the power meter and stability of the light source.

Advantages of this method are device miniaturization, small required amount of sample fluid together with simple design, measurement procedure, and post-data analysis. Despite these advantages, low detection limit and signal instability are the drawbacks of this sensor unit. This EOCB-based optofluidic platform still requires bulky equipment, such as a coupling system, a powerful light source, and a highly sensitive detector unit, for appropriate operation. The use of more stable light sources in constant environmental conditions may lead to higher stability of the output signal. Another way to improve the performance is to increase the output signal, e.g. by reduction of the optical losses in an improved optical combiner design, by use of larger waveguide cores and more powerful light sources. Moisture protective conformal coatings, e.g. parylene [181], may protect the sensor tip from the undesired fluid penetration.

5.4 Mach-Zehnder Interferometers on EOCBs

In this section, the concept of polymer-based Mach-Zehnder interferometers (MZIs) on EOCB is presented for fluidic sensing applications and for thermo-optic attenuation of the light signal.

5.4.1 Mach-Zehnder Interferometer-based Refractometer

In fluid sensing, the use of Mach-Zehnder interferometers as compact refractometers for biosensing is reported in [159, 182, 183]. The classical MZI-based refractometer consists of two branches

originating from a Y-splitter and recombined in a second Y-coupler. One of the interferometer arms is implemented cladding-less and is thus sensitive to refractive index changes of the surrounding medium. The latter are referred to as the sensor arm, while the other path is isolated from the environment and serves as the reference arm [182, 184], see Fig. 5.20 (right). Replacement of the medium, surrounding the sensing arm, leads to a change in the effective refractive index of the guided mode and therefore to a phase shift φ with respect to the light wave propagating in the reference arm [159]:

$$\varphi = \frac{2\pi}{\lambda} \Delta n_{\text{eff}} L, \quad (5.8)$$

where Δn_{eff} is the induced difference between effective refractive indices of sensor and reference arms, L is length of the interaction region, and λ is the operation wavelength. Depending on the phase shift, electromagnetic waves from two MZI-arms may interfere constructively (2π -phase shift) or destructively (π -phase shift), see Fig. 5.20 (left). Due to this interference, the light intensity at the output of the device I_{output} varies as:

$$I_{\text{output}} = I_S + I_R + 2\sqrt{I_S I_R} \cos \varphi, \quad (5.9)$$

where I_S and I_R are the intensities in sensing and reference arms, respectively. From the intensity variation at the output of the MZI, the refractive index of the fluid surrounding the sensor arm can be determined, see Fig. 5.20 (left).

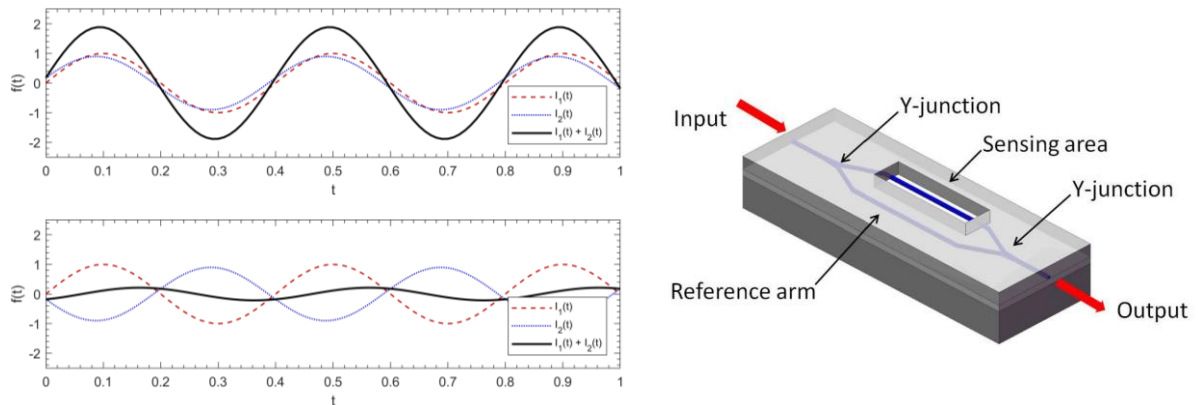


Fig. 5.20: (Left) Constructive (above) and destructive (below) interference (black curve) of two signals (red and blue curves); (right) schematic representation of a MZI consisting of two symmetric Y-splitters with sensing and reference arms [184].

5.4.2 Thermo-optic Effect in Polymer MZI-based Tunable Attenuator

The thermo-optic effect represents the dependence of the refractive index n on temperature T . When compared with glass or silicon, polymers have larger thermo-optic coefficients, e.g. $dn/dT = (-7.1 \pm 0.4) \cdot 10^{-5} \text{ K}^{-1}$ for EpoCore [85]. The thermo-optic effect is a well-pronounced phenomenon in polymeric structures, which can cause a phase shift between the MZI-arms and thus can be used for thermo-optic modulation of the light power [133]. The feasibility of thermo-optic light attenuator on EOCBs is tested in this section.

Here, one of the interferometer arms is heated while the other is kept at room temperature. The temperature gradient ΔT results in a change of refractive index and accordingly in a phase difference between two electromagnetic waves φ_n calculated as follows [52]:

$$\varphi_n = \frac{2\pi L}{\lambda} \frac{dn}{dT} \Delta T, \quad (5.10)$$

where λ is the wavelength of light and L is the length of the heated region. The temperature that causes the phase shift of $\varphi_n = \pi$ is then calculated as follows:

$$\Delta T = \frac{\lambda}{2L} \left(1 / \frac{dn}{dT}\right) \quad (5.11)$$

For example, in case of 6 mm long EpoCore waveguide operating at a wavelength of $\lambda = 850$ nm, the necessary temperature change between two MZI branches to cause destructive interference (phase shift $\varphi = \pi$) is $\Delta T \approx 1$ K.

In relation (5.11), it is assumed that the length of the heated region L remains constant. However, it varies with temperature by ΔL due to its thermal expansion. This value can be estimated from the thermo-mechanical simulation using FEM software COMSOL Multiphysics. The linear expansion of a 28.07 mm long waveguide is about $\Delta L = 1.45$ nm (simulation input parameters: EpoCore waveguide attached to a 50 μm thick EpoClad layer fixed on a 1.5 mm thick FR-4 substrate, a homogeneous temperature distribution of $T_{\text{env}} = 25.6$ °C over the simulation area of 50×50 mm² and a temperature increase of $\Delta T = 1$ K over heated region with the length of 6 mm). This causes an additional phase shift φ_{TE} , which can be calculated as $\varphi_{\text{TE}} = \frac{2\Delta L}{\lambda} \pi$ and at a wavelength $\lambda = 850$ nm is around $\varphi_{\text{TE}} = 0.0034 \pi$. This value is more than three orders of magnitude below the phase shift $\varphi_n = \pi$ caused by the thermo-optic effect and can thus be neglected.

Design of MZI-based Thermo-optic Light Attenuator

This working principle is tested on the EOCB-based interferometric light attenuator, which is an all-polymer multilayer platform consisting of an integrated copper heater in a meandering shape and two symmetric Y-splitters. The shape of the Y-splitters follows the cosine-function $f(x) = 1.5 \cos(\pi x/10)$ as shown in the inset in the upper right corner of Fig. 5.21.

On this platform, ridge waveguides with a core size of 3.5×6 μm^2 made of EpoCore / EpoClad material combination operate in few-mode regime at the wavelength of $\lambda = 850$ nm. According to the calculations performed with an open-access mode solver [57], at this wavelength, this waveguide core can support four light modes TEM_{00} , TEM_{01} , TEM_{10} , and TEM_{02} (see section 4.4). Each of these modes or their superposition can be excited depending on the launch conditions. However, the most clearly observed and stable mode is the TEM_{01} , see light intensity distribution obtained by CMOS chip in the left inset in Fig. 5.21. This mode is selected for testing.

Temperature Distribution over MZI Branches

Due to the fact that the exact temperature difference between the two interferometer arms is decisive for signal interference, the temperature distribution over the two MZI arms should be investigated.

On the EOCB platform, the heating is performed by an integrated copper thin-film heater in a meandering shape. It has a thickness of 5 μm , occupies the area 2×7 mm², and is placed straight

under one of the MZI arms (see inset in the center in Fig. 5.21). The electrical resistance of the heater, experimentally determined using a 4-wire sensing, is $R_m = 2.08 \Omega$ at a temperature of $T_{env} = 25.6 \text{ }^\circ\text{C}$. The heater operates with a heating power of $P \approx 83 \text{ mW}$ at constant current set to 200 mA, which leads to a temperature increase of approximately $4 \text{ }^\circ\text{C}$.

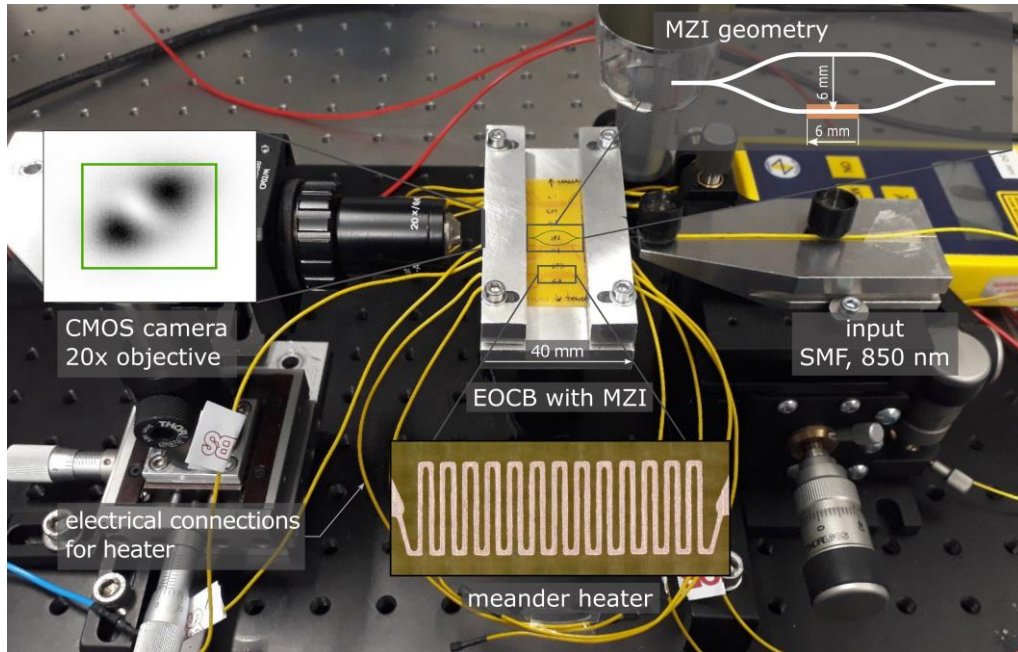


Fig. 5.21: Setup for evaluation of MZI attenuator performance: EOCB platform, CMOS camera, SM coupling fiber, light source (laser diode with central wavelength of $\lambda = 850 \text{ nm}$), and a flexure stage with a tilt module. Insets: MZI geometry and dimensions; copper thin-film heater in meandering shape; TEM_{01} mode at the MZI output at room temperature, green rectangle represents cross-sectional dimension of a waveguide.

Thermal FEM simulation using ANSYS Multiphysics is performed for determination of temperature gradient over the EOCB board. Simulation results are compared with experimental results obtained with a thermographic camera testo 882 (Testo SE & Co. KGaA). Both approaches show strong exponential temperature decay. Consequently, the distance of 6 mm between two MZI-arms is sufficiently large for the temperature of the reference arm to remain at room temperature (see Fig. 5.22).

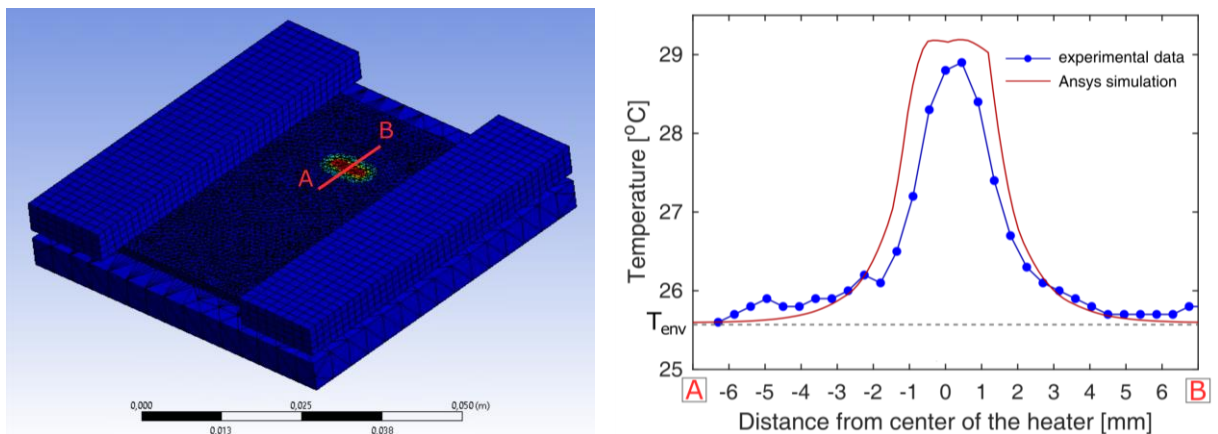


Fig. 5.22: Thermal FEM simulation confirming experimental results obtained using thermographic camera: temperature gradient over the distance of 14 mm (AB).

Performance of MZI-based Attenuator on EOCB

The evaluation of the MZI-based light attenuator is performed using the setup shown in Fig. 5.21. It consists of the fabricated EOCB-based optical platform, a microscope objective with 20-fold magnification mounted on the monochromatic Blackfly CMOS camera BFLY-PGE-50A2M-CS with pixel size of $2.2 \mu\text{m}$ (Point Grey Research Inc.), SM800 coupling fiber with mode field diameter of $4.7 - 6.9 \mu\text{m}$ mounted on a 3-axis flexure stage MicroBlock™ MBT616D/M (Thorlabs, Inc.), and a laser diode FOSS-21-3S-5/125-850-S-1 (OZ optics Ltd.) with a central wavelength of $\lambda = 850 \pm 15 \text{ nm}$ as a light source.

During MZI-based attenuator operation, light modulation can be observed twice: during the heating phase (heater on) and during the subsequent passive cooling phase (heater off). Figure 5.23 shows the output signal obtained with the CMOS camera by integrating of all pixel intensities across the core area (see green rectangle in the inset on the left in Fig. 5.21 and normalized to the MZI output signal at room temperature.

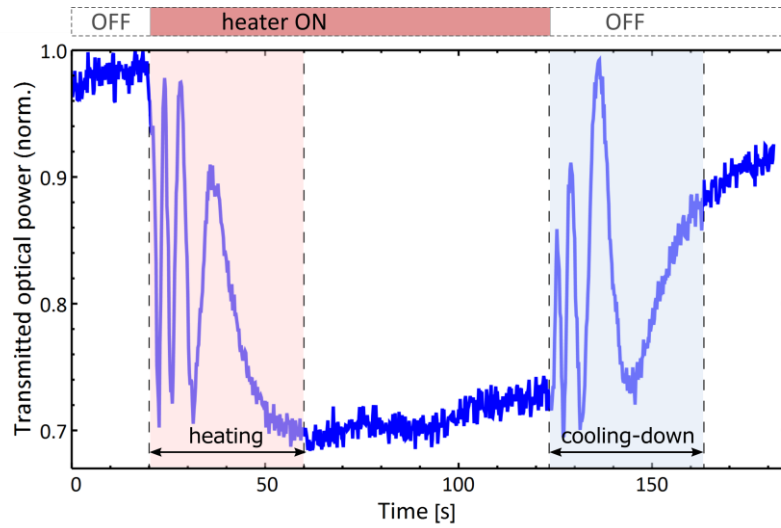


Fig. 5.23: Operation of a MZI-based few-mode light attenuator at the wavelength of $\lambda = 850 \text{ nm}$ with an integrated thin-film meander heater ($P = 83 \text{ mW}$). The bar indicates intervals at which the heater is switched on or turned off.

Recalculation of time axis into the temperature axis is implemented by means of Newton's law of heating or cooling (temperature function-of-time solution in terms of object heat capacity) [185]:

$$T(t) = T_{\infty} - (T_{\infty} - T_0) e^{-t/\tau}, \quad (5.12)$$

where T_0 is the initial temperature of the heater, T_{∞} is the converged heater temperature, and τ is the time constant of the system. The time constant should be thus experimentally estimated for the system. The meander temperature dependence on time can be subsequently recalculated from dependencies of meander resistance on time and temperature.

The relationship between temperature change and heater resistance $R(T)$ can be described by the following linear approximation [186]:

$$R(T) = R_{\text{ref}} [1 + \alpha (T - T_{\text{ref}})], \quad (5.13)$$

where R_{ref} is the resistance at the reference temperature T_{ref} and α is the temperature coefficient of resistance. The temperature coefficient of resistance for the fabricated copper heater should be determined experimentally due to the significant differences in table values depending on alloy composition [187, 188].

The fabricated EOCB platform with meander heater is placed and temperature-controlled on a Peltier element TEC1-127060 connected to a TEC-1091 controller (Meerstetter Engineering GmbH). The resistance of the thin-film copper heater is determined by means of 4-wires sensing and plotted over the temperatures (see Fig. 5.24). The temperature coefficient of resistance for copper of $\alpha = 3.82 \cdot 10^{-3} \text{ K}^{-1}$ is obtained from the linear fit $R(T) = 1.9354 + 0.0074 T$.

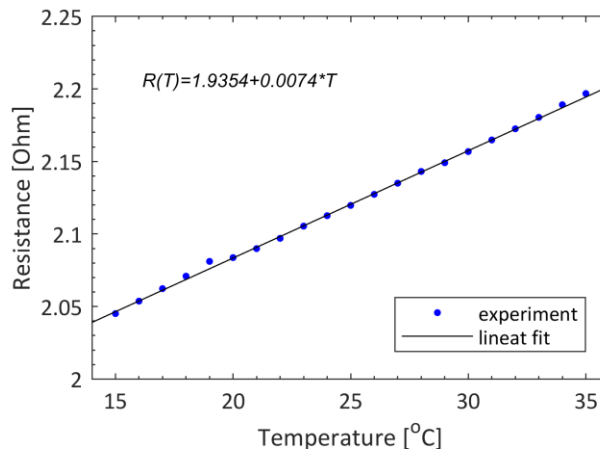


Fig. 5.24: Dependence of resistance of thin-film copper heater on temperature obtained using a Peltier element and 4-wires sensing.

Using the 4-wires sensing, the temporal change of the heater resistance $R(t)$ at a constant current of $I = 50 \text{ mA}$ is measured using a sourcemeter Keithley 2400 (see Fig. 5.25). At this current the resistance converges exponentially (see Fig. 5.25, left) to a value of $R_{\infty} = 2.132 \Omega$. The resistance change over the time can be fitted by the following function:

$$R(t) = 2.1325 - 0.0082 e^{-0.0305 t} \quad (5.14)$$

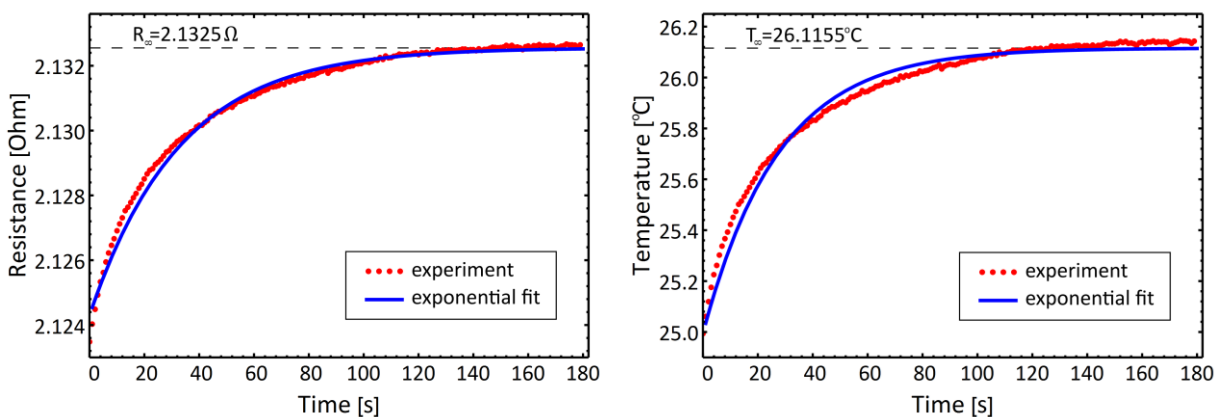


Fig. 5.25: (Left) Experimental results and exponential dependence of the meander resistivity on time; (right) calculation of the meander temperature dependence on time according to the rule (5.13) and exponential fit.

Using (5.13), (5.14) and estimated values of temperature coefficient of resistance, the heater temperature dependence on time takes the following form, see Fig. 5.25 (right):

$$T(t) = 26.1155 - 1.1218 e^{-0.0365 t} \quad (5.15)$$

Considering equation (5.15), the time constant of the system dominated by thermal conductivities of the EpoCore and EpoClad [133] takes the value of $\tau = 0.0365 \text{ s}^{-1}$. Therefore, the temperature dependence of the MZI signal during heating and cooling phases (see colored regions in Fig. 5.23) could be obtained. These results confirm the calculations performed at the beginning of this section related to destructive interference of light from two MZI branches with the temperature gradient of $\Delta T \approx 1 \text{ K}$ between two MZI branches (see Fig. 5.26).

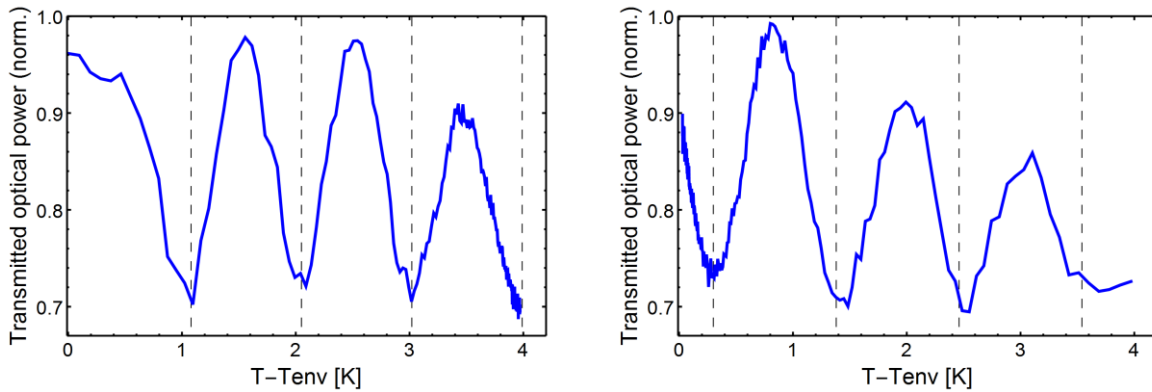


Fig. 5.26: Signal modulation on output of the MZI attenuator depending on the temperature difference $\Delta T = T - T_{env}$ in two MZI branches in the same cycle: (left) by heating and (right) by cooling down.

The light power modulation depth of an interferometric attenuator depends on many factors, such as bandwidth of the light source, geometric symmetry of the 1:2 splitter, number of supported modes, mode dispersion in a waveguide, light polarization and its maintenance within the setup. For the presented setup, a light power modulation depth of 30% is demonstrated. The single-mode operation regime is essential for unambiguous operation of an interferometer [159]. The higher-order propagating modes lead to the degradation of the modulation depth. Single-mode operation can be achieved with this optical board by the use of a longer-wavelength light source, e.g. at $\lambda = 1310 \text{ nm}$. In this experiment, light with the wavelength $\lambda = 850 \text{ nm}$ is used due to the sensitivity of the camera's silicon image sensor MT9P031 in the NIR region. Better power modulation may be achieved at higher heater temperatures, due to reduced sensitivity of the setup to small environmental temperature fluctuations.

The performance of single-mode interferometric devices is also polarization-sensitive. In this experiment, the polarization of incident laser light and its maintenance along the waveguide are not considered due to the lack of measurement equipment and project time. The maintenance of linear polarization can be hindered by differences in effective refractive indices in lateral and transversal directions due to rectangular geometry of fabricated waveguides. It can be improved using square waveguides with a critical edge length a_c calculated according to the single-mode criterion (2.15) [189].

This MZI-based demonstrator shows the feasibility of EOCB-implementation and can be applicable for fluid sensing, mode multiplexing, light phase and power modulation, or as a thermo-optic switch. However, this concept is difficult to implement fully on an EOCB without any external optical

equipment due to the narrow coupling tolerances of single-mode waveguides. Coupling concepts allowing narrow alignment tolerances and filtering of high-order modes, e.g. using sufficiently long back-to-back tapered multi-mode sections [189], should be implemented.

6 Conclusions and Outlook

The primary goals of this thesis were the establishment and evaluation of a technological process chain for the fabrication of polymer-based optofluidic sensor units with integrated optical waveguides and microfluidic structures on EOCBs. Addressing and answering this objective required arranging for necessary laboratory equipment, extensive experimental work, and establishing multiple measurement techniques. Furthermore, a characterization environment for fabricated optical structures and optofluidic sensor units was designed and assembled. This work builds a solid technological and theoretical basis for further investigations of optical microsystems at the Institute of Electronic Appliances and Circuits, University of Rostock.

This study compiled and advanced the knowledge of state-of-the-art versatile fabrication approaches, technological process optimization, waveguide characterization techniques, integrated optical sensing principles, and EOCBs for on-board optical fluid analysis. The results are made easily accessible and well-structured. In this chapter, the milestones of the study are summarized and discussed; an outlook on advisable future work is described.

6.1 Conclusions

6.1.1 Fabrication

The feasibility of polymer-based waveguides integration into EOCBs was studied. The complete laser direct writing setup was built in-house and characterized for writing of photopolymer-based waveguides on EOCBs. Advantages of this technology are: high flexibility, potential scalability to large substrates, high accuracy of the relative beam-to-substrate positioning, and high precision of fabricated structures. The combination of laser direct writing with mask-based lithography enabled fabrication of various optofluidic devices.

The waveguide and substrate material selection was based on the outcomes of a comprehensive literature study. The technological process chain was established for commercially available photolithographically patternable epoxy resin-based photopolymers, such as EpoCore, SU-8, and EpoClad, on FR-4 and borosilicate glass substrates. Optimization of technological processes in terms of polymer adhesion, exposure, tempering, and post processing was performed.

The influence of substrate material and technological parameters, such as laser intensity profile, size and shape of the focused laser spot, exposure dose, and tempering temperature and profile, on the geometric and optical waveguide properties was investigated in great detail. The optimal exposure parameters were investigated theoretically and experimentally for different polymer thicknesses and waveguide dimensions. The optimal technological process parameters are listed in Table 3.3.

Initially, fabrication was hindered by poor polymer adhesion on different substrates types. This could be overcome by physical and chemical substrate pre-treatment before application of the photoresist. As a result, homogeneous polymer films were spin coated. The fabricated multilayer optical systems withstood abrasive grinding and polishing during the preparation of waveguide end-faces.

Different laser beam shaping concepts were proposed, characterized in terms of laser intensity distribution, and used for fabrication of few- and multi-mode waveguides with curved and flat end-faces. Focusing of a Gaussian beam by the exposure head optics allowed to achieve a minimum laser spot diameter of approximately $8\ \mu\text{m}$, which was used for writing of few-mode waveguides. By using circular and rectangular apertures supplemented in the optical path of the exposure head, nearly homogeneous top-hat like laser intensity profiles with circular and rectangular laser spot geometry could be obtained. The occurrence of a presumably inhomogeneous refractive index distribution within the laser-written waveguide cores, named a "double core" effect, was mitigated by optimization of the tempering process and selection of an appropriate laser intensity profile.

The structuring of polymer-based multi-mode waveguides as well as single- or few-mode waveguides by means of laser direct writing was demonstrated on different substrates, such as FR-4, borosilicate glass, and PMMA. Fabricated multi-mode waveguides, in which multiple hundreds of TEM modes could propagate, had a typical cross-sectional dimension of $50 \times 50\ \mu\text{m}^2$. Further, few-modal operation of optical waveguides with minimum achieved cross-section of $3.5 \times 6\ \mu\text{m}^2$, supporting up to four TEM modes in the near infrared light spectrum, has been verified. Mode estimations obtained from a mode solver showed that these waveguides of smallest achievable dimensions exhibit single-mode behavior for wavelengths above $1.41\ \mu\text{m}$. Their single-mode operation is possible up to the cutoff wavelength of $2.02\ \mu\text{m}$.

Several waveguide geometries, such as straight and bent waveguides, splitters, as well as discontinuous waveguides with curved and flat end-faces were structured by varying the laser intensity profile and laser beam trajectory. The fabricated optical waveguides form basic components of the optofluidic demonstrators.

Recommendations and parameters for post-processing steps and system integration, such as multi-step polishing of waveguide end-faces, light coupling, hermetic sealing of microfluidic channels, and connection to external fluidic units, were also given in this work. The parameters of the multistep polishing process sequence of polymer waveguide end-faces were optimized yielding an optical quality of the surface with a mean roughness of $R_a = 45 \pm 4.1\ \text{nm}$.

Different concepts of optical glass fiber-to-waveguide coupling were suggested and implemented. They included butt-coupling and epoxy gluing of the optical board with conventional glass fibers, self-written waveguides, and photolithographically structured trenches in both cladding layers. Later features served for insertion of glass fibers and their simplified relative alignment to the waveguide end-faces. All of these methods were irreversible and suffered from low reproducibility.

The hermetic sealing of up to 10 mm wide fluidic channels was performed by lamination and subsequent photolithographic structuring of the $62.5\ \mu\text{m}$ thick dry film negative tone photoresist, as used as a solder mask in PCB production. This thin laminate is not as durable and firm when compared to bonded thin glass plates. However, it allowed fast and easy sealing of up to 10 mm wide fluidic channels.

This work demonstrates that the developed technology platform meets a wide range of application-specific requirements. As a proof of technological concept, cost-effective optofluidic lab-on-a-board platforms for physical fluid sensing were fabricated and their sensing performance was analyzed.

6.1.2 Analysis of Optical Waveguides

The optical structures fabricated by means of laser direct writing approach were extensively characterized both optically and mechanically. The investigated parameters were optical losses, spectral absorption, mode behavior, sidewall roughness, and impact of end-face geometry on light focusing and transmission in discontinuous waveguides.

The optical losses were analyzed for multi-mode waveguides with a typical cross-section of $50 \times 50 \mu\text{m}^2$ fabricated on FR-4 substrates. Optical losses caused by internal material absorption and scattering at sidewalls were investigated in visible and infrared light spectra depending on core material and tempering parameters used. For the material combination EpoCore/EpoClad, a strong light absorption of more than 3.55 dB/cm was observed for wavelengths below 600 nm, whereas for red light (625 nm) it was 2.90 dB/cm, and for infrared light (850 nm) was as low as 0.59 dB/cm. The influence of core material on propagation losses was investigated on EpoCore- and SU-8-based waveguides. The SU-8 waveguides have lower optical losses than EpoCore, with propagation loss values of 2.74 dB/cm at 590 nm, 1.57 dB/cm at 625 nm and 0.30 dB/cm at 850 nm. Longer tempering at higher temperatures (in deviation from the standard processing recipe) during the post exposure bake tempering had become necessary. However, this caused an increase in propagation losses to 8.25 dB/cm at 590 nm, 5.15 dB/cm at 625 nm, and 1.18 dB/cm at 850 nm. Yet, the modified post exposure bake is an important step, which ensures a homogeneous refractive index distribution in the laser-written waveguide core. With such relatively high propagation losses in the visible light spectrum, applications of epoxy resin-based optical systems are limited to the near infrared spectral range. The obtained propagation losses in the near infrared light range are consistent with results achieved by other research groups using mask-based lithographic structuring. They are acceptable for short-range signal transfer.

In bent waveguides, which are essential for downscaling the EOCB footprint, propagation losses are accompanied by waveguide geometry-induced bending losses. The bending losses were investigated for an array of multi-mode waveguides bends with a cross-sectional dimension of $50 \times 50 \mu\text{m}^2$, radii of curvature of 1 – 14 mm, and central angle of 90° at a wavelength of 850 nm. By subtracting coupling losses and propagation losses caused by absorption and scattering from the measured insertion losses, the dependence of bending losses $V_B(r)$ on radius of curvature r in 90° EpoCore waveguide bends was determined in exponential form: $V_B(r) = 13.01 e^{0.68-1.01 r}$ [dB/cm]. A critical radius of curvature below which the bending losses become significant was determined. For a typical multi-mode EpoCore/EpoClad waveguide the critical radius of curvature was found to be 6 mm resulting in a bending loss of 2.28 dB/ 90° turn. These experimental results were considered in the optical design of light guiding structures, e.g. in Y-splitters of back-reflection and interferometric demonstrators.

The choice of substrate material determines significantly the sidewall roughness of fabricated optical structures, which in turn impacts on a value of scattering-induced propagation losses. The sidewall roughness was evaluated using an optical laser scanning microscope. Waveguides fabricated on smooth and transparent glass substrates have a mean sidewall roughness of $R_a = 79 \pm 7$ nm, while waveguides fabricated on FR-4 substrates exhibit almost three times larger mean sidewall roughness $R_a = 226 \pm 25$ nm. This attributes to diffuse scattering (speckle patterns) at the FR-4 substrate surface during exposure with focused UV light. To what extent the sidewall roughness affects the propagation losses has not been investigated and should be addressed in future work.

The use of rectangular and circular apertures in the beam path of the exposure head enabled structuring waveguides with flat and curved end-faces. Their shape and size depend on the trajectory, profile, and diameter of the laser beam. The end-face geometry strongly influences light transfer through the gap between two end-faces facing each other. Curved end-faces of polymer waveguides act as cylindrical converging lenses, whose focal length in the horizontal plane depends on the radius of curvature of the curved end-face and on the refractive index of the surrounding fluid. Experimental investigations confirmed that the curvature of the waveguide end-face together with the gap between them can be varied such that light focusing and light transfer by discontinuous waveguides with curved end-faces were improved. Waveguides with curved end-faces showed an optimum coupling at nonzero gap (for end-face curvature of $125\ \mu\text{m}$ the optimal distance was $280\ \mu\text{m}$ in air and $350\ \mu\text{m}$ in water), thereby increasing the light path for absorption-based measurements. In contrast, the flat-ended waveguides require butt-coupling for optimal light transfer and were considered as rectangular diverging light emitting surfaces. Waveguides with curved end-faces also demonstrated a better coupling efficiency compared to flat-end waveguides with the same gap width. Based on these experimental results, curved configuration of discontinuous waveguides was defined as more effective and was utilized in demonstrators for absorption-based spectroscopic measurements.

6.1.3 On-Board Detection: Demonstrators Performance

The feasibility of the established technology and its applicability for fabrication of EOCB-based sensing units has been confirmed by means of four optofluidic demonstrators. From the variety of well-established fiber-based measurement methods, the most suitable for an EOCB-based implementation were selected for implementation. Their functionality was based on free light propagation and absorption in fluid, on absorption of the evanescent field, on partial back-reflection at the waveguide end-face, and on interferometric effects. Design and fabrication of these demonstrators were performed. The evaluation of the sensing performance and achievable sensing range of these demonstrators was carried out.

1. Discontinuous multi-mode waveguides were integrated into an autonomous optofluidic measuring platform exploiting Lambert-Beer's absorption law. This enabled turbidity and concentration measurements on EOCB. A reduction of the footprint down to a few square centimeters and the elimination of external optics were achieved by combination of the optofluidic platform as a separate board with an electrical PCB carrying light sources, detectors, and driver electronics. The demonstrator performance in absorption characterization was tested on food dyes and water mixtures using the integrated red SMD LED ($625\ \text{nm}$) as a light source. A coupling concept to LEDs with wide emission angle using a circular aperture (for selective core illumination) was evaluated as well (total LED power was reduced by about $30\ \text{dB}$ by the aperture) [165]. The detected signal decreased exponentially with the dye concentration. A detection limit of approximately 3% of the dye concentration in water was demonstrated. The high signal amplification of $250 \cdot 10^6$ can be reduced by the use of a more powerful light source in the infrared light range, where the waveguide exhibits lower propagation losses, shorter polymer waveguides with larger cross-sectional dimensions, and more advanced coupling concepts with arranged waveguides.
2. A demonstrator, whose measuring principle is based on the wavelength-specific absorption of the evanescent field in a liquid under test, was implemented using continuous optical waveguides. The waveguides, which were manufactured without an upper cladding layer, were placed into a

microchannel filled with a sample fluid. The sample fluid serves as the upper waveguide cladding. According to performed finite element analysis, the bent waveguides with small radii of curvature (< 6 mm) have a greater penetration depth of the evanescent field. This should be experimentally confirmed in future experiments. Thus, such waveguide bends were selected for integration into the evanescent field-based sensing unit and experimental evaluation. A qualitative signal change could be detected when the dissolved dye color or the refractive indices of the sample fluid was changing. The detected signals (absorbance) of evanescent field spectroscopy, obtained with an EOCB-based sensor, were close to 0.1. These results were compared with transmission spectra obtained using a conventional spectrophotometer. A good agreement between the results of EOCB-based sensor and transmission spectra was demonstrated with consideration of an attenuated total reflection correction algorithm. However, a stable light source and a high-sensitivity detector are required for reliable sensor operation. In order to achieve a better signal-to-noise ratio, a reference path can be introduced into the optical layout enabling relative measurements. The detection performance can be further improved by deposition of several nanometers thin silver or/and gold metal layers for implementation of the surface plasmon resonance sensing principle or by waveguide surface functionalization to restrict the detection to specific molecules.

3. An optical refractometer based on Fresnel reflection of the light at a waveguide end-face was fabricated and evaluated. The fraction of light power back-reflected from the waveguide-fluid boundary depends strongly on the refractive index of the liquid surrounding the waveguide end-face. The refractive index was determined by measuring the back-reflected light power. Refractive indices in the range of 1 – 1.4 could be measured with a resolution of $1.6 \cdot 10^{-2}$ RIU. Although, the achieved measuring accuracy of this demonstrator is lower than the resolution of 10^{-5} – 10^{-7} of recently published refractometers, this measurement concept is well suited for fast on-board refractive index determination in a compact form due to its easy implementation and small footprint. Sensing performance can be improved by increasing and stabilizing the optical output signal. This can be achieved by reduction of the optical losses in an improved optical design, by use of larger waveguide cores and more powerful light sources. This shall be accomplished by maintaining constant environmental conditions, such as temperature control of the optofluidic platform and protecting the sensing area from ambient light.

4. The Mach-Zehnder interferometer provided a basis for an EOCB-based interferometric optical power attenuator/modulator. It consisted of waveguides manufactured in the form of two successive Y-splitters with waveguides having a cross-sectional dimension of $3.5 \times 6 \mu\text{m}^2$. These waveguides operated in the few-mode regime guiding four TEM modes at the wavelength of 850 nm. A copper thin film structure in a meandering shape served as a heater. Here, the thermo-optic effect, which is strongly pronounced in polymers, was exploited for light modulation. One interferometer arm was heated; the changing refractive index led to a phase shift for light propagating in the heated arm. This caused destructive or constructive interference at the output of the modulator. A modulation depth of 30% was demonstrated with this setup, which can be further improved by the use of narrow band light sources with a longer wavelength. Since the interferometric setup is polarization sensitive, the use of linear polarized light in combination with polarization-maintaining fibers is essential for optimal performance. The direct EOCB implementation of this demonstrator is challenging due to demanding narrow coupling tolerances to single-mode waveguides, which can be relaxed by implementation of multi-mode tapers. The optical design of the

presented thermo-optic modulator should be proven in future work for Mach-Zehnder interferometer-based refractive index sensing on EOCBs.

In conclusion, a solid technological basis for fabrication of EOCB-based optofluidic units was developed and its applicability was demonstrated for a range of optofluidic demonstrators. The demonstrators are suitable for fluid analysis and represent a trade-off between compactness, cost-effectiveness, and performance. The use of open fluidics, i.e. non-sealed microcuvettes, allows the reduction of consumed fluid volume down to a few microliters. Due to the small footprint, almost non-invasive and autonomous fluid measurement devices, e.g. fixed on buoys, self-propelling research vessels or submarines, can be implemented. The integrated measuring platforms presented in this thesis improve the autonomy and compactness of conventional fluidic laboratory instruments and extend the functionality of already existing autonomous lab-on-a-board measuring devices.

6.2 Recommendations and Future Work

In the following, possible directions for further scientific investigations both in process development and design are proposed.

6.2.1 Technological Research Needs

Future work shall address further EOCB system integration by implementation of a passive optical layer as an additional layer of pre-assembled electrical PCB with integrated heating elements, light sources, and optical signal evaluation units. This entails further constructive and technological work. The implementation can be performed by pressing the optical layer into a conventional PCB [2] or by application of polymers on the backside of the PCB using through-board connector slots or optical vias for optical coupling to soldered light sources [6]. Here, prepreg selection (fibers pre-impregnated with a resin serving as a connecting material in PCB production) must be made with regard to temperature and pressure resistance of the used photopolymers. The required pressing process parameters have to be investigated. All necessary design and manufacturing steps including electric PCB manufacturing can be carried out within the Institute of Electronic Appliances and Circuits using already existing equipment.

The evaluation of fabricated EOCBs in their standard use for the short range high speed data transfer should be considered. It is associated with investments in the required analytical equipment. Here, the functionality of optical circuits can be extended by Mach-Zehnder interferometer-based optical attenuators presented in section 5.4; they can be assembled with integrated LEDs as presented in section 5.1.2. For data transfer, the relatively high propagation losses of waveguides fabricated within the scope of this thesis can become critical. The optical losses can be reduced by improved design of optical structures (refer section 6.2.2) and use of other photosensitive materials having less optical losses at typical transmission wavelengths, e.g. Ormocer/Ormocore and Cytop™/Cyclotene™. In this case, the required process parameters should be determined and tested. For future large scale manufacturing, doctor blade process for liquid resist application could be implemented in the technological process chain instead of the currently used spin coating.

The fabricated optofluidic platforms and EOCBs should pass application-specific reliability and environmental tests. According to claimed properties of epoxy-resin based photopolymers, such as high thermal stability up to 230 °C and glass transition temperature $T_g > 180$ °C [79, 102], the fabricated polymer structures should pass conventional PCB tests. In this study, neither damp-heat

nor thermal cycling tests were performed and should thus be completed in future work according to ISO 9455-17 (85 °C / 85% RH for 168 h) and IPC-TM-650 2.6.7 (100 cycles with temperature fluctuations of -40 °C / 85 °C). These environmental tests should be supplemented by relevant solvent compatibility study. Further research should be focused on evaluation of robustness of fabricated optofluidic systems: their pressure resistance and influence of surrounding temperature on the sensing performance and detection accuracy. These results will be helpful for identifying further possible technological and constructive improvements. Polymer specific aging and degradation of optical performance in harsh environmental conditions and over longer time periods are other aspects that were not investigated in this thesis and should be addressed further.

6.2.2 Constructive Research Needs

Laser Direct Writing Setup

For structuring of single-mode waveguides with dimensional measurements of several micrometers by means of laser direct writing, highly focused laser light is essential. The diameter of the laser beam spot on the photoresist surface becomes critical and can be strongly influenced by fluctuations in substrate thickness and its waviness. The implementation of autofocusing will help to actively compensate the focusing error and should be further embedded into in-house built laser direct writing setup. It can be achieved e.g. with well-established and cost-effective astigmatic lens approach [190] or by extending the exposure head by a semi-transparent and an autofocusing mirrors, which will allow simultaneous laser beam quality and power control.

Computer-controlling of the direct-drive linear stage of the laser direct writing setup should be further optimized: more complex velocity and acceleration profiles could be used for writing of splitters, tapers, and other merging structures in order to obtain more smooth transitions and thus minimize splitting loss.

Design and Optimization of Waveguide Shapes

Optimal routing of optical waveguides is of great importance for efficient light guidance and minimization of optical losses. The shape of the individual waveguide sections, such as cross section, bending radius, and shape of Y-splitter, S-bends, and tapers, has to be optimized in order to increase adjustment tolerances and minimize optical losses. In this thesis, long adiabatic tapers were used in the design of optical splitters as they have lower splitting losses according to Kruse et al. [144]. To further minimize splitting losses in splitters, one of the main components of optical circuits and interferometric devices, the involved taper shape and its length should be optimized further. The optimization of optical waveguide design should be performed with regard to performed experimental results accompanied by optical simulations with help of software tools, such as COMSOL Multiphysics (RF / ray optics / wave optics modules), Zemax, BeamPROP, ModePROP, FIMMPROP etc., and in consideration of other practical design recommendations reported in [191–195]. Numerical simulations can be extended for analysis of fundamental building blocks of integrated optical circuits and to reduce geometry-induced bending losses.

For single-mode bent waveguides and for extremely small radii of curvature it is worth to implement bent structures with an offset [74, 196] or tapers [197] in order to minimize transitional and mode mismatch losses. It can be achieved by compensation of the mode profile shift to the outer waveguide

sidewall occurring due to waveguide bending, as was also confirmed in a master thesis performed at our institute [172].

Light transition between two waveguide end-faces was experimentally investigated (see section 4.3). In order to achieve better light coupling between discontinuous waveguide end-faces, the shaping of curved end-faces or even an integrated lens system as proposed by Watts in [198] should be supported by ray tracing numerical modeling.

Coupling Concepts

Light coupling is one of the major challenges in EOCB production. Optical structures could be coupled to external optical elements or to integrated light sources by means of conventional glass fibers or directly on the EOCB, e.g. using integrated optics, apertures, and deflection elements (mirrors). The implementation of pluggable and low-cost coupling concepts is of particular interest. Such approaches facilitate light coupling and thus drastically reduce the effort for optimal relative waveguide-to-fiber positioning.

The suggested temporary laboratory solution (see section 3.5.2) with glass fibers glued into a U-groove enables stable light coupling but at the same time is bulky, inflexible, and irreversible. There are different concepts of glass fibers integration into a planar photopolymer layer. Concepts of embedding glass fibers in a U-groove structured in the upper or lower cladding layers have already been proposed by many research groups in [134, 135, 199–201]. Some even allow narrow alignment tolerances to single-mode waveguides. Vario-optics AG suggests the use of copper rails on the EOCB surface for passive alignment of glass fibers to polymer waveguide end-faces [83]. Promising configurations for precise passive alignment and fixing of conventional glass fiber by lithographically structured multilayer fiber clamps using a sacrificial layer are given by Guan et al. in [133] and by Liu et al. in [202].

Board-level light coupling remains a major challenge in manufacturing of EOCBs and optofluidic devices, when working towards their autonomous operation. Therefore, more research should be invested into this area. The use of apertures for LED-to-waveguide alignment, as suggested in section 5.3.2, confirmed its feasibility. However, it is bulky and irreversible, since it contains a gluing step. 45° deflection micromirrors placed at the waveguide end-faces can be used for vertical out-of-plane light coupling to VCSELs (vertical-cavity surface-emitting lasers), LEDs, and photodiodes as reported in [2, 203, 204]. Pluggable coupling concepts are of enormous interest for the field of optical communications. Multiple pluggable concepts exploiting pins, alignment marks, and slots have been proposed in [2, 51, 83, 205, 206].

One of these concepts can be adopted for further experiments or an own concept can be developed at the Institute of Electronic Appliances and Circuits. Testing of an appropriate concept in terms of coupling losses, repeatability, and reliability is essential. These couplers should survive thermal cycling, vibration, and other application-specific tests in order to provide long term reliable operation under realistic conditions.

6.2.3 Further Testing Techniques and Device Designs

The application-specific fluidic functionality of EOCB-based optofluidic platforms could be further extended by implementation of microheaters, active and passive mixers, hydrodynamic 2D and 3D flow focusing, and integrated active membrane and passive capillary pumps to perform the on-board

fluid actuation and thus to become independent of external fluidic components, such as syringe pumps, tubings, and fluidic connectors.

Besides optimization of the sensing performance of the four technological demonstrators, suggested in this thesis (according to the recommendations given in chapter 5 and section 6.1.3), the selection of measurement techniques and designs that have a potential to be implemented as a lab-on-a-board sensing platform can be further diversified. This section briefly introduces the most promising candidates that could be implemented during further research activities.

The sensor configuration with discontinuous waveguides with curved end-faces (described in section 5.1) may be used for implementation of a microscale EOCB-based flow cytometer for single cell and DNA analysis. A miniaturized flow cytometer with a complex integrated focusing system was proposed by Watt et al. [18]. Nanoscale optofluidic DNA mapping exploiting nanofocusing by plasmonic antennas was presented by Bayat et al. [207]. This sensor configurations may also be used for UV-Vis spectroscopy of small fluidic sample volumes. However, photosensitive polymers with higher optical transmittance in the wavelength range of 300 – 900 nm are essential for these improvements.

EOCB-based optofluidic sensor systems may be exploited in micro-scale optical analysis of fluid motion. A micro-scale particle image velocimetry (μ PIV) is considered as a promising measurement technique, e.g. Lindken et al. [208] implemented a μ PIV technique for visualization of fluidic flows and fluid velocity measurements in microchannels, Gemmell et al. [209] used μ PIV in context of bio-fluid dynamics for characterization of fluid motion around free-swimming zooplankton and Pitts et al. [210] for characterization of blood flow seeded with fluorescing tracer particles.

Another physical phenomenon, surface plasmon resonance, which can be used for precise refractive index monitoring with resolution of about $10^{-6} - 10^{-7}$ RIU [161], is implementable on EOCB-basis. Low-cost dual LEDs implementation using a metallized Pyrex glass plate was reported by Suzuki et al. in [174] and can be modified for use in a EOCB-based sensor unit.

The large thermo-optic effect and low thermal conductivity of polymers qualify them for on-board thermal tuning and routing of optical signals [88]. Mach-Zehnder interferometer-based structures could perform as thermo-optic mode or wavelength filters, mode-selective switches, and mode converters [87, 88, 133]. Preliminary tests of thermo-optic signal modulation directly on EOCB, as performed in section 5.4.2 of this thesis, confirmed the feasibility of this approach. Further experiments should address optimization of optical circuit design, modulation depth, response time, and switching power.

Neuroscience and optogenetics are emerging research areas. Optogenetics investigates brain activities and neural signaling by optical signal monitoring [211]. Optrodes, which contain optical and electrical elements, are used for light delivery and electrical stimulation of neurons. Different configurations and fabrication techniques have been proposed in [81, 82, 212]. The optrodes should be kept small in order to minimize the impairment of brain tissue by their insertion. The improved light focusing using the curved waveguide end-faces can be advantageous for targeted illumination and thus can find their application in optrodes.

As conclusion, I would like to add that research partners with diverse background and expertise, e.g. from industry, biology, medicine, marine technology, and physics, should be involved into further research activities at the Institute of Electronic Appliances and Circuits to increase the practical relevance of fabricated EOCBs.

7 Bibliography

- [1] A. F. J. Levi, "Optical interconnects in systems," *Proceedings of the IEEE*, vol. 88, no. 6, pp. 750–757, 2000.
- [2] J. Dingeldein *et al.*, "Optical-electrical printed wiring board for high-speed computing applications," *Optical Engineering*, vol. 52, no. 3, 035201(1)-035201(7), 2013.
- [3] H. Ma, A.K.-Y. Jen, and L. R. Dalton, "Polymer-based optical waveguides: Materials, processing, and devices," *Advanced Materials*, vol. 14, no. 19, pp. 1339–1365, 2002.
- [4] D. A. B. Miller, "Physical reasons for optical interconnection," *International Journal of Optoelectronics*, vol. 11, no. 3, pp. 155–168, 1997.
- [5] J. Beals *et al.*, "A terabit capacity passive polymer optical backplane based on a novel meshed waveguide architecture," *Applied Physics A*, vol. 95, no. 4, pp. 983–988, 2009.
- [6] N. Bamiedakis, T. Hutter, R. V. Penty, I. H. White, and S. R. Elliott, "PCB-integrated optical waveguide sensors: An ammonia gas sensor," *Journal of Lightwave Technology*, vol. 31, no. 10, pp. 1628–1635, 2013.
- [7] C. Monat, P. Domachuk, and B. J. Eggleton, "Integrated optofluidics: A new river of light," *Nature photonics*, vol. 1, no. 2, pp. 106–114, 2007.
- [8] D. R. Reyes, D. Iossifidis, P.-A. Auroux, and A. Manz, "Micro total analysis systems. 1. Introduction, theory, and technology," *Analytical Chemistry*, vol. 74, no. 12, pp. 2623–2636, 2002.
- [9] R. A. Potyrailo, S. E. Hobbs, and G. M. Hieftje, "Optical waveguide sensors in analytical chemistry: today's instrumentation, applications and trends for future development," *Fresenius' Journal of Analytical Chemistry*, vol. 362, no. 4, pp. 349–373, 1988.
- [10] P. Polynkin, A. Polynkin, N. Peyghambarian, and M. Mansuripur, "Evanescent field-based optical fiber sensing device for measuring the refractive index of liquids in microfluidic channels," *Optics Letters*, vol. 30, no. 11, pp. 1273–1275, 2005.
- [11] S. W. Kang, K. Sasaki, and H. Minamitani, "Sensitivity analysis of a thin-film optical waveguide biochemical sensor using evanescent field absorption," *Applied Optics*, vol. 32, no. 19, pp. 3544–3549, 1993.
- [12] A. Banerjee *et al.*, "Fiber optic sensing of liquid refractive index," *Sensors and Actuators B: Chemical*, vol. 123, no. 1, pp. 594–605, 2007.
- [13] L. Zhang *et al.*, "Optofluidic refractive index sensor based on partial reflection," *Photonic Sensors*, vol. 7, no. 2, pp. 97–104, 2017.
- [14] J. S. Kee, D. P. Poenar, L. Yobas, and Y. Chen, "Evanescent field absorption spectroscopy on poly(dimethylsiloxane) single-mode rib waveguide integrated with microfluidic system," in *14th International Conference on Miniaturized Systems for Chemistry and Life Sciences*, Groningen, the Netherlands, 2010, pp. 1256–1258.

- [15] F. B. Xiong, W. Z. Zhu, H. F. Lin, and X. G. Meng, "Fiber-optic sensor based on evanescent wave absorbance around 2.7 μm for determining water content in polar organic solvents," *Applied Physics B*, vol. 115, no. 1, pp. 129–135, 2014.
- [16] E. Archibong, J. Stewart, and A. Pyayt, "Optofluidic spectroscopy integrated on optical fiber platform," *Sensing and Bio-Sensing Research*, vol. 3, pp. 1–6, 2015.
- [17] D. Yin *et al.*, "Planar optofluidic chip for single particle detection, manipulation, and analysis," *Lab on a chip*, vol. 7, no. 9, pp. 1171–1175, 2007.
- [18] Y. Zhang *et al.*, "Optofluidic device based microflow cytometers for particle/cell detection: A review," *Micromachines*, vol. 7, no. 4, p. 70, 2016.
- [19] A. Alrifaiy, O. A. Lindahl, and K. Ramser, "Polymer-based microfluidic devices for pharmacy, biology and tissue engineering," *Polymers*, vol. 4, no. 4, pp. 1349–1398, 2012.
- [20] X. Cui *et al.*, "Lensless high-resolution on-chip optofluidic microscopes for *Caenorhabditis elegans* and cell imaging," *PNAS*, vol. 105, no. 31, pp. 10670–10675, 2008.
- [21] Y. C. Seow, S. P. Lim, and H. P. Lee, "Optofluidic variable-focus lenses for light manipulation," *Lab on a chip*, vol. 12, no. 19, pp. 3810–3815, 2012.
- [22] Thorlabs, *Product catalog: optical fiber and patch cables*. [Online] Available: https://www.thorlabs.com/navigation.cfm?guide_id=26.
- [23] D. Psaltis, S. R. Quake, and C. Yang, "Developing optofluidic technology through the fusion of microfluidics and optics," *Nature*, vol. 442, no. 7101, pp. 381–386, 2006.
- [24] P. Abgrall and A.-M. Gué, "Lab-on-chip technologies: making a microfluidic network and coupling it into a complete microsystem-a review," *Journal of Micromechanics and Microengineering*, vol. 17, no. 5, R15-R49, 2007.
- [25] K. Leosson and B. Agnarsson, "Integrated Biophotonics with CYTOP," *Micromachines*, vol. 3, no. 4, pp. 114–125, 2012.
- [26] V. Prajzler, M. Knietael, and R. Maštera, "Large core optical planar splitter for visible and infrared region," *Optical and Quantum Electronics*, vol. 48, no. 2, 2016.
- [27] J. Yuan, F. Luo, X. Zhou, Q. Huang, and M. Cao, "Optical interconnection in embedded-fiber printer circuit boards," *Optik - International Journal for Light and Electron Optics*, vol. 119, no. 1, pp. 46–50, 2008.
- [28] M. Immonen, "Development of optical interconnect PCBs for high-speed electronic systems: Fabricator's view," in *IBM Printed Circuit Board Symposium*, Raleigh, NC, USA, 2011.
- [29] R. Dangel *et al.*, "Development of versatile polymer waveguide flex technology for use in optical interconnects," *Journal of Lightwave Technology*, vol. 31, no. 24, pp. 3915–3926, 2013.
- [30] M. Nordström, D. A. Zauner, A. Boisen, and J. Hübner, "Monolithic single mode SU-8 waveguides for integrated optics," in *MOEMS-MEMS 2006, Micro and Nanofabrication*, San Jose, United States, 2006, 611206-1 - 611206-11.
- [31] M. Singh, K. Kitazoe, K. Moriya, and A. Horimoto, "High reliability and high density graded index polymer waveguides for optical interconnect," *Optics Communications*, vol. 362, pp. 33–35, 2016.

- [32] K. Kruse, J. Peng, and C. T. Middlebrook, "Laser direct writing of complex radially varying single-mode polymer waveguide structures," *Journal of Micro/Nanolithography, MEMS, and MOEMS*, vol. 14, no. 3, p. 34502, 2015.
- [33] R. Dangel *et al.*, "Polymer-waveguide-based board-level optical interconnect technology for datacom applications," *IEEE Transactions on Advanced Packaging*, vol. 31, no. 4, pp. 759–767, 2008.
- [34] G. van Steenberge *et al.*, "Laser ablation of parallel optical interconnect waveguides," *IEEE Photonics Technology Letters*, vol. 18, no. 9, pp. 1106–1108, 2006.
- [35] S. S. Zakariyah, P. P. Conway, D. A. Hutt, N. Suyal, and D. R. Selviah, "Integrated in-plane mirror and multimode waveguide fabrication using 248 nm excimer laser ablation for optical interconnects on PCBs," *Circuit World*, vol. 38, no. 2, pp. 59–63, 2012.
- [36] M. U. Khan *et al.*, "Multi-level single mode 2D polymer waveguide optical interconnects using nano-imprint lithography," *Optics Express*, vol. 23, no. 11, pp. 14630–14639, 2015.
- [37] T. Korhonen *et al.*, "Multilayer single-mode polymeric waveguides by imprint patterning for optical interconnects," in *OPTO SPIE Photonics West*, San Francisco, California, United States, 2014.
- [38] R. Houbertz, S. Steenhusen, T. Stichel, and G. Sextl, "Two-photon polymerization of inorganic-organic hybrid polymers as scalable technology using ultra-short laser pulses emission," in *Coherence and Ultrashort Pulse Laser*, D.F.J. Duarte, Ed., 2010.
- [39] M. Rezem, A. Günther, M. Rahlves, B. Roth, and E. Reithmeier, "Fabrication and sensing applications of multilayer polymer optical waveguides," *Procedia Technology*, vol. 26, pp. 517–523, 2016.
- [40] C.-S. Huang and W.-C. Wang, "Large-core single-mode rib SU8 waveguide using solvent-assisted microcontact molding," *Applied Optics*, vol. 47, no. 25, p. 4540, 2008.
- [41] E. Tadayuki and T. Ishigure, "Direct fabrication for smooth end facets on GI-core polymer waveguide using the Mosquito method," in *6th International Conference on Photonics (ICP)*, Sarawak, Malaysia, 2016.
- [42] T. Ishigure, S. Yoshida, K. Yasuhara, and D. Sukanuma, "Low-loss single-mode polymer optical waveguide at 1550-nm wavelength compatible with silicon photonics," in *65th Electronic Components and Technology Conference (ECTC)*, San Diego, CA, USA, 2015, pp. 768–774.
- [43] J. Chappell, D. A. Hutt, and P. P. Conway, "Variation in the line stability of an inkjet printed optical waveguide-applicable material," in *2nd Electronics System-Integration Technology Conference*, Greenwich, UK, 2008, pp. 1267–1272.
- [44] A. Tervonen, B. R. West, and S. Honkanen, "Ion-exchanged glass waveguide technology: A review," *Optical Engineering*, vol. 50, no. 7, 1-15, 2011.
- [45] M. Kufner and S. Kufner, "Ion exchange technology for optical waveguides," *Optik & Photonik*, vol. 6, no. 4, pp. 32–34, 2011.
- [46] H. Folkert, "Combining Si-photonics and optical PCB's," in *LEOS Annual Meeting Conference*, Belek-Antalya, Turkey, 2009.

- [47] T. Tsuchizawa *et al.*, "Microphotonic devices based on silicon microfabrication technology," *IEEE Journal of Selected Topics in Quantum Electronics*, vol. 11, no. 1, pp. 232–240, 2005.
- [48] D. R. Selviah *et al.*, "Integrated optical and electronic interconnect PCB manufacturing research," *Circuit World*, vol. 36, no. 2, pp. 5–19, 2010.
- [49] A. Elmogi, E. Bosman, J. Missinne, and G. van Steenberge, "Comparison of epoxy- and siloxane-based single-mode optical waveguides defined by direct-write lithography," *Optical Materials*, vol. 52, pp. 26–31, 2016.
- [50] Y. Temiz, R. D. Lovchik, G. V. Kaigala, and E. Delamarche, "Lab-on-a-chip devices: How to close and plug the lab?," *Microelectronic Engineering*, vol. 132, pp. 156–175, 2015.
- [51] I. Papakonstantinou, D. R. Selviah, R. C. A. Pitwon, and D. Milward, "Low-cost, precision, self-alignment technique for coupling laser and photodiode arrays to polymer," *IEEE Transactions on Advanced Packaging*, vol. 31, no. 3, pp. 502–511, 2008.
- [52] B. E.A. Saleh, Ed., *Fundamentals of Photonics*, 2nd ed. Hoboken, New Jersey: John Wiley & Sons, Inc, 2007.
- [53] Microresist Technology GmbH, *Processing Guidelines: Negative tone photoresist series EpoCore/EpoClad*.
- [54] H. P. Zappe, *Fundamentals of micro-optics*. Cambridge: Cambridge University Press, 2010.
- [55] R. D. Craig Hoffman, *Encyclopedia of Optical and Photonic Engineering*. Fresnel Equations, 2nd ed. Boca Raton: Taylor & Francis, 2015.
- [56] Fiber Instrument Sales, *Matching gel F1-0001V: Data Sheet*. Available: <http://www.fiberinstrumentsales.com/specs/FIS-MatchingGel.pdf>.
- [57] A. Ivanova, R. Stoffer, M. Hammer, *2-D multilayer waveguide mode solver: variational effective index approximation*: University of Twente, 2009.
- [58] A. Ivanova, R. Stoffer, and M. Hammer, "A variational mode solver for optical waveguides based on quasi-analytical vectorial slab mode expansion," University of Twente, the Netherlands, 2013. [Online] Available: <http://arxiv.org/pdf/1307.1315v2>.
- [59] R. Scarmozzino, A. Gopinath, R. Pregla, and S. Helfert, "Numerical techniques for modeling guided-wave photonic devices," *IEEE Journal of Selected Topics in Quantum Electronics*, vol. 6, no. 1, pp. 150–162, 2000.
- [60] K. S. Chiang, "Review of numerical and approximate methods for the modal analysis of general optical dielectric waveguides," *Optical and Quantum Electronics*, vol. 26, no. 3, S113-S134, 1994.
- [61] C. Vassallo, "1993-1995 Optical mode solvers," *Optical and Quantum Electronics*, vol. 29, no. 2, pp. 95–114, 1997.
- [62] F. Mitschke, *Fiber optics: Physics and technology*. Berlin, London: Springer, 2009.
- [63] E. Squillante, "Applications of fiber-optic evanescent wave spectroscopy," *Drug development and industrial pharmacy*, vol. 24, no. 12, pp. 1163–1175, 1998.

- [64] K. S. Chiang, "Polymer optical waveguide devices for mode-division-multiplexing applications," in *SPIE Optics + Optoelectronics*, Prague, Czech Republic, 2017, 102420R-1 - 102420R-12.
- [65] D. Axelrod, "Total internal reflection fluorescence microscopy in cell biology," *Traffic*, vol. 2, no. 11, pp. 764–774, 2001.
- [66] Robert A. Meyers, "Infrared spectroscopy in clinical and diagnostic analysis," in *Encyclopedia of Analytical Chemistry*, R. Anthony Shaw Henry H. Mantsch, Ed., Chichester: John Wiley & Sons Ltd, 2006.
- [67] L. A. Eldada and L. W. Shacklette, "Advances in polymer integrated optics," *IEEE Journal of Selected Topics in Quantum Electronics*, vol. 6, no. 1, pp. 54–68, 2000.
- [68] S. Soloman, Ed., *Sensors Handbook*. New York, United States: McGraw-Hill Companies, Inc., 2010.
- [69] A. Argyros, R. Lwin, and M. C. J. Large, "Bend loss in highly multimode fibres," *Optics Express*, vol. 16, no. 23, p. 18590, 2008.
- [70] School of Electronic and Communications Engineering, "Optical Communications Systems: Bending Loss and Reliability in Optical Fibres," Dublin, 2014.
- [71] D. Nhiwatiwa, "Comparison of macrobend losses in Single Mode fibre (SMF) and Multimode Fibre (MMF)," M.Sc. thesis, Department of Physics, University of Zimbabwe, Harare, Zimbabwe, 2012.
- [72] N. Bamiedakis, R. V. Penty, and I. H. White, "Compact multimode polymer waveguide bends for board-level optical interconnects," *Journal of Lightwave Technology*, vol. 31, no. 14, pp. 2370–2375, 2013.
- [73] D. F. G. Gallagher, "Photonic CAD matures: Industry research highlights," *IEEE LEOS The society for photonics*, vol. 22, no. 1, 2008.
- [74] N. Riegel, "Optical waveguides and structures for short haul optical communication channels within printed circuit boards," Ph.D. dissertation, Michigan Technological University, Houghton, United States, 2013.
- [75] N. Riegel, C. Middlebrook, K. Kruse, and M. Roggemann, "Using the 3D beam propagation method to model the effects of lithographic roughness on the attenuation of highly multimodal polymer waveguides," *Journal of Vacuum Science and Technology: B*, vol. 31, no. 3, 0312061-0312066, 2013.
- [76] *Lasers and laser-related equipment – Test methods for laser beam widths, divergence angles and beam propagation ratios – Part 2: General astigmatic beams*, ISO 11146-2: 2015, 2005.
- [77] M. Immonen *et al.*, "Development of electro - optical PCBs with polymer waveguides for high - speed intra - system interconnects," *Circuit World*, vol. 38, no. 3, pp. 104–112, 2012.
- [78] J. Mohr, Ed., *Mikrosystemtechnik für Ingenieure*, 3rd ed. Weinheim: Wiley-VCH Verlag GmbH & Co. KGaA, 2005.
- [79] Microresist Technology GmbH, *Core and Cladding systems for waveguiding: Comparison of the material systems OrmoCore & OrmoClad and EpoCore & EpoClad*.

- [80] S. Kobayashi and K. Müllen, Eds., *Encyclopedia of polymeric nanomaterials*. Berlin, Heidelberg: Springer Berlin Heidelberg, 2015.
- [81] M. Schwaerzle, P. Ringwald, O. Paul, and P. Ruther, "First dual-color optrode with bare laser diode chips directly butt-coupled to hybrid-polymer waveguides," in *30th IEEE International Conference on Micro Electro Mechanical Systems (MEMS)*, Las Vegas, Nevada, USA, 2017, 526–529.
- [82] E. Fiedler, N. Haas, and T. Stieglitz, "Suitability of SU-8, EpoClad and EpoCore for flexible waveguides on implantable neural probes," in *36th annual international conference of the IEEE Engineering in Medicine and Biology Society (EMBC)*, Chicago, IL, United States, 2014, pp. 438–441.
- [83] "Company presentation," Heiden, Switzerland, 2015.
- [84] K. Kruse and C. T. Middlebrook, "Polymer taper bridge for silicon waveguide to single mode waveguide coupling," *Optics Communications*, vol. 362, pp. 87–95, 2016.
- [85] Microresist Technology GmbH, "Processing Guidelines: Negative Tone Photoresist Series EpoCore," Microresist Technology GmbH, Berlin, 2016.
- [86] F. Testa and L. Pavesi, Eds., *Optical switching in next generation data centers*. Cham: Springer International Publishing, 2018.
- [87] Abu Sahmah Mohd Supa'at, "Implementation of thermo-optic waveguide photonics switch using polymer material," in *4th International Conference on Photonics (ICP)*, Melaka, Malaysia, 2013, pp. 33–37.
- [88] Z. Zhang and N. Keil, "Thermo-optic devices on polymer platform," *Optics Communications*, vol. 362, pp. 101–114, 2016.
- [89] D. Cai, "Optical and mechanical aspects of polysiloxane based electrical-optical-circuits-board," Ph.D. dissertation, TU Dortmund University, Dortmund, Germany, 2008.
- [90] V. Prajzler, P. Hys, R. Mastera, and P. Nekvindova, "Properties of siloxane based optical waveguides deposited on transparent paper and foil," *Radioengineering*, vol. 25, no. 2, pp. 230–235, 2016.
- [91] Y.-G. Zhao *et al.*, "Polymer waveguides useful over a very wide wavelength range from the ultraviolet to infrared," *Applied Physics Letters*, vol. 77, no. 19, pp. 2961–2963, 2000.
- [92] Y. Hanada, K. Sugioka, and K. Midorikawa, "UV waveguides light fabricated in fluoropolymer CYTOP by femtosecond laser direct writing," *Optics Express*, vol. 18, no. 2, pp. 446–450, 2010.
- [93] W.-C. Chuang, C.-T. Ho, and W.-C. Chang, "Fabrication of polymer waveguides by a replication method," *Applied Optics*, vol. 45, no. 32, p. 8304, 2006.
- [94] M. Nordstrom, D. A. Zauner, A. Boisen, and J. Hubner, "Single-mode waveguides with SU-8 polymer core and cladding for MOEMS applications," *Journal of Lightwave Technology*, vol. 25, no. 5, pp. 1284–1289, 2007.
- [95] L. Strauch, "EpoCore & EpoClad — New materials for optical wave guides in PCB," micro resist technology GmbH, Berlin, 2014. [Online] Available: <http://www.microchem.com/>. Accessed on: Feb. 02 2016.

- [96] V. Prajzler, P. Nekvindova, P. Hybs, and V. Jerabek, "Properties of the optical planar polymer waveguides deposited on printed circuit boards," *Radioengineering*, vol. 24, no. 2, pp. 442–448, 2015.
- [97] V. Prajzler, M. Neruda, P. Nekvindova, and P. Mikulik, "Properties of multimode optical epoxy polymer waveguides deposited on silicon and TOPAS substrate," *Radioengineering*, vol. 26, no. 1, pp. 10–15, 2017.
- [98] J. Zhou, W. H. Wong, E.Y.B. Pun, Y. Q. Shen, and Y. X. Zhao, "Fabrication of low loss optical waveguides with a novel thermo-optical polymer material," *Optica Applicata*, vol. XXXVI, no. 2-3, pp. 429–435, 2006.
- [99] Microresist Technology GmbH, "Ormocore,Ormoclad: ORMOCER® system for planar optical waveguides," Microresist Technology GmbH, Berlin, Germany. [Online] Available: http://www.microresist.de/products/ormocers/pdf/pi_ormocore_clad_en_07062201_ls_neu.pdf.
- [100] T. A. Anhoj, A. M. Jorgensen, D. A. Zauner, and J. Hübner, "The effect of soft bake temperature on the polymerization of SU-8 photoresist," *Journal of Micromechanics and Microengineering*, vol. 16, no. 9, pp. 1819–1824, 2006.
- [101] R. Martinez-Duarte and M. J. Madou, "SU-8 photolithography and its impact on microfluidics," in *Microfluidics and Nanofluidics Handbook: Fabrication, Implementation, and Applications*, Sushanta K. Mitra, Suman Chakraborty, Ed., 1st ed.: CRC Press, 2018, pp. 231–268.
- [102] MicroChem Corp., "SU-8 2000 permanent epoxy negative photoresist: Processing guidelines," MicroChem Corp., Newton, MA.
- [103] Hamoudi Asiri, "Fabrication of surface plasmon biosensors in CYTOP," M.Sc. thesis, Department of Chemical and Biological Engineering, University of Ottawa, Ottawa, Ontario, Canada, 2012.
- [104] Isola Group GmbH, "IS400 High Performance Laminate and Prepreg: Specifications," Düren, Germany. [Online] Available: <http://www.isola-group.com/wp-content/uploads/2015/12/IS400-High-Performance-Laminate-and-Prepreg-Data-Sheet-Isola.pdf>.
- [105] SCHOTT Technical Glass Solutions GmbH, "SCHOTT BOROFLOAT® 33," Jena, Germany. [Online] Available: https://www.schott.com/d/borofloat/b89578c1-3509-40a2-aacf-ca3c2371ef7b/1.0/borofloat33_therm_eng_web.pdf.
- [106] MicroChem Corp., "SU-8 3000: Permanent epoxy negative photoresist," Newton, MA.
- [107] Evonik Industries AG, "Spannungsris- und Chemikalienbeständigkeit: PLEXIGLAS® GS, PLEXIGLAS® XT, PLEXIGLAS RESIST® XT," Darmstadt, Germany, May. 2000. [Online] Available: https://www.plexiglas-hecker.de/wordpress_c/wp-content/uploads/2016/09/Chemikalienbestaendigkeit-Plexiglas.pdf.
- [108] Evonik Industries AG, "Technical Information PLEXIGLAS®," Darmstadt, Germany, Jan. 2013. [Online] Available: <https://www.plexiglas.net/sites/lists/pm/documentsap/211-1-plexiglas-gs-xt-en.pdf>.

- [109] N. Wangler *et al.*, “High-resolution permanent photoresist laminate TMMF for sealed microfluidic structures in biological applications,” *Journal of Micromechanics and Microengineering*, vol. 21, no. 9, p. 95009, 2011.
- [110] L. Deng, “Preparation of synthetic membranes,” IKP, NTNU, 2016 Fall.
- [111] E. Sergeeva, “Entwicklung von neuartigen Verfahren zur Herstellung von polymerbasierten superamphiphoben Oberflächen mit robusten Benetzungseigenschaften,” M.Sc. thesis, RWTH Aachen University, 2014.
- [112] MicroChem Corp., “NANO SU-8: Negative tone photoresist formulations 50-100,” MicroChem Corp., Newton, MA.
- [113] Micro/Nano Technology Center, “Spin coating process theory,” University of Louisville, Louisville, United States, 2013. [Online] Available: <https://louisville.edu/micronano/files/documents/standard-operating-procedures/SpinCoatingInfo.pdf>.
- [114] C. Koch and Rinke, Titus, J., “Lithography trouble shooter: Questions and answers around the most common problems in microstructuring,” MicroChemicals GmbH, Ulm, 2014. [Online] Available: https://www.microchemicals.com/technical_information/TroubleShooter_EN.pdf.
- [115] W. Wang and S. A. Soper, Eds., *Bio-MEMS: Technologies and applications*. Boca Raton: CRC/Taylor & Francis, 2007.
- [116] Microresist Technology GmbH, “Processing guidelines - EpoClad: Negative tone photoresist series,” Microresist Technology GmbH, Berlin, 2015.
- [117] E. Zraggen, “Fabrication and system integration of single-mode polymer optical waveguides,” 2014.
- [118] MicroChemicals GmbH, “Laser-exposure of photoresists (white paper),” 2013.
- [119] J. R. Salgueiro, V. Moreno, and J. Liñares, “Model of linewidth for laser writing on a photoresist,” *Applied Optics*, vol. 41, no. 5, p. 895, 2002.
- [120] E. Rabe, S. Kopetz, and A. Neyer, “The generation of mould patterns for multimode optical waveguide components by direct laser writing of SU-8 at 364 nm,” *Journal of Micromechanics and Microengineering*, vol. 17, no. 8, pp. 1664–1670, 2007.
- [121] N. Bamiedakis *et al.*, “Cost-effective multimode polymer waveguides for high-speed on-board optical interconnects,” *IEEE Journal of Quantum Electronics*, vol. 45, no. 4, pp. 415–424, 2009.
- [122] S. Keller, G. Blagoi, M. Lillemose, D. Haefliger, and A. Boisen, “Processing of thin SU-8 films,” *Journal of Micromechanics and Microengineering*, vol. 18, no. 12, p. 125020, 2008.
- [123] MicroChemicals GmbH, “Exposure of photoresists (white paper),” 2013.
- [124] J. C. Dingeldein, “Direct write fabrication of waveguides and interconnects for optical printed wiring boards,” Michigan Technological University, 2012.
- [125] M. Immonen *et al.*, “Development of electro - optical PCBs with polymer waveguides for high - speed intra - system interconnects,” *Circuit World*, vol. 38, no. 3, pp. 104–112, 2012.

- [126] K. Kruse and C. T. Middlebrook, "Laser-direct writing of single mode and multi-mode polymer step index waveguide structures for optical backplanes and interconnection assemblies," *Photonics and Nanostructures - Fundamentals and Applications*, vol. 13, pp. 66–73, 2014.
- [127] Y. Ichihashi, T. Mappes, and J. Mohr, "UV-induzierte Brechzahländerung zur Herstellung von Wellenleitern und Integration von Siliziumphotodioden," Ph.D. dissertation, Institut für Mikrostrukturtechnik, Forschungszentrum Karlsruhe GmbH, Karlsruhe, 2007.
- [128] K. Kruse, N. Riegel, C. Demars, C. Middlebrook, and M. Roggemann, "Optical waveguide end roughness in correlation to optical coupling," *SPIE Proceedings: Optoelectronic Interconnects XII*, vol. 8267, 2012.
- [129] H. Baghsiahi, Kai Wang, W. Kandulski, R. C. A. Pitwon, and D. R. Selviah, "Optical waveguide end facet roughness and optical coupling loss," *Journal of Lightwave Technology*, vol. 31, no. 16, pp. 2659–2668, 2013.
- [130] M. S. Ab-Rahman *et al.*, "The study of the good polishing method for polymer SU-8 waveguide," *Optica Applicata*, vol. XXXIX, no. 3, 2009.
- [131] M. H. Ibrahim, N. M. Kassim, A. B. Mohammad, and Supaat, A. S. M., "Facet polishing technique for polymer on glass optical waveguide," *Journal of Optoelectronics and Advanced Materials*, vol. 3, no. 3, 2009.
- [132] M. S. Ab-Rahman, F. Ab-Aziz, Arif, Noor Azie Azura Mohd, S. D. Zan, and S. M. Mustaza, "The polishing of cutting-edge polymer-on-glass for pigtailling preparation," *American Journal of Engineering and Applied Sciences*, vol. 2, no. 1, pp. 127–132, 2009.
- [133] T. Guan, F. Ceysens, and R. Puers, "An EpoClad/EpoCore-based platform for MOEMS fabrication," *Journal of Micromechanics and Microengineering*, vol. 23, no. 12, p. 125005, 2013.
- [134] F. Ceysens, M. Driesen, K. Wouters, and R. Puers, "A low-cost and highly integrated fiber optical pressure sensor system," *Sensors and Actuators A: Physical*, vol. 145-146, pp. 81–86, 2008.
- [135] P. Henzi, D. G. Rabus, K. Bade, U. Wallrabe, and J. Mohr, "Low-cost single-mode waveguide fabrication allowing passive fiber coupling using LIGA and UV flood exposure," *SPIE, Micro-Optics: Fabrication, Packaging, and Integration*, vol. 5454, pp. 64–74, 2008.
- [136] A. Günther *et al.*, "Cladded self-written multimode step-index waveguides using a one-polymer approach," *Optics Letters*, vol. 40, no. 8, pp. 1830–1833, 2015.
- [137] K.-L. Deng *et al.*, "Self-aligned single-mode polymer waveguide interconnections for efficient chip-to-chip optical coupling," *IEEE Journal of Selected Topics in Quantum Electronics*, vol. 12, no. 5, pp. 923–930, 2006.
- [138] J. Steigert *et al.*, "A versatile and flexible low-temperature full-wafer bonding process of monolithic 3D microfluidic structures in SU-8," *Journal of Micromechanics and Microengineering*, vol. 18, no. 9, p. 95013, 2008.
- [139] Walter Lemmen GmbH, "DYNAMASK KM - Trockenfilm-Lötstopmmaske: Morton, Technical Data,"

- [140] H. Bathel, "Polymer-Wellenleiter zur Messung der Brechzahl in Fluiden," B.Sc. Thesis, University of Rostock, Rostock, Germany, 2018.
- [141] R. G. Hunsperger, *Integrated optics: Theory and technology*, 6th ed. New York, London: Springer, 2009.
- [142] E. Dermitzaki, B. Wunderle, J. Bauer, H. Walter, and B. Michel, "Structure property correlation of epoxy resins under the influence of moisture; and comparison of diffusion coefficient with MD-simulations," in *9th. Int. Conf. on Thermal, Mechanical and Multiphysics Simulation and Experiments in Micro-Electronics and Micro-Systems, EuroSimE 2008*, Freiburg-im-Breisgau, Germany, 2008.
- [143] N. Bamiedakis *et al.*, "Cost-effective multimode polymer waveguides for high-speed on-board optical interconnects," *IEEE Journal of Quantum Electronics*, vol. 45, no. 4, pp. 415–424, 2009.
- [144] K. L. Kruse and C. T. Middlebrook, "Fan-out routing and optical splitting techniques for compact optical interconnects using single-mode polymer waveguides," *Journal of Modern Optics*, vol. 62, no. S2, pp. S1-S10, 2014.
- [145] I. Papakonstantinou, R. James, and D. R. Selviah, "Radiation- and bound-mode propagation in rectangular, multimode dielectric, channel waveguides with sidewall roughness," *Journal of Lightwave Technology*, vol. 27, no. 18, pp. 4151–4163, 2009.
- [146] R. Pitwon *et al.*, "Polymer optical waveguides with reduced in-plane bend loss for electro-optical PCBs," *Proceedings of the SPIE*, vol. 8264, 2012.
- [147] Evonik, *Spannungsris- und Chemikalienbestaendigkeit: PLEXIGLAS®GS, PLEXIGLAS®XT, PLEXIGLAS RESIST®XT*. [Online] Available: https://www.plexiglas-hecker.de/wordpress_c/wp-content/uploads/2016/09/Chemikalienbestaendigkeit-Plexiglas.pdf.
- [148] E. Sergeeva, H. Hartwig, and D. Hohlfeld, "Optofluidic cuvettes with integrated polymer waveguides for fluid analysis on printed circuit boards," in *7th MikroSystemTechnik Kongress "MEMS, Mikroelektronik, Systeme"*, Munich, 2017, pp. 281–284.
- [149] K. Bescherer, D. Munzke, O. Reich, and H.-P. Loock, "Fabrication and modeling of multimode fiber lenses," *Applied Optics*, vol. 52, no. 4, B40-5, 2013.
- [150] M. Polyanskiy, *Refractive index database*. [Online] Available: <https://refractiveindex.info/>. Accessed on: May 16 2018.
- [151] P. Lutus, *OpticalRayTracer*, 2016.
- [152] P. Nath, H. K. Singh, P. Datta, and K. C. Sarma, "All-fiber optic sensor for measurement of liquid refractive index," *Sensors and Actuators A: Physical*, vol. 148, no. 1, pp. 16–18, 2008.
- [153] I. Klimant, M. Kühn, R. N. Glud, and G. Holst, "Optical measurement of oxygen and temperature in microscale: strategies and biological applications," *Sensors and Actuators B*, vol. 38-39, pp. 29–37, 1997.
- [154] M. H. Gholizadeh, A. M. Melesse, and L. Reddi, "A comprehensive review on water quality parameters estimation using remote sensing techniques," *Sensors*, vol. 16, no. 8, 2016.

- [155] C. Papoutsas, D. G. Hadjimitsis, S. Perdikou, A. Retalis, and L. Toullos, "Smart monitoring of water quality in Asprokremmos Dam in Paphos, Cyprus using satellite remote sensing and wireless-sensor platform," in *Remote Sensing*, Toulouse, France, 2010.
- [156] E.-J. Lee *et al.*, "Comparison of UV–VIS and FDOM sensors for in situ monitoring of stream DOC concentrations," *Biogeosciences*, vol. 12, no. 10, pp. 3109–3118, 2015.
- [157] F. Betschon *et al.*, "Novel optical titration sensor based on integrated planar polymer waveguides," in *SENSOR+TEST Conference*, Nürnberg, 2011, pp. 89–94.
- [158] C. Li, G. Bai, Y. Zhang, M. Zhang, and A. Jian, "Optofluidics Refractometers," *Micromachines*, vol. 9, no. 3, p. 136, 2018.
- [159] Y. Xiao *et al.*, "Towards integrated resonant and interferometric sensors in polymer films," *Procedia Technology*, vol. 15, pp. 691–701, 2014.
- [160] B. J. Luff *et al.*, "Integrated optical Mach-Zehnder biosensor," *Journal of Lightwave Technology*, vol. 16, no. 4, pp. 583–592, 1998.
- [161] L. Ji *et al.*, "Surface plasmon resonance refractive index sensor based on ultraviolet bleached polymer waveguide," *Sensors and Actuators B: Chemical*, vol. 244, pp. 373–379, 2017.
- [162] S. Thomas Lee *et al.*, "Long period gratings in multimode optical fibers: Application in chemical sensing," *Optics Communications*, vol. 224, no. 4-6, pp. 237–241, 2003.
- [163] Z. P. Lee *et al.*, "Secchi disk depth: A new theory and mechanistic model for underwater visibility," *Remote Sensing of Environment*, vol. 169, pp. 139–149, 2015.
- [164] W. Demtröder, *Laser spectroscopy: Basic concepts and instrumentation*, 2nd ed. Berlin, New York: Springer, 1996.
- [165] J. Schmidt, "Messgerät zur Absorptionsmessung in optofluidischen Platinen auf Leiterplattenebene," M.Sc. thesis, University of Rostock, Rostock, Germany, 2017.
- [166] L. Kingbright Electronic Co., *Data Sheet: KPTD-1608LVSECK-J3-PF, SMD chip LED lamp green*. [Online] Available: <http://www.kingbright.com/content/listitem/products/75>.
- [167] J. Schmidt, E. Sergeeva, H. Hartwig, and D. Hohlfeld, "Integration von SMD-LEDs in elektrisch-optische Leiterplatten für Sensoranwendungen," in *7th MikroSystemTechnik Kongress "MEMS, Mikroelektronik, Systeme"*, Munich, 2017.
- [168] S. Nunn and K. Nishikida, "Advanced ATR Correction Algorithm," Application Note, Thermo Fisher Scientific, Application Note 50581.
- [169] Jasco International Co., Ltd, "ATR Method: Application Note," Tokyo, Japan 280-AT-0002.
- [170] A. Prabhakar and S. Mukherji, "Microfabricated polymer chip with integrated U-bend waveguides for evanescent field absorption based detection," *Lab on a chip*, vol. 10, no. 6, pp. 748–754, 2010.
- [171] J. H. Ryu *et al.*, "Design and analysis of refractometer based on bend waveguide structure with air trench for optical sensor applications," *ETRI Journal*, vol. 36, no. 5, pp. 841–846, 2014.

- [172] V. Balapuram, "Design and fabrication of multimode optical waveguides for polymer based optical printed circuit boards," M.Sc. thesis, Institute of Electronic Appliances and Circuits, University of Rostock, Rostock, Germany, 2015.
- [173] G. Gauglitz and T. Vo-Dinh, Eds., *Handbook of spectroscopy*. Weinheim, Cambridge: Wiley-VCH, 2003.
- [174] A. Suzuki, J. Kondoh, Y. Matsui, S. Shiokawa, and K. Suzuki, "Development of novel optical waveguide surface plasmon resonance (SPR) sensor with dual light emitting diodes," *Sensors and Actuators B: Chemical*, vol. 106, no. 1, pp. 383–387, 2005.
- [175] C.-Y. Chao, W. Fung, and L. J. Guo, "Polymer microring resonators for biochemical sensing applications," *IEEE Journal of Selected Topics in Quantum Electronics*, vol. 12, no. 1, pp. 134–142, 2006.
- [176] G. Testa, G. Persichetti, and R. Bernini, "Liquid core ARROW waveguides: A promising photonic structure for integrated optofluidic microsensors," *Micromachines*, vol. 7, no. 3, p. 47, 2016.
- [177] C. Wu *et al.*, "In-line microfluidic integration of photonic crystal fibres as a highly sensitive refractometer," *The Analyst*, vol. 139, no. 21, pp. 5422–5429, 2014.
- [178] N. Zhang *et al.*, "In-line optofluidic refractive index sensing in a side-channel photonic crystal fiber," *Optics Express*, vol. 24, no. 24, pp. 27674–27682, 2016.
- [179] I. N. Bronstein, H. Mühlig, G. Musiol, and K. A. Semendjajew, *Taschenbuch der Mathematik*, 10th ed. Haan: Europa-Lehrmittel, 2016.
- [180] OZ optics Ltd., *Data Sheet: Laser diode sources - fiber optic*. [Online] Available: http://www.ozoptics.com/ALLNEW_PDF/DTS0019.pdf.
- [181] R. Kumar, "A high temperature nano/micro vapor phase conformal coating for electronics applications," in *High Temperature Electronics Network (HiTEN)*, Churchill College, Cambridge, UK, 2015, pp. 83–90.
- [182] Y. Xiao, M. Hofmann, Z. Wang, S. Sherman, and H. Zappe, "Design of all-polymer asymmetric Mach-Zehnder interferometer sensors," *Applied Optics*, vol. 55, no. 13, pp. 3566–3573, 2016.
- [183] R. Bruck, "High index difference polymer waveguide Mach-Zehnder interferometer biosensor, compatible with injection molding and spin-coating," Ph.D. dissertation, University of Vienna, Vienna, Austria, 2010.
- [184] S. Dante *et al.*, "All-optical phase modulation for integrated interferometric biosensors," *Optics Express*, vol. 20, no. 7, pp. 7195–7205, 2012.
- [185] T. L. Bergman, A. Lavine, and F. P. Incropera, *Fundamentals of heat and mass transfer*, 8th ed. Hoboken, NJ: John Wiley & Sons, Inc, 2017.
- [186] L. Stiny, *Passive elektronische Bauelemente: Aufbau, Funktion, Eigenschaften, Dimensionierung und Anwendung*, 2nd ed. Wiesbaden: Springer Fachmedien Wiesbaden, 2015.
- [187] W. Machon, *Friedrich Tabellenbuch: Elektrotechnik/Elektronik Tabellenbuch*, 9th ed.: Bildungsverlag Eins, 2017.

- [188] F. Bernhard, *Handbuch der technischen Temperaturmessung*. VDI-Buch, 2nd ed. Vieweg: Springer-Verlag Berlin Heidelberg, 2014.
- [189] M.-K. Chin, C.-W. Lee, S.-Y. Lee, and S. Darmawan, "High-index-contrast waveguides and devices," *Applied Optics*, vol. 44, no. 15, pp. 3077–3086, 2005.
- [190] Donald K. Cohen, Wing Ho Gee, M. Ludeke, and Julian Lewkowicz, "Automatic focus control: the astigmatic lens approach," *Applied Optics*, vol. 23, no. 4, pp. 565–570, 1984.
- [191] N. Bamiedakis *et al.*, "Low-loss, high uniformity 1x2, 1x4 and 1x8 polymer multimode Y-splitters enabling radio-over-fiber multicasting applications," in *European Conference on Integrated Optics*, Copenhagen, Denmark, 2007.
- [192] N. Bamiedakis, R. V. Penty, and I. H. White, "Compact multimode polymer waveguide bends for board-level optical interconnects," *Journal of Lightwave Technology*, vol. 31, no. 14, pp. 2370–2375, 2013.
- [193] A. Hashim, N. Bamiedakis, R. V. Penty, and I. H. White, "Multimode polymer waveguide components for complex on-board optical topologies," *Journal of Lightwave Technology*, vol. 31, no. 24, pp. 3962–3969, 2013.
- [194] I. Salinas, I. Garces, R. Alonso, A. Llobera, and C. Dominguez, "Simple estimation of transition losses in bends of wide optical waveguides by a ray tracing method," *IEEE Photonics Technology Letters*, vol. 16, no. 3, pp. 825–827, 2004.
- [195] R. Pitwon *et al.*, "International standards for optical circuit board fabrication, assembly and measurement," *Optics Communications*, vol. 362, pp. 22–32, 2016.
- [196] V. Subramaniam, G. N. de Brabander, D. H. Naghski, and J. T. Boyd, "Measurement of mode field profiles and bending and transition losses in curved optical channel waveguides," *Journal of Lightwave Technology*, vol. 15, no. 6, pp. 990–997, 1997.
- [197] J. Chappell and D. A. Hutt, "Inkjet fabrication of optical waveguides: Integrated optical and electronic interconnect PCB manufacturing," Loughborough, UK, Jul. 4 2008.
- [198] B. R. Watts, "Development of a microchip-based flow cytometer with integrated optics – device design, fabrication, and testing," Ph.D. dissertation, McMaster University, Hamilton, 2012.
- [199] H. S. Cho *et al.*, "Optical interconnection using fiber-embedded boards and connection blocks fabricated by a micro-grooving technique for fiber insertion," *Journal of Micromechanics and Microengineering*, vol. 14, no. 8, pp. 1181–1184, 2004.
- [200] J. M. Ruano-López *et al.*, "A new SU-8 process to integrate buried waveguides and sealed microchannels for a Lab-on-a-Chip," *Sensors and Actuators B: Chemical*, vol. 114, no. 1, pp. 542–551, 2006.
- [201] A. Rashidi, R. Gharavi, and A. Gharavi, "Fiber to polymer-waveguide coupling with low insertion loss," *Journal of Optics*, vol. 17, no. 4, p. 45801, 2015.
- [202] J. Liu *et al.*, "A novel device of passive and fixed alignment of optical fiber," *Microsystem Technologies*, vol. 10, no. 4, pp. 269–271, 2004.

- [203] Y. Morimoto and T. Ishigure, "Low-loss light coupling with graded-index core polymer optical waveguides via 45-degree mirrors," *Optics Express*, vol. 24, no. 4, p. 3550, 2016.
- [204] W. Vis, "Polymer materials, processing, and structures for optical turning in 3D glass photonic interposers," M.Sc. thesis, School of Materials Science and Engineering, Georgia Institute of Technology, Atlanta, 2016.
- [205] R. Krahenbuhl, T. Lamprecht, E. Zraggen, F. Betschon, and A. Peterhans, "High-precision, self-aligned, optical fiber connectivity solution for single-mode waveguides embedded in optical PCBs," *Journal of Lightwave Technology*, vol. 33, no. 4, pp. 865–871, 2015.
- [206] L. Dellmann *et al.*, "120 Gb/s Optical Card-to-Card Interconnect Link Demonstrator with Embedded Waveguides," 2007.
- [207] P. Bayat, F. Esmek, T. Günther, and A. Grundhoff, "Nanofluidics and nano-optics for in-line DNA optical mapping," in *44th International Conference on Micro & Nano Engineering*, Copenhagen, 2018.
- [208] R. Lindken, M. Rossi, S. Grosse, and J. Westerweel, "Micro-particle image velocimetry (microPIV): Recent developments, applications, and guidelines," *Lab on a chip*, vol. 9, no. 17, pp. 2551–2567, 2009.
- [209] B. J. Gemmell, H. Jiang, and E. J. Buskey, "A new approach to micro-scale particle image velocimetry (μ PIV) for quantifying flows around free-swimming zooplankton," *Journal of Plankton Research*, vol. 36, no. 5, pp. 1396–1401, 2014.
- [210] K. L. Pitts and M. Fenech, "Micro-particle image velocimetry for velocity profile measurements of micro blood flows," *Journal of visualized experiments*, vol. 74, e50314-1-e50314-8, 2013.
- [211] S. Dufour and Y. de Koninck, "Optrodes for combined optogenetics and electrophysiology in live animals," *Neurophotonics*, vol. 2, no. 3, 031205-1 - 031205-14, 2015.
- [212] F. Pisanello, F. Pisano, M. Pisanello, A. Rizzo, A. Balenaa, L. Sileo, R. Peixotoc, E. Lemmad, E., "Tapered optical fibers for multifunctional neural interfaces," in *44th International Conference on Micro & Nano Engineering*, Copenhagen, 2018.

8 Appendix

Table 8.1: Evaluation of propagation and coupling losses at $\lambda=850$ nm (EpoCore, straight waveguides).

Length of the waveguide [cm]	Losses (1 st sample) [dB]	Losses (2 nd sample) [dB]
7.93	5.02	4.77
6.95	4.75	4.02
5.85	3.69	3.26
4.85	3.16	2.96
3.88	2.48	2.31
2.98	1.99	1.81
2.19	1.71	1.41

Table 8.2: Evaluation of bending losses at $\lambda=850$ nm.

r [mm]	Bending losses [dB/cm]	Deviation [dB/cm]
1	9.836	0.668
2	2.847	0.279
3	1.441	0.247
4	0.813	0.199
6	0.433	0.170
8	0.244	0.144
10	0.210	0.120
12	0.145	0.099
14	0.101	0.081

Table 8.3: Sensor readings of conceptual testing of fiber-based refractometer with curved multi-mode fiber tip at $\lambda=1310$ nm.

Fluid	Refractive index, n	Sensor response P [dBm]	Deviation [dB]
air	1.0003	-45.8	0.406
water	1.3223	-55.5	0.360
ethylene glycol	1.4214	-59.9	0.756
glycerin	1.4631	-60.2	0.337

Table 8.4: Sensor readings of conceptual testing of fiber-based refractometer with flat multi-mode fiber tip at $\lambda=1310$ nm.


Fluid	Refractive index, n	Sensor response P [dBm]	Deviation [dB]
air	1.0003	-31.8	0.017
water	1.3223	-46.0	0.087
ethylene glycol	1.4214	-55.7	0.381
glycerin	1.4631	-65.7	0.346

Table 8.5: Sensor readings of polymer-based Fresnel refractometer on EOCB; configuration with integrated waveguides with curved end-face at $\lambda=850$ nm.

Fluid	Refractive index, n	Sensor response P [dBm]	Deviation [dB]
air	1.0002	-40.30	0.30
water	1.3290	-49.96	0.25
ethylene glycol	1.4255	-51.93	0.45
glycerin	1.4656	-53.04	0.09

Table 8.6: Sensor readings of polymer-based Fresnel refractometer on EOCB; configuration with integrated waveguides with flat end-face at $\lambda=850$ nm.

Fluid	Refractive index, n	Sensor response P [dBm]	Deviation [dB]
air	1.0002	-39.47	0.20
water	1.3290	-47.00	0.51
ethylene glycol	1.4255	-51.42	0.38
glycerin	1.4656	-56.91	0.34

	Absorption spectra EpoCore	Dok.-Nr.: Absorption EpoCore_052016.doc, Seite: 1 von 2
---	---------------------------------------	--

UV-vis -NIR-Absorption spectrum of EpoCore

Processing:

Substrate: Quartz glass
 EpoCore: 665 μm thickness
 PB: RT – 5 h @ 95 °C – RT
 D: 6000 mJ/cm^2 (MA broadband exposure, intensity measured and dose calculated @ 365 nm)
 PEB: RT – 45 min @ 95 °C - RT

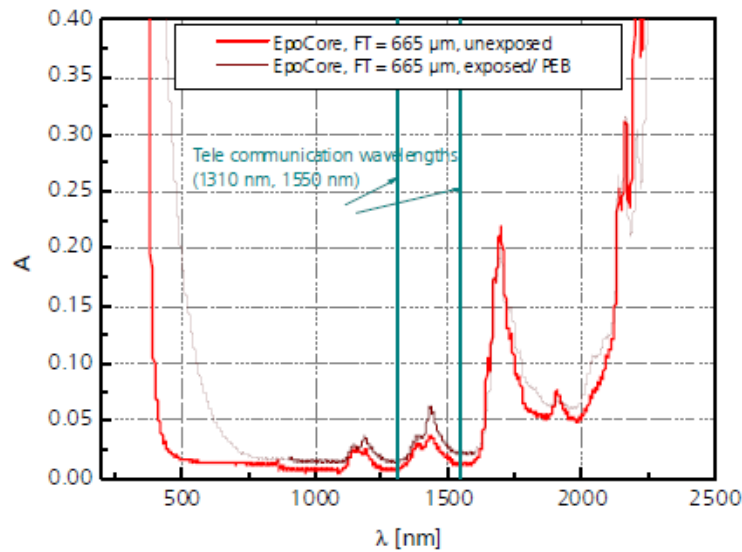


Fig.1: UV-vis-NIR absorption spectrum (as recorded)

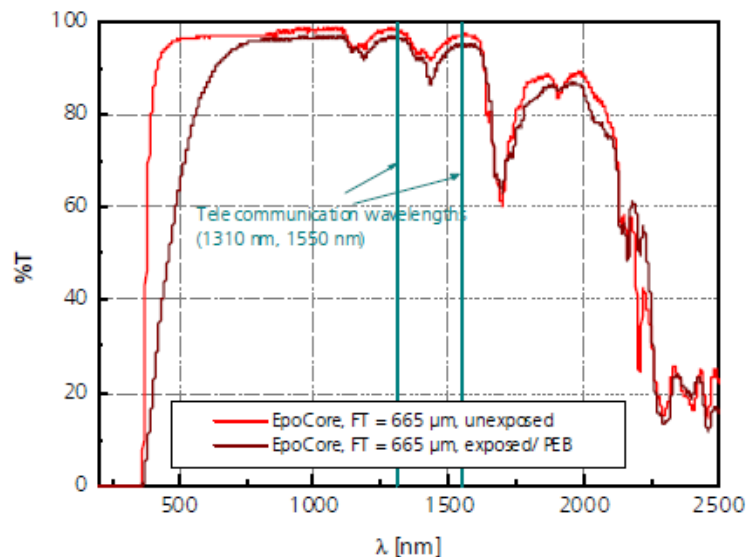


Fig.2: UV-vis-NIR transmission spectrum (as recorded/ calculated)

micro resist technology GmbH Koepenicker Str. 325, 12555 Berlin Tel.: +49 30 641670 100, Fax.: +49 30 641670 200	Dr. Anja Voigt 2016
--	------------------------

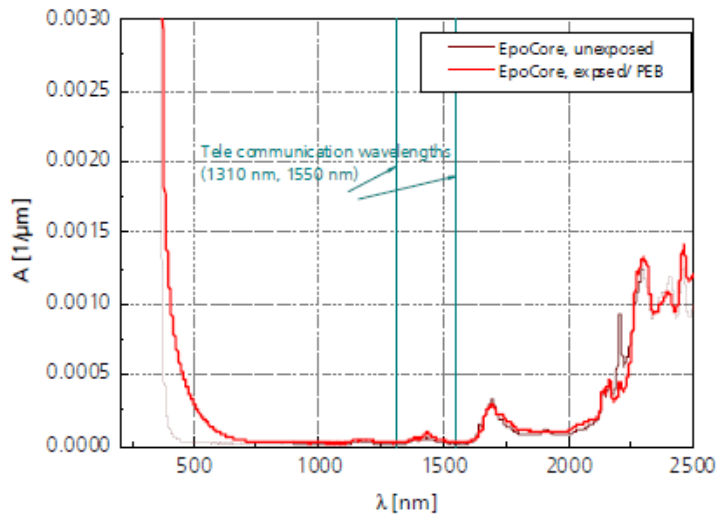


Fig.3: UV-vis-NIR absorption spectrum, normalized to thickness

